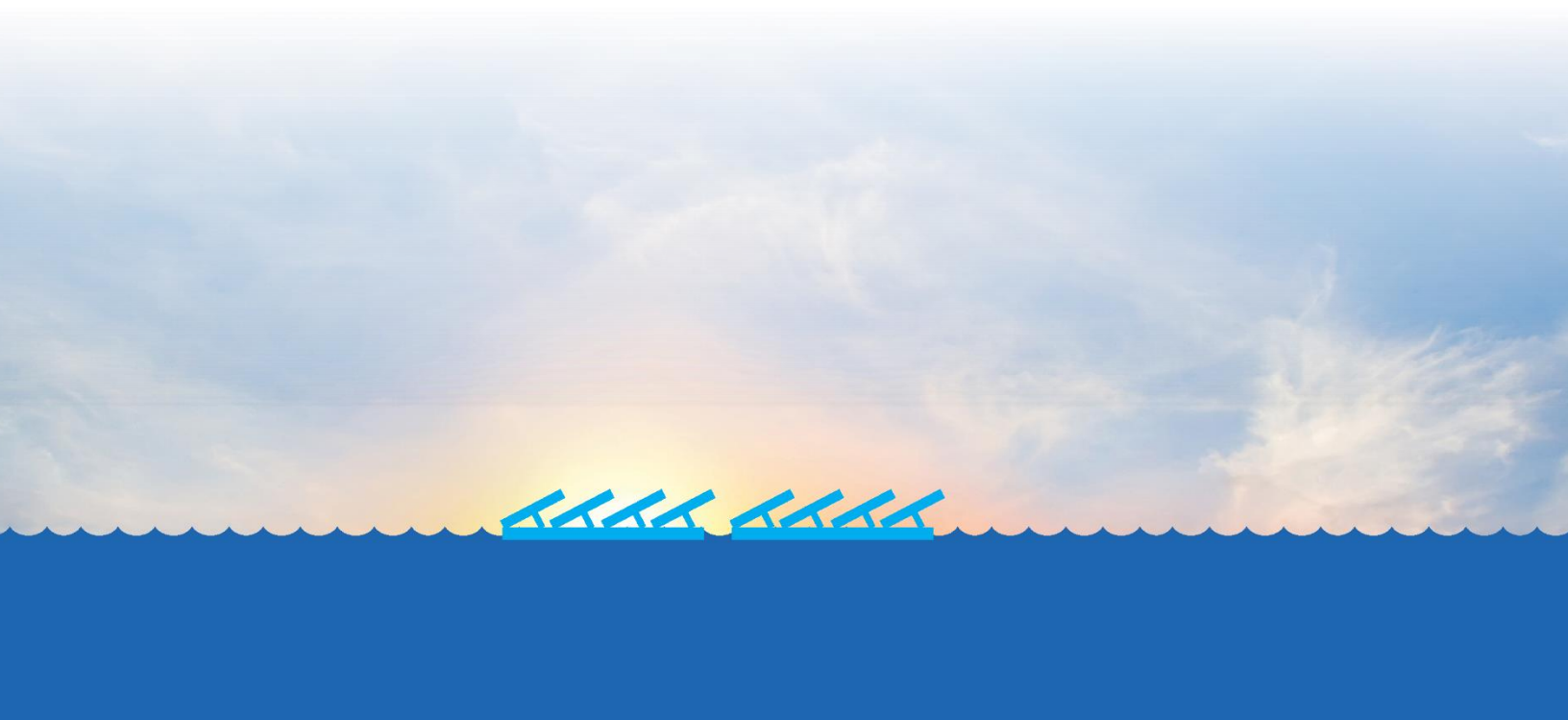# Offshore Floating Solar

Numerical Modelling of Interconnected Floating Solar Energy Platforms

F.J. Koppes

"The alphabet should start with X,Y,Z."
~ Dr. A. Extra ~

Numerical Modelling of Interconnected Floating Solar Energy Platforms

by

F.J. Koppes

to obtain the degree of Master of Science at the Delft University of Technology, to be defended on Wednesday April 17, 2019 at 14:00.

TU Delft

Oceans of Energy

Project duration: May 1st, 2018 – April 17th, 2019

Thesis committee:	Prof. dr. A.V. Metrikine	TU Delft
	Dr.ir A. Jarquin Laguna	TU Delft
	Dr. F. Pisano	TU Delft
	J.M. Nijk, MSc	Oceans of Energy

Abstract

Land scarcity is increasing and therefore one of the main challenges for renewable energy in the future is 'physical space'. While renewables need a lot of space compared to conventional energy sources, and the competition for space is already increasing (food production, housing etc.), leading to higher land costs and opposition. Public resistance to new highly visible windfarms and onshore solar farms is hardening. Large land-based solar farms compete with agricultural use and can have negative effects on the ecosystem, by covering the soil from the solar light. A solution to the stated problems is by placing renewable energy production at sea, among which offshore floating solar energy.

One of the main challenges in offshore floating solar is the continuous wave-induced motion of floaters, and the forces that arise at the most critical points. Dynamically modelling multiple floaters in waves becomes very computationally and time intensive when the number of floaters increases. This research focused on creating and comparing a linear and a non-linear model that calculates motions of multiple floaters under first order wave forces. The aim is to perform these calculations with open-source software only.

The dynamic forces on the floaters are obtained by evaluating the radiation, diffraction and wave excitation potential in the open-source Boundary-Element-Method-Solver NEMOH and showed good resemblance with commercial software packages AQWA and DIFFRAC. The modelling of the motions is performed in time (linear and non-linear RK4-integration-scheme) and frequency domain (linear). The implementation of the dynamic forces in both cases showed to be the most critical for the behavior of the floaters. Especially the determination of the hydrodynamic coefficients: Infinite added mass and retardation function for the time domain simulation are key in getting the same result for the linear time domain and frequency domain. Suppressing non-realistic values of gap resonance between multiple floating bodies increases the efficiency of time-domain simulations. Small differences between the motions of the floaters can cause significant differences in the forcing, therefor it is rather advisable to perform the comparison between the linear and non-linear case in time domain.

A comparison of different wave directions and conditions showed that the results of the linear model are of the same order of magnitude as the non-linear model. For the determination of motions and forcing under first order wave forces this shows that both cases are similar. Nevertheless, other non-linear effects can be added in a follow-up study.

"We build to many walls and not enough bridges"
~ Isaac Newton ~

Acknowledgements

The feeling of reaching a point where several of your paths in life come together, makes it difficult to not forget people that inspired me along the way.

Firstly, I would like to thank my committee from the university, Andrei Metrikine and Antonio Jarquin Laguna. Next to giving good guidance, they were both true inspirers and amazing tutors along my path at the university.

Secondly, I would like to thank Jeremy Nijk from Oceans of Energy for having confidence in me, his insights and positivity, good talks about life and giving me the opportunity and freedom to be involved in the company. Not to forget all the employees and graduates at Oceans of Energy that make the OOE-family an unstoppable train that has great potential to build something for the future.

Next to that I should thank my dear friends Kizjè, Timo, Machiel, Roy, Ben and Coen for the interesting talks, feedback and taking up (technical) challenges together, but most important for being along my side.

Special thanks to my parents and sister, for forming a great basis and supporting me always. Finally, I would like to thank Dr. A. Extra, my mathematics teacher at high school, for his valuable lessons and inspiration, that I will never forget.

Fabian Koppes, April 2019

Contents

11

1. Introduction

Land scarcity is increasing and therefore one of the main challenges for renewable energy in the future is 'physical space'. While renewables need a lot of space compared to conventional energy sources, and the competition for space is already increasing (food production, housing etc.), leading to higher land costs and opposition. Public resistance to new highly visible windfarms and onshore solar farms is hardening. Large land-based solar farms compete with agricultural use and can have negative effects on the ecosystem, by covering the soil from the solar light. A solution to the stated problems is by placing renewable energy production at sea.

Wind energy has shown to be very competitive in offshore locations already, and sometimes even cheaper due to the economy of scales. A same effect can be expected for offshore floating solar energy. Multiple floating solar projects on inland lakes have been carried out, in the past ten years, in especially Europe and Asia, and have shown to be a beneficial solution as well (Trapani & Redon Santafe, 2014). Nevertheless, no real offshore floating solar projects have been carried out yet, since harsh offshore environments make it hard for "cheap" solutions that can survive the waves.

1.1   Context

Now the Netherlands, China and Singapore are starting their first pilot projects for offshore floating solar. In the Netherlands this is a consortium led by the start-up Oceans of Energy (Oceans of Energy B.V., 2018).

It is expected that the cooling of the seawater will lead to an increase of power production of the solar panels of 5-15% and is one of the main targets for the first floating solar project on the Dutch North Sea in 2019. Expected is that by the end of 2019 a start is made with a first offshore solar array: multiple solar floating platforms connected to each other at sea, riding the waves.

1.2   Problem definition

One of the main challenges in offshore floating solar is the continuous motion of the floating platforms (floaters), and the forces that arise at the most critical points, namely the joints in between the platforms. Dynamically modelling multiple floaters in waves and the forces that arise in the interconnecting joints becomes very computationally and time intensive when the number of floaters increases. This research focusses on the possibilities of creating a linearized model that calculates motions of interconnected floaters under first order wave forces and see what the difference is with a non-linear model. The aim is to perform these calculations with open-source software only.

The main research questions are:

- What is an appropriate way of calculating motions of floating bodies and how can this all been done with open source tools only?
- How to build a model that combines all the coefficients for multiple degrees of freedom?
- How can the joints be implemented?

- o In a non-linear model
- o In a linear model
- What is the effect of linearizing the model on the overall motions and forces, compared to the non-linear model?
- What are the effects of wave-directions on the forces expected in the joints?
- What is the effect of different types of joints on the forces in the joints?

1.3 Scope

This report was simultaneously written with the start of developing offshore floating solar in the Dutch North Sea. Therefor this report evaluates all the required inputs that are needed for a hydrodynamic model, from floater characteristics to environmental conditions.

This report compares linear and non-linear responses of the motions of the floaters and the forces in the connections to first order wave forces. The models developed should give an estimation if linearization of the joint forces on the floaters Center of Gravity (CoG) is applicable. The models developed contain all hydrodynamic coefficients through an open source BEM-solver, the coupled equations of motion (non-linear and linear) are automatically composed for given joint locations and the resulting motions and forces numerically calculated.

The models created in this research can be further developed for more non-linear effects like: mooring, non-linear joint stiffness, non-linear hydrodynamic damping and second order wave forces. But this is not evaluated in this research.

1.4 Research approach

This research is started with a brief literature study about modelling floating bodies in water (1.6) and the expected environmental conditions in an offshore floating solar project (1.5). Where after the equations of motion for a linear frequency domain model (FD) and a non-linear time domain model (TD) are given (2). For the proposed floater (designed simultaneously with this report) all geometrical properties are calculated (2.3). Hydrodynamic coefficients are solved in a BEM-solver (boundary element method) based on potential theory. In order to validate open source codes for this, a comparison is made with commercial BEM software packages for the same geometry (3).

The model starts with a description of the system of floaters and the implementation of the joints (2.4). The implementation of a numerical time-domain model (4.1) and frequency domain model (4.2) and its challenges is described. The non-linear time domain model is verified with standard cases, the exact solution is known and the linear time-domain model is verified with the frequency domain model in time and frequency domain (6). Since potential theory in BEM-solvers can cause gap resonance issues between floaters, the effect and the suppression of it is discussed (5). Finally, the models are compared for different wave directions and joint types (7).

1.5 Site Location

This study is performed for the initial deployment site for the first Dutch offshore solar array on the North Sea. The environmental conditions for this location are shortly discussed.

1.5.1 Bathymetry

The North Sea is a relatively shallow sea with the Dutch sector varying between 20 and 50 meters. The identified test location for the first dutch offshore floating solar project is at the North Sea Innovation Lab (NSIL). This is an offshore innovation test facility accommodating a prototype seaweed farm about 15 km offshore of the port of Scheveningen. The area has a relatively constant bathymetry at 20m LAT as is shown in Figure 1.1.
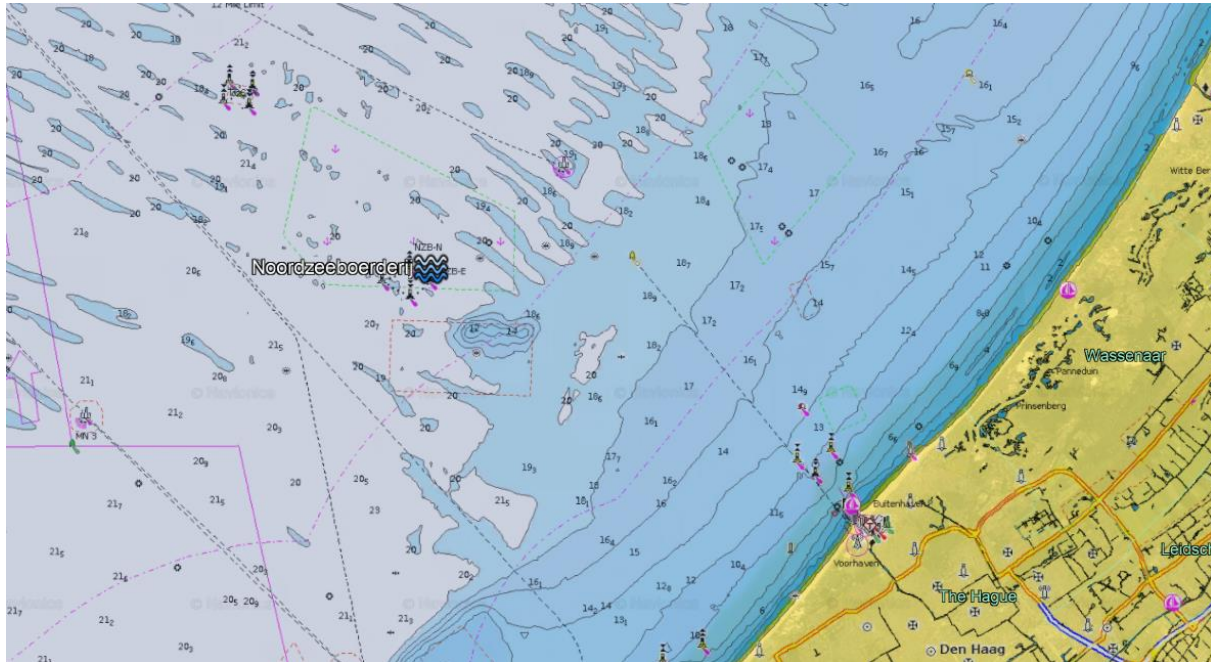
Figure 1.1 – North Sea around the NSIL showing a relatively constant water depth around the test area.

1.5.2 Wave Environment

Wave data is analyzed from 5 different sources:

- North Sea Innovation Lab
- Fugro
- Eneco Luchterduinen available data
- BMT ARGOSS
- RWS measurement buoys

For locations see Figure 1.2. With these data the extreme wave parameters are calculated for different return periods with Weibull tail-fitting, see Figure 1.3.
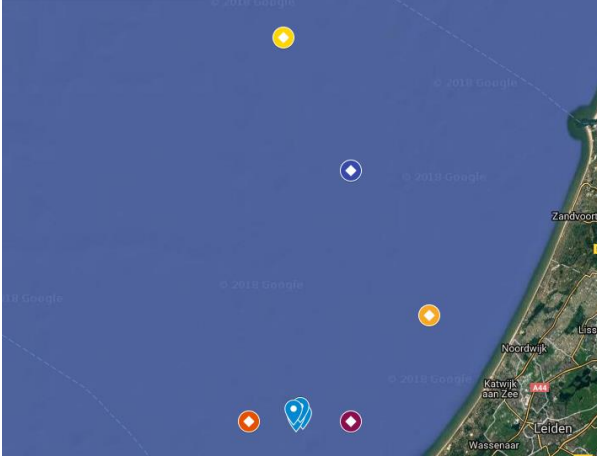
Figure 1.2 – Overview of locations of available data.
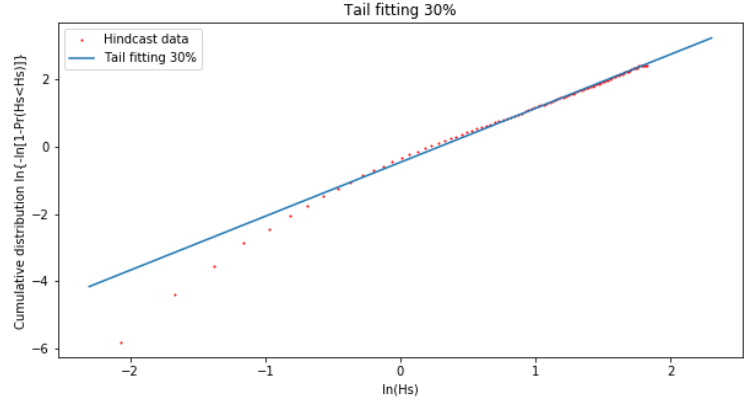
Figure 1.3: CDF of GP1 data with 30% tailfitting

The retrieved result from the different available data led to the following design conditions:

- Ultimate limit state (ULS): $H_s = 7.0m, T_p = 12.7s$
- Serviceability limit state (SLS): $H_s = 2.0m, T_p = 6.7s$

1.5.3 Wave Spectrum

The applied wave energy density spectrum in this research is the JONSWAP-spectrum. This is most common used spectrum for designing at the North Sea (Holhuijsen, 2010) and can be described in the following form in relation to the significant wave height H_s and peak period T_p (DNV, 2010):

As a continuous variance density spectrum the JONSWAP spectrum $S_J(\omega)$, a modification on the Pierson-Moskowitz spectrum $S_{PM}(\omega)$, is used.

$$S_{PM}(\omega) = \frac{5}{16} H_s^2 \omega_p^4 \omega^{-5} \exp\left(-\frac{5}{4}\left(\frac{\omega}{\omega_p}\right)^4\right) \qquad \textit{(Eq. 1.1)}$$

$$S_J(\omega) = A_\gamma S_{PM}(\omega) \gamma^{\exp\left(-0.5\left(\frac{\omega - \omega_p}{\sigma \omega_p}\right)^2\right)} \qquad \textit{(Eq. 1.2)}$$

Where $\gamma = non\ dimensional\ peak\ shape\ parameter,\ \sigma = spectral\ width\ parameter$

$\sigma = \sigma_a\ for\ \omega \leq \omega_p,\ \sigma = \sigma_b\ for\ \omega > \omega_p,\ A_\gamma = 1 - 0.287\ln(\gamma)$

For $\omega_p = \frac{2\pi}{T_p} = 0.4947 \frac{rad}{s}$ and $H_s = 7.0m$ this leads to the spectrum shown in Figure 1.4.

17
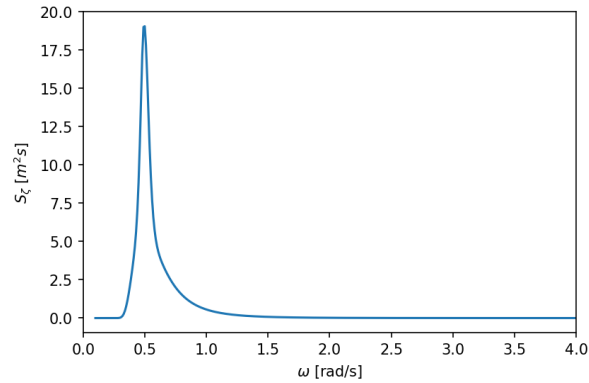
Figure 1.4: JONSWAP spectrum for $H_s = 7.0m, T_p = 12.7s, \gamma = 3.3$

1.6 Model approach

This chapter describes briefly the most used methods that exist to model the motions and forces on floating bodies in waves.

1.6.1 Bodies in water

There are several ways of calculating motions and forces in floating bodies in water. The most common are listed below:

- Morison (drag and inertial forces)
- Potential theory (BEM-solvers)
- Reynolds averaged Navier-Stokes simulation (CFD)

Morison equation is only valid for bodies that are slender compared to occurring wavelengths. Potential theory and CFD are both applicable for the problem, but both have their issues.

Potential flow models take a few assumptions in consideration (Folley, et al., 2012):

- Inviscid fluids
- Irrotational flow: a velocity potential exists $\phi(M, t)$, wherefrom the velocity can be calculated at every place in the domain: $\vec{V}(M, t) = \vec{\nabla}\phi(M, t)$
- Incompressible flow: With conservation of mass this leads to the Laplace equation: $\Delta\phi(M, t) = 0$

Solving potential functions is a non-linear boundary value problem and therefore calculating potential flows the problem is further linearized. Assumptions made are described by (Folley, et al., 2012):

- The ratios of wave height to wavelength (i.e. wave steepness) and wave height to water depth must both be much smaller than 1.
- The motions of the body are small and around a fixed mean position: the ratio of the typical amplitude of motion to the typical dimension of the body is much smaller than 1.

Although these assumptions are violated for small floaters in intermediate depths. The linear potential theory is known as a good estimation for calculations of floating bodies (frequently used for the modelling of wave energy converters). Nevertheless, when the sea-states are getting harsher on small floating objects, experiments have shown that modelling with CFD show better results. On the other hand BEM-solver calculations are much faster than CFD-calculations.

CFD models are models that resolve specific terms of the Navier-Stokes equations, these are based on the conservation of mass and momentum. In comparison to potential theory, viscous and turbulence effects can be taken into account. Especially for the modelling of bodies in harsh conditions, this method is very applicable, since it can also take into account viscous effects and a combination of air-water effects like breaking waves or fountain spraying in floater gaps. This is also one of the main weaknesses: CFD models are often prone to internal dissipation, particularly when resolving gravity water waves (free surface flow).

Since the intended floaters have a low freeboard, it will be overtopped frequently by waves and water will splash (fountaining effect), potential theory might not be as good as expected, since it only considers the radiation, diffraction and wave loading perpendicular to the wetted surface. Also, effects like turbulence (especially for a rectangular floater that has sharp edges) are challenging to take into account. Despite all these limitations, using BEM-solvers this is a most common practice in Offshore/Maritime industries to analyze floater's motions in design stages.

CFD-calculations require high computational effort and it is not certain if the result will be trustworthy. The boundary between air and water is already difficult to simulate and will be even harder with a lot of splashing.

1.7 Model domain

From this point onward it is chosen to start with potential theory simulations, to identify the motions of- and forces in the joints between the floaters. Two main model possibilities can be distinguished, after solving the potential theory:

- Time domain
- Frequency domain

Time domain analysis requires higher computational time and frequency domain analysis cannot handle non-linear terms, which can be an issue with interconnecting joints for multiple floaters and moorings. The time domain model is further evaluated in section 4.1 and the frequency domain model in section 4.2.

In Figure 1.5 an overview is given of the model approach in this research. The boxes symbolize the steps taken in this research to model interconnected offshore floating platforms. This results in a linear frequency domain model (FD), a linear (TDL) and a non-linear (TDNL) time domain model that will be compared in the result section. All the steps will be discussed in the following chapters.
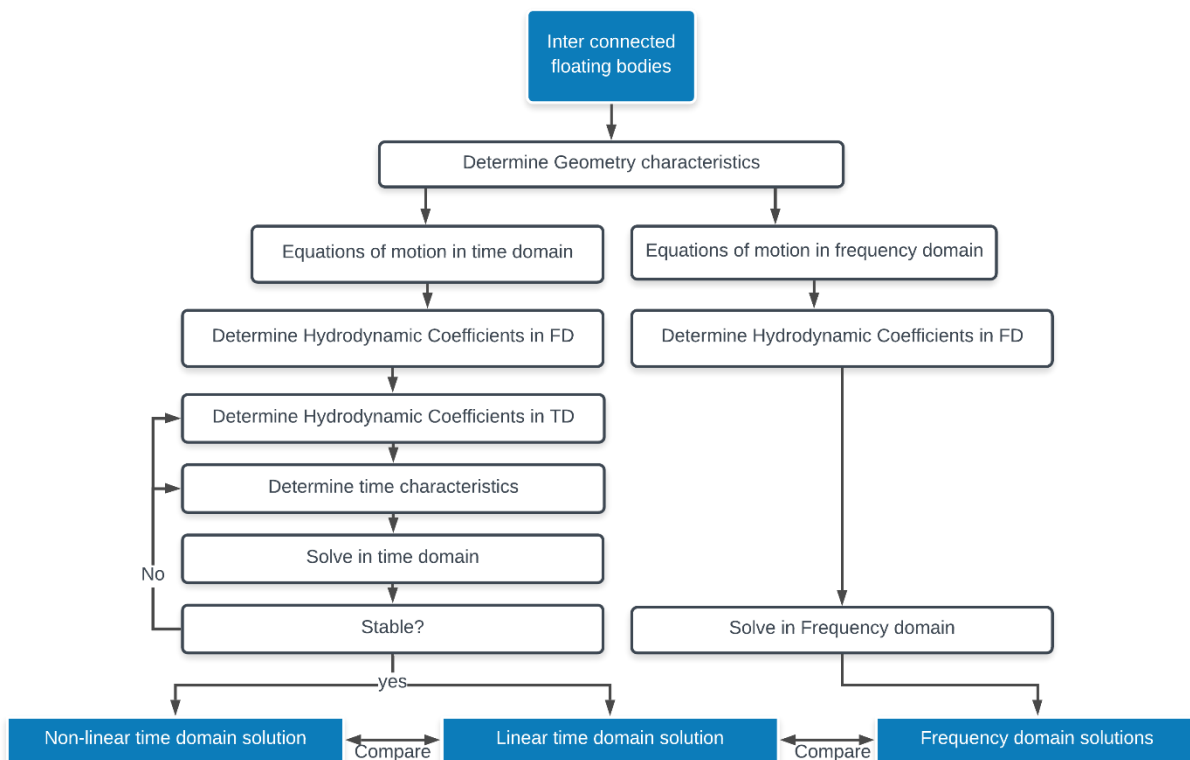
Figure 1.5: Overview of the model approach in this research

2. System description

In this chapter the considered system is briefly described. The geometry and sign conventions used in the system are needed for correct calculations. After that the systems equations of motion for frequency domain and time domain calculations are presented and the forcing terms summarized.

2.1 Geometry

An overview of the system and the sign convention is given in Figure 2.1.

The considered system in this research consists of two interconnected floaters. The floaters have a very small height compared to their length and width and on each floater approximately fit 15 solar panels.

The draft is approximately at two third of the floater's height, while the center of gravity is below the waterline, but higher than the geometrical center of the structure due to the electrical equipment on top. Every floater has its own local axis system in the center of gravity. The floaters are interconnected with joints on the outer edges, where the connecting points on the first floater are denoted with P_{11} and P_{12}. The wave directions are according to the axis systems.
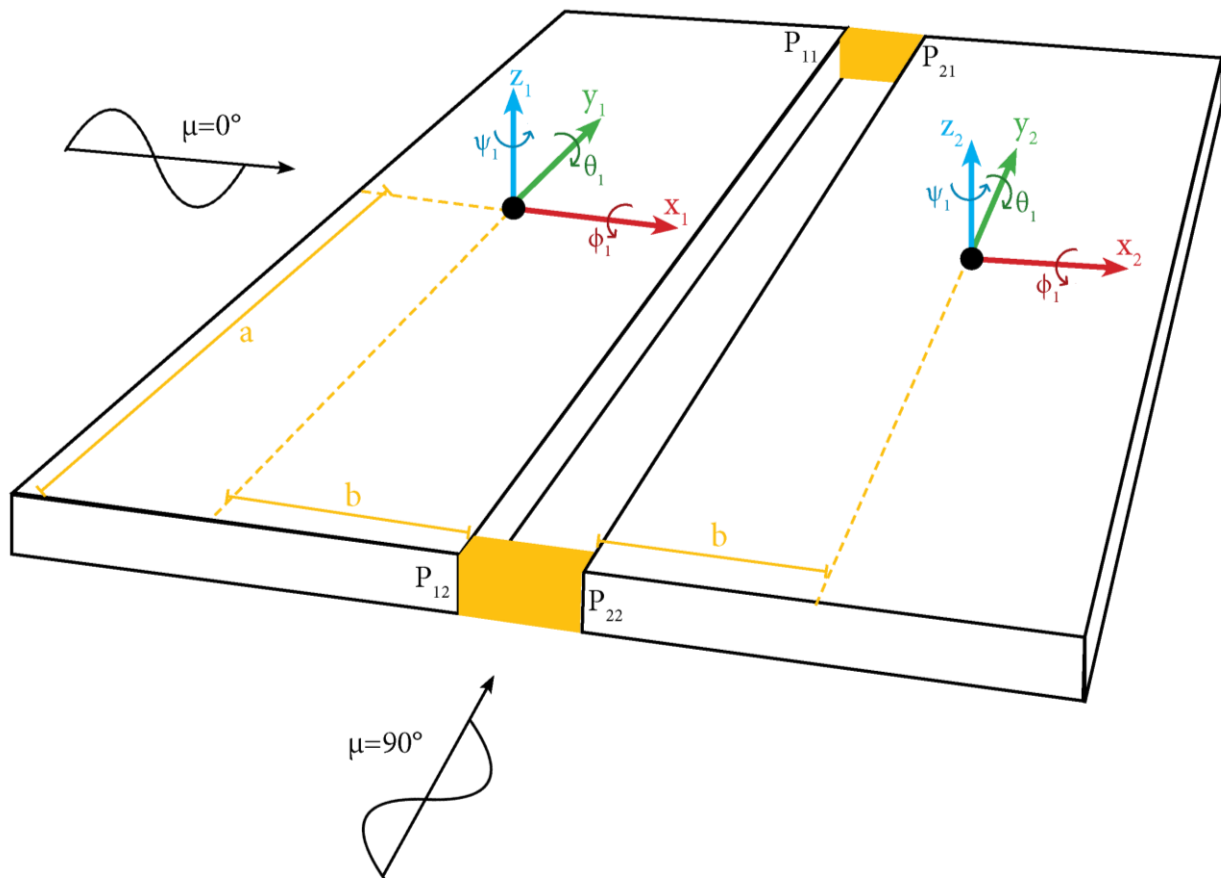
Figure 2.1: Overview of the geometry of the structure, sign convention and wave direction.

2.1.1 Floater motions

The motions of the floater are described as presented in Figure 2.1, with the corresponding textual reference, given in Table 2.1.

Table 2.1: axis and motion naming

Sign	Name	Number (first floater)	Number (second floater)
x	Surge	1	7
y	Sway	2	8
z	Heave	3	9
ϕ	Roll	4	10
θ	Pitch	5	11
ψ	Yaw	6	12

Motions are described with respect to the floaters center of gravity. Translational motions are denoted with u_t ($x, y \text{ or } z$) and rotational motions with u_r (ϕ, θ, ψ). Any of the motions in general is denoted as u ($x, y, z, \phi, \theta, \psi$). All motions in vector notation as $\underline{u} = [x, y, z, \phi, \theta, \psi]^T$ for a single floater and for two floaters $\underline{u} = [u_1, u_2, \dots, u_{12}] = [x_1, y_1, z_1, \phi_1, \theta_1, \psi_1, x_2, y_2, z_2, \phi_2, \theta_2, \psi_2]$.

2.1.2 Wave directions

The convention of the wave directions (μ) is presented in Figure 2.1 and due to symmetry of the system the wave directions only need to be evaluated for: $0° \leq \mu \leq 90°$. Other textual references in the report are given in Table 2.2.

Table 2.2: Textual reference for certain wave direction.

μ	Textual reference
0°	Beam waves
90°	Head waves
μ	μ-waves

2.2   Equation of motion

The equation of motion for a body can be derived from Newton's second law (Journee & Massie, 2001):

$$\vec{F} = \frac{d}{dt}\left(m\vec{V_t}\right) \; and \; \vec{M} = \frac{d}{dt}\left(\vec{H}\right)$$

<div align="right">(Eq. 2.1)</div>

$\vec{F}$ resulting external force acting in the center of gravity (N)

m Mass of the rigid body (kg)

$\vec{V}$ Instantaneous velocity of center of gravity (m/s)

$\vec{M}$ Resulting external moment acting about the center of gravity (Nm)

$\vec{H}$ Instantaneous angular momentum about the center of gravity (Nms)

t Time (s)

In water, when the system is linear, the motion of a floating body in waves can be seen as the summation of the motion in still water and the forcing by waves on the restrained body (Journee & Massie, 2001). Applying Newton's second law will result in the following equation for respectively translational and rotational motions:

Translational: $\frac{d}{dt}(m\dot{u}_t) = \rho\nabla\ddot{u}_t = F_h + F_w$

<div align="right">(Eq. 2.2)</div>

Rotational: $\frac{d}{dt}(I\dot{u}_r) = I\ddot{u}_r = M_h + M_w$

<div align="right">(Eq. 2.3)</div>

Where:

ρ density of water (kg/m^3)

∇ volume of displacement of the body (m^3)

I Mass moment of inertia (kgm^2)

F_h, M_h hydromechanical force or moment (N or Nm)

F_w, M_w exciting wave force or moment (N or Nm)

u_t Translational motion (m)

u_r Rotational motion (rad)

2.2.1   Frequency domain equation of motion

The equation of motion in time domain can also be written in frequency domain, if the external forcing is a superposition of harmonic vibrations, which is the case in linear wave theory. To analyze a single

degree of freedom system under linear harmonic loading in frequency domain, can be done by the Integral Fourier Transform. This can only be applied for zero initial conditions.

The Fourier Transform states:

$$\begin{Bmatrix} \tilde{F}(\omega) \\ \tilde{u}(\omega) \end{Bmatrix} = \int_{-\infty}^{\infty} \begin{Bmatrix} F(t) \\ u(t) \end{Bmatrix} e^{-i\omega t} dt$$

The equation of motion for a single translational degree of freedom then becomes:

$$(-\omega^2 m)\tilde{u}(\omega) = \tilde{F}_h(\omega) + \tilde{F}_w(\omega)$$

Hydromechanical forces and moments

Hydromechanical forces (and moments) arise due to harmonic oscillations of the body in the undisturbed fluid. It can be subdivided into a hydrostatic and a hydrodynamic part:

$$\tilde{F}_h = \tilde{F}_{static} + \tilde{F}_{dynamic} \tag{Eq. 2.4}$$

Physically the hydrostatic force is a force on the body in a displaced situation with zero velocity and is opposite to the direction of the displacement. It is given as a hydrostatic stiffness:

$$\tilde{F}_{static} = -c \cdot \tilde{u}(\omega) \tag{Eq. 2.5}$$

The hydrostatic stiffness will be further elaborated on in section 2.3.3.

The hydrodynamic force $\tilde{F}_{dynamic}$, also known as the radiation force $\tilde{F}_r$ is a result of the motion of the body in the water. Assuming harmonic excitation, the radiation force will result in two components with the same frequency as the excitation frequency. One in phase with the velocity of the body and one in phase with the acceleration of the body:

$$\tilde{F}_{dynamic} = \omega^2 a\tilde{u} - i\omega b\tilde{u} \tag{Eq. 2.6}$$

Characterized as the added mass (a), and the hydrodynamic damping (b) coefficient. Physically the hydrodynamic term relates to radially propagating waves away from the body, meaning that energy is distracted from the system (damping). The force $\omega^2 a\tilde{u}$ is caused by the accelerations of the water particles close to the body. This can be interpreted as water mass moving along with the body, and therefor as an added mass to the system.

Wave excitation forces

The first order wave excitation forces (and moments) consists of two forces: a diffraction force and a Froude-Krilov force:

$$\tilde{F}_w = \tilde{F}_D + \tilde{F}_{FK} \tag{Eq. 2.7}$$

The Froude-Krilov force is the force of the undisturbed wave on the floating body, derived from the integration of the pressures on the body's surface. The diffraction force is a correction on this assumption, since the waves will be diffracted by the floating body.

Further evaluating these forces will result in the frequency domain equation for a translational motion (the same procedure holds for a rotational degree of freedom considering equation 2.3):

$$\left(-\omega^2\big(m + a(\omega)\big) + i\omega b(\omega) + c\right)\tilde{u}(\omega) = \tilde{F}_w(\omega) \qquad \text{(Eq. 2.8)}$$

Where:

$\tilde{u}$	Complex Motion (m)
m	Mass of the body (kg)
a	Added mass coefficient for heave (Ns^2/m=kg)
b	Hydrodynamic damping coefficient for heave (Ns/m)
c	Restoring spring coefficient for heave (N/m)
ω	Excitation frequency (rad/s)
$\tilde{F}_w$	Complex FD Excitation force (N)

Multiple degree of freedom system

More general the equation of motion can also be written for a multiple degrees of freedom system, with its corresponding matrices:

$$\left(-\omega^2\big(M + A_H(\omega)\big) + i\omega B_H(\omega) + C\right)\underline{\tilde{u}}(\omega) = \underline{\tilde{F}}(\omega) \qquad \text{(Eq. 2.9)}$$

M	Mass matrix
A	Added mass matrix
B	Hydrodynamic damping matrix
C	Restoring Stiffness matrix
$\underline{\tilde{F}}(\omega)$	Complex excitation force (and moment) vector in frequency domain
$\underline{\tilde{u}}(\omega)$	Complex Motion vector in frequency domain $= \left[\tilde{x}, \tilde{y}, \tilde{z}, \tilde{\phi}, \tilde{\theta}, \tilde{\psi}\right]^T$

2.2.2 Time domain equation of motion

In order to make calculations for general loading, time domain calculations can be performed. The equation of motion looks slightly different, compared to the one in frequency domain. This equation of motion is known as the Cummins' equation, which evaluates the hydrodynamic damping force as a convolution of the velocity ($\dot{u}$) and a retardation function (R_u). The Cummins' equation for a translational motion is given:

$$\big(m + a_{\infty,u}\big)\ddot{u}(t) + \int_0^\infty R_u(\tau)\dot{u}(t - \tau)d\tau + c_u u(t) = F_w(t) \qquad \text{(Eq. 2.10)}$$

Where:

m	Mass of body
a_∞	Added mass at infinite frequency

25

R Retardation function

c Restoring spring coefficient for heave

$F_w(t)$ Wave Excitation force

u Motion

In this way the terms are not frequency dependent and a complete representation of the equation of motion under general loading is given in time domain.

Multiple degree of freedom system

Similar to equation 2.10 the system under general loading can also be expressed for MDoF systems in Matrix notation:

$$(M + A_\infty)\,\underline{\ddot{u}}(t) + \int_0^\infty R(\tau)\underline{\dot{u}}(t - \tau)d\tau + C\underline{u}(t) = \underline{F}(t)$$

(Eq. 2.11)

M Mass of body

A_∞ Added mass matrix at infinite frequency

R Retardation function matrix

C Restoring spring matrix

$\underline{F}(t)$ Wave Excitation force vector

$\underline{u}$ Motion vector

The different coefficients stated in this part are further described in the next section.

2.3   Equation of motion coefficients

In this section all coefficients of the equation of motion are shortly described and the procedure to obtain them.

2.3.1   Floater specifics

The following specifics of the floater need to be determined for further calculations in the process:

- Mass: m
- Center of Gravity (CoG)
- Moments of Inertia I_{xx}, I_{yy}, I_{zz}

Mass

Mass of all components in the floater added up together:

$$m = \sum_{i=1}^{n} m_i \qquad \text{(Eq. 2.12)}$$

Center of Gravity

The floaters center of gravity can be determined by implementing a reference axis system on the side of the floater, see Figure 2.2.
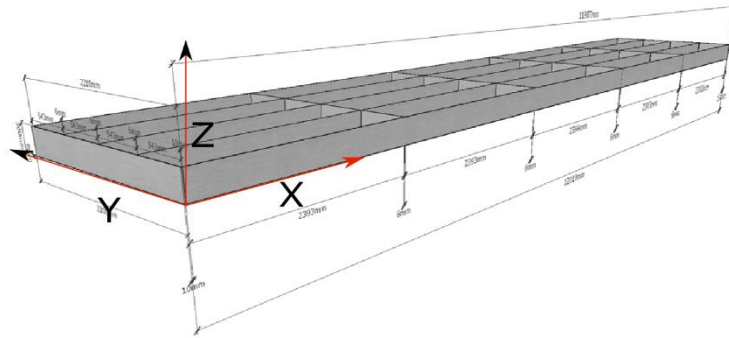
Figure 2.2: reference axis system for calculation of the floaters center of gravity

The floaters center of gravity is then calculated in the following manner:

$$c_{axis} = \frac{\sum(c_{axis,i} m_i)}{\sum m_i} \qquad \text{(Eq. 2.13)}$$

With: c_{axis} =floater center of gravity axis-coordinate, $c_{axis,i}$ =components center of gravity axis-coordinate and $axis = x, y \ or \ z$.

Moment of inertia

For each individual component of the floater the moment of inertia $I_{axis,i}$ and the eccentricity $a_{axis,i}$ from its own center of gravity to the floaters center of gravity needs to be determined. With Steiner's Rule the floaters moments of inertia can be determined.

$$I_x = \sum \left(I_{x,i} + m_i \big(a_{y,i}^2 + a_{z,i}^2 \big) \right) \qquad \text{(Eq. 2.14)}$$

$$I_y = \sum \left(I_{y,i} + m_i \big(a_{x,i}^2 + a_{z,i}^2 \big) \right)$$

$$I_z = \sum \left(I_{z,i} + m_i \big(a_{x,i}^2 + a_{y,i}^2 \big) \right)$$

The gyradii of the floater can be derived from the mass and the mass moment of inertia: $r_{axis} = \sqrt{\frac{I_{axis}}{m}}$

A detailed calculation of the mass m and moment of inertia I of the floater needs to be carried out for all the components (i.e. structural elements, electrical equipment).

2.3.2 Solid mass matrix

The solid mass matrix is determined by the weight and shape of the platform. It is assumed that its mass does not change in time.

So, water laying on top of the platform or added marine growth is neglected. It should be mentioned that this is of importance for further study, since the platforms own mass is not high. This will also influence the hydromechanic stiffness and damping.

The solid mass matrix for a single platform (6DOF) will become:

$$M = \begin{bmatrix} m & & & & & \\ & m & & & & \\ & & m & & & \\ & & & I_{xx} & & \\ & & & & I_{yy} & \\ & & & & & I_{zz} \end{bmatrix}$$

(Eq. 2.15)

To overcome confusion with coupling terms the moment of inertia is now denoted as I_{xx} instead of I_x as presented in equation 2.14. The coupling terms between pitch and roll ($I_{xz} = I_{zx}$) are neglected, they are generally small (Journée & Massie, 2001).

2.3.3 Hydrostatic stiffness matrix

The linear restoring matrix for a single floater, with respect to the center of floatation (waterline), can be written in the following manner (Marin, 2018):

$$C = \begin{bmatrix} 0 & & & & & \\ & 0 & & & & \\ & & c_{33} & & & \\ & & & c_{44} & & \\ & & & & c_{55} & \\ & & & & & 0 \end{bmatrix}$$

(Eq. 2.16)

With linearized: $c_{33} = \rho g A, c_{44} = GM_t \rho g V, c_{55} = GM_l \rho g V$ *(Eq. 2.17)*

$GM_t = KB + \frac{I_{xx}}{V} - KG, \; GM_l = KB + \frac{I_{yy}}{V} - KG$ *(Eq. 2.18)*

c_{33}: *generally, this is valid for small values of z, but when the floater is vertically walled, it remains exact for larger values of z.*

Since all the motions are evaluated with respect to the center of gravity, the stiffness matrix needs to be changed to the center of floatation. This is done with a generic translation matrix:

(Eq. 2.19)

$$T = \begin{bmatrix} 1 & & & & & \\ & 1 & & & & \\ & & 1 & & & \\ & & -\Delta z & \Delta y & 1 & \\ \Delta z & & -\Delta x & & 1 & \\ -\Delta y & \Delta x & & & & 1 \end{bmatrix}$$

(Eq. 2.19)

$$C_g = TCT^* = \begin{bmatrix} 0 & & & & & \\ & 0 & & & & \\ & & c_z & \Delta y c_z & -\Delta x c_z & \\ & & \Delta y c_z & c_{xx} + (\Delta y)^2 c_z & -\Delta x \Delta y c_z & \\ & & -\Delta x c_z & & c_{yy} & \\ & & & & & 0 \end{bmatrix}$$

(Eq. 2.20)

With $\Delta x = LCF - LCG, \Delta y = TCF - TCG, \Delta z = T - KG$

(Eq. 2.21)

The considered floater is axially symmetrical in the x-, and y-axis, meaning that in this case $\Delta x = 0, \Delta y = 0$, and the restoring stiffness matrix is reduced to matrix C presented in equation 2.16.

2.3.4 Hydrodynamic coefficients in frequency domain

The hydrodynamic coefficients can be calculated with the principles of potential theory, assuming that the flow is irrotational and non-viscous.

As described in section 2.2.1 the coefficients for added mass and hydrodynamic damping are related to the dynamics of the fluid around the body. Applying potential theory prescribes that the fluid only exerts forces perpendicular to the floating body. These forces can be solved by evaluating the radiation potential Φ_r. An overview of the theory is given in Appendix A. Nevertheless, mostly these equations for floating are solved in Diffraction-software using a boundary element method. Further on in Chapter 3 an overview and a comparison is given of these solvers.

For n degrees of freedom (nDoF), the added mass and damping matrix are a [n x n x number of frequencies] matrix in frequency domain.

$$A(\omega) = \begin{bmatrix} a_{1,1}(\omega) & \cdots & a_{1,n}(\omega) \\ \vdots & \ddots & \vdots \\ a_{n,1}(\omega) & \cdots & a_{n,n}(\omega) \end{bmatrix}, B(\omega) = \begin{bmatrix} b_{1,1}(\omega) & \cdots & b_{1,n}(\omega) \\ \vdots & \ddots & \vdots \\ b_{n,1}(\omega) & \cdots & b_{n,n}(\omega) \end{bmatrix}$$

(Eq. 2.22)

2.3.5 Hydrodynamic coefficients in time domain

The hydrodynamic coefficients for Cummin's equation in time domain can be derived by comparing the time domain and frequency domain equation of motion. (Ogilvie, 1964) found the following relation:

$$a_{ij}(\omega) = a_{ij} - \frac{1}{\omega}\int_0^\infty R_{ij}(\tau)\sin(\omega\tau)\,d\tau \leftrightarrow a_{ij} = a_{ij}(\omega) + \int_0^\infty \frac{1}{\omega}R_{ij}(\tau)\sin(\omega\tau)d\tau:$$

$$a_{ij,\infty} = a_{ij}(\omega \to \infty)$$

$$b_{ij}(\omega) = \int_0^\infty R_{ij}(\tau)\cos(\omega\tau)\,d\tau \quad \leftrightarrow \quad R_{ij}(\tau) = \frac{2}{\pi}\int_0^\infty b_{ij}(\omega)\cos(\omega\tau)\,d\tau$$

2.3.6 Symmetry

A single floater is symmetric in its x-axis. Therefor the symmetric (x, z, θ) and anti-symmetric (y, ϕ, ψ) equations of motions can be uncoupled, and there is no need to perform the calculations for the added mass and damping terms of the coupling between these symmetric and anti-symmetric motions, see equation 2.23 as an example.

$$A = \begin{bmatrix} a_{11}(\omega) & 0 & a_{13}(\omega) & 0 & a_{15}(\omega) & 0 \\ 0 & a_{22}(\omega) & 0 & a_{24}(\omega) & 0 & a_{26}(\omega) \\ a_{31}(\omega) & 0 & a_{33}(\omega) & 0 & a_{35}(\omega) & 0 \\ 0 & a_{42}(\omega) & 0 & a_{44}(\omega) & 0 & a_{46}(\omega) \\ a_{51}(\omega) & 0 & a_{53}(\omega) & 0 & a_{55}(\omega) & 0 \\ 0 & a_{62}(\omega) & 0 & a_{64}(\omega) & 0 & a_{66}(\omega) \end{bmatrix} \qquad \text{(Eq. 2.23)}$$

Note: For multiple floating bodies next to each other this theory cannot be applied. Since there can be cross coupling between the platforms.

2.3.7 Other damping effects

As stated, solving the radiation potential only considers forces of the fluid perpendicular to the body. Nevertheless, there are non-linear viscous damping effects that act as forces on the floater, like:

- Friction damping
- Eddy-making damping
- Lift damping
- Bilge keel damping

Mostly the effect of these coefficients is small compared to the (potential) hydrodynamic damping but can play a major role in roll motion for specific type of keels. Since the effects are non-linear, they can only be considered when solving the time domain equation of motion. In this report they are not further taken into account.

2.3.8 Wave excitation Forces

Next to the hydrodynamic coefficients the first order wave excitation force can be calculated with the principles of potential theory. It is built up out of the potential of the undisturbed wave Φ_w for the Froude-Krilov force and the diffracted wave potential Φ_d for the diffraction force. See Appendix A for further calculations.

The first order wave force is frequency dependent and often expressed with respect to the center of gravity of the body in terms of an amplitude response $\frac{F_a}{\zeta_a}(\omega)$ and a phase shift $\epsilon_{F\zeta}(\omega)$ with respect to the incoming wave. These coefficients for bodies can be calculated with diffraction software, see chapter 3.

2.3.9 Other wave excitation forces

Next to the first order wave force, second order wave drift forces exist. These are non-linear effects of the motion of the body in waves and can be subdivided into mean wave drift forces and low-frequency wave drift forces (Journée & Massie, 2001). These are not further considered in this report.

2.4 Equation of motion with joints

This section elaborates on the implementation of joints as springs between two floaters. The non-linear forcing on the floaters centers of gravity is derived and for frequency domain calculations further linearized.

2.4.1 Joints as springs

The scope of this research focusses on implementing the connections as springs between the floating bodies. Every floater is connected with two joints to another floater, see Figure 2.1.

Every connection is treated as 6 springs, see Figure 2.3: *1 axial, 2 transversal and 3 rotational springs in a single connection*Figure 2.3 as example:

- 1 Axial spring (k_a)
- 2 Transversal springs (k_s)
- 2 rotational springs (bending) (k_r)
- 1 rotational spring (torsion) (k_t)
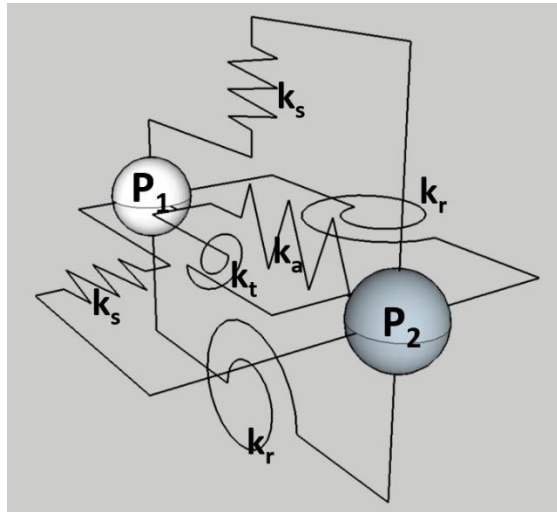
Figure 2.3: 1 axial, 2 transversal and 3 rotational springs in a single connection.

The determination of the joint stiffnesses is based on a circular connection and further evaluated in Appendix L.

2.4.2 Equation of motion with joints

The equation of motion in time domain given in equation 2.11, can be extended for additional forcing, next to the first order wave forces, described in section 0. Accordingly, the forcing by interconnecting joints between floaters is added to the equation of motion:

(Eq. 2.24)

$$(M + A_\infty)\,\underline{\ddot{u}}(t) + \int_0^\infty R(\tau)\underline{\dot{u}}(t - \tau)d\tau + C\underline{u}(t) = \underline{F_w}(t) + \underline{F_{joint}}(t)$$

M Mass of body

A_∞ Added mass matrix at infinite frequency

R Retardation function matrix

C Restoring spring matrix

$\underline{F}_w(t)$ Wave Excitation force vector

$\underline{F}_{joint}(t)$ Joint forcing (restrains)

$\underline{u}$ Motion vector

2.4.3 Euler-Lagrange equation

A straight forward and clear manner to obtain the equations of motion of a general dynamic system is making use of the Euler-Lagrange equations:

$$\frac{d}{dt}\frac{\partial \mathcal{L}}{\partial \dot{u}_i} = \frac{\partial \mathcal{L}}{\partial u_i} \qquad \text{(Eq. 2.25)}$$

$$\mathcal{L} = \mathcal{T} - \mathcal{V} \qquad \text{(Eq. 2.26)}$$

Where $\mathcal{T}$ and $\mathcal{V}$ are respectively the total kinetic, and potential energy in a system. The forcing by the joints on the system can be derived in a similar manner.

In a mass spring system (without gravity), the kinetic energy part in the Lagrangian, $\mathcal{L}$, contributes to the inertial forces and the Potential energy to the restoring forces of the spring(s). As an example the Lagrangian is solved for a single mass spring system in Appendix B.

2.4.4 Joints in multiple degrees of freedom

The method of Euler-Lagrange can be applied to determine the connection stiffness forcing: F_{joint}. The potential energy of all springs needs to be evaluated:

$$\mathcal{V} = \frac{1}{2}\left(k_a\left(\Delta x_{joint}\right)^2 + k_s\left(\Delta y_{joint}\right)^2 + k_s\left(\Delta z_{joint}\right)^2 + k_t\left(\Delta \phi_{joint}\right)^2 + k_r\left(\Delta \theta_{joint}\right)^2 \right. \qquad \text{(Eq. 2.27)}$$
$$\left. + k_r\left(\Delta \psi_{joint}\right)^2\right)$$

$$F_{joint,i} = \frac{-\partial \mathcal{V}}{\partial u_i} \qquad \text{(Eq. 2.28)}$$

With i the degrees of freedom of the system.

Relative motions between connection points

In order to calculate the potential energy that is stored in the springs, the new coordinates of a connection point P must be calculated after rotation around the CoG. This can be done by using rotational matrices. The new position can be calculated with the help of rotation matrices:

$$\left[P'_{x,i}, P'_{y,i}, P'_{z,i}\right]^T = R_i\left[P_x, P_y, P_z\right]^T \qquad \text{(Eq. 2.29)}$$

With $i = \phi, \theta \text{ or } \psi$

$$R_\phi = \begin{bmatrix} 1 & 0 & 0 \\ 0 & \cos\phi & -\sin\phi \\ 0 & \sin\phi & \cos\phi \end{bmatrix}, R_\theta = \begin{bmatrix} \cos\theta & 0 & \sin\theta \\ 0 & 1 & 0 \\ -\sin\theta & 0 & \cos\theta \end{bmatrix}, R_\psi = \begin{bmatrix} \cos\psi & -\sin\psi & 0 \\ \sin\psi & \cos\psi & 0 \\ 0 & 0 & 1 \end{bmatrix}$$ (Eq. 2.30)

This is for an axis system where the rotations are counter clockwise. The displacement of the connection point in its local axis system is the subtraction of the original coordinate:

$$[x_{P,i}, y_{P,i}, z_{P,i}]^T = [P'_{x,i}, P'_{y,i}, P'_{z,i}]^T - [P_x, P_y, P_z]^T$$ (Eq. 2.31)

The summation of all possible displacements of the connection points, due to motion around the center of gravity can then be summarized as:

$$x_P = x + x_{P,\phi} + x_{P,\theta} + x_{P,\psi} = x + x_{P,\theta} + x_{P,\psi}$$ (Eq. 2.32)

$$y_P = y + y_{P,\phi} + y_{P,\theta} + y_{P,\psi} = y + y_{P,\phi} + y_{P,\psi}$$ (Eq. 2.33)

$$z_P = z + z_{P,\phi} + z_{P,\theta} + z_{P,\psi} = z + z_{P,\phi} + z_{P,\theta}$$ (Eq. 2.34)

$$\phi_P = \phi$$ (Eq. 2.35)

$$\theta_P = \theta$$ (Eq. 2.36)

$$\psi_P = \psi$$ (Eq. 2.37)

Connecting the floaters

A single connection is connected from a point P1 on floater 1 and to point P2 on floater 2 (P11 and P12 in Figure 2.1: Overview of the geometry of the structure, sign convention and wave direction. Figure 2.1 for example). The above procedure can be performed with the following input:

- For P1:
    - Location of point P1 on axis system of floater 1: $P1: (P1_{x1}, P1_{y1}, P1_{z1})$
    - Motions of floater one in CoG: $[x, y, z, \phi, \theta, \psi]^T = [x_1, y_1, z_1, \phi_1, \theta_1, \psi_1]^T$
    - Results in local displacements of connection system: $u_{P1} = [x_{P1}, y_{P1}, z_{P1}, \phi_{P1}, \theta_{P1}, \psi_{P1}]^T$
- For P2:
    - Location of point P2 on axis system of floater 2: $P2: (P2_{x2}, P2_{y2}, P2_{z2})$
    - Motions of floater two in CoG: $[x, y, z, \phi, \theta, \psi]^T = [x_2, y_2, z_2, \phi_2, \theta_2, \psi_2]^T$
    - Results in local displacements of connection system: $u_{P2} = [x_{P1}, y_{P1}, z_{P1}, \phi_{P1}, \theta_{P1}, \psi_{P1}]^T$

The relative displacement of the two ends of a connection (one connected to floater 1 and one to floater 2) that need to be evaluated in equation 2.27 can be composed:

$$\Delta\underline{u}_{joint} = \underline{u}_{P1} - \underline{u}_{P2}$$ (Eq. 2.38)

With: $\Delta\underline{u}_{joint} = [\Delta x_{joint}, \Delta y_{joint}, \Delta z_{joint}, \Delta\phi_{joint}, \Delta\theta_{joint}, \Delta\psi_{joint}]^T$

The resulting reaction force from the joint is dependent, with respect to the floaters center of gravity, is dependent on the joint stiffness and the motions of both floaters:

$$\rightarrow \underline{F}_{joint}\big(\underline{u}(t),\underline{k}\big)$$

with $\underline{k} = [k_a, k_s, k_s, k_t, k_r, k_r]^T$.

Damping from joints

To cover material damping from the joints, the same procedure can be applied for linear joint dampers on the system. Simply by replacing the motion and stiffness terms in the obtained joint forcing equation with the velocity at the floaters' centers of gravity $\big(\underline{v}(t)\big)$ and linear damping coefficient (d). In this case the total forcing from the joint would become:

$$\underline{F}_{joint}\big(\underline{u}(t),\underline{k},\underline{v}(t),\underline{d}\big) = \underline{F}_{joint,springs}\big(\underline{u}(t),\underline{k}\big) + \underline{F}_{joint,dampers}\big(\underline{v}(t),\underline{d}\big)$$

It must be said that these are linear approximations of the reality. Joint damping is not further applied in the result section, but is incorporated in the models, described in chapter 4.

Multiple joints

This same procedure can be repeated for multiple facing connection points on side-by-side or matrix configured floaters. In this report there is focused on two joints connecting two floaters at the ends (see figure Figure 2.1). Equation 2.27 is then extended to 12 terms instead of 6 terms (6 springs per connection) that are incorporated into the calculation of the potential energy equation.

Frequency domain Spring Matrix

In frequency domain calculations it is desired to implement the joint interaction in the form of a linear stiffness matrix. The frequency domain equation of motion presented in equation 2.9, will have the following adjustment:

$$\big(-\omega^2\big(M + A_H(\omega)\big) + i\omega B_H(\omega) + C + C_{joint}\big)\underline{\tilde{u}}(\omega) = \underline{\tilde{F}}(\omega) \qquad \text{(Eq. 2.39)}$$

$\quad M$ Mass matrix

$\quad A$ Added mass matrix

$\quad B$ Hydrodynamic damping matrix

$\quad C$ 12x12 Restoring Stiffness matrix

$\quad C_{joint}$ 12x12 Joint Stiffness matrix

$\quad \underline{\tilde{F}}(\omega)$ Complex excitation force vector in frequency domain

$\quad \underline{\tilde{u}}(\omega)$ Complex Motion vector in frequency domain

Since all calculations in frequency domain are linear, this stiffness matrix is related to the linearized stiffness joint forcing vector in time domain. The linearization of this joint forcing vector is further described in Appendix C. It can be transformed to a matrix notation with the following similarity.

$$\underline{F}_{joint,linear}\big(\underline{u}(t)\big) = -C_{joint}\underline{u}(t) \qquad \text{(Eq. 2.40)}$$

Note: the minus is due to the difference in side (left or right of the equal sign) of the equation where the joint forcing is implemented.

Since the forcing vector is linear, the entries of the stiffness matrix can be composed by taking the derivative with respect to each degree of freedom for every vector input:

$$C_{joint} = \begin{bmatrix} c_{1,1} & \cdots & c_{1,12} \\ \vdots & \ddots & \vdots \\ c_{12,1} & \cdots & c_{12,12} \end{bmatrix} = -1 \cdot \begin{bmatrix} \dfrac{\partial F_1}{\partial u_1} & \cdots & \dfrac{\partial F_1}{\partial u_{12}} \\ \vdots & \ddots & \vdots \\ \dfrac{\partial F_{12}}{\partial u_1} & \cdots & \dfrac{\partial F_{12}}{\partial u_{12}} \end{bmatrix}$$

An overview of the forcing vectors and resulting linear spring matrix can be found in Appendix D.

2.5 Conclusion

In this section the equations of motion for the time and frequency domain model were derived and are:

Time domain: non-linear

$$(M + A_\infty)\,\underline{\ddot{u}}(t) + \int_0^\infty R(\tau)\underline{\dot{u}}(t - \tau)d\tau + C\underline{u}(t) = \underline{F}_w(t) + \underline{F}_{joint}(t)$$

Time domain: linear

$$(M + A_\infty)\,\underline{\ddot{u}}(t) + \int_0^\infty R(\tau)\underline{\dot{u}}(t - \tau)d\tau + C\underline{u}(t) = \underline{F}_w(t) + \underline{F}_{joint,linear}(t)$$

Frequency domain (linear)

$$\left(-\omega^2\big(M + A_H(\omega)\big) + i\omega B_H(\omega) + C + C_{joint}\right)\underline{\tilde{u}}(\omega) = \underline{\tilde{F}}(\omega)$$

Where the joint forcing vector and joint stiffness matrix are derived with the potential energy part in the Euler-Lagrange equation.

3. Diffraction software

Numerical modelling of floaters is much less expensive then performing scale model tests in a basin and gives in a lot of circumstances very accurate approximations. As described before an import bases of the numerical modelling are the hydrodynamic coefficients and wave excitation forces via potential theory. The most common method to do the modelling is by making use of diffraction software that uses boundary element method (BEM), also known as the panel method, applied in so called diffraction software.

This method is based on potential flow theory and is therefore somewhat limited by linear calculations. Nevertheless, it is still much faster than other methods like computational fluid dynamics (CFD) or smoothed-particle hydrodynamics (SPH).

The coefficients that can be obtained with diffraction software are the hydrodynamic coefficients described in Section 2.3.4, being the frequency dependent added mass $a(\omega)$, hydrodynamic damping $b(\omega)$, wave excitation force amplitude response $\frac{F_a}{\zeta_a}(\omega)$ and phase shift $\epsilon_{F\zeta}(\omega)$ with respect to the incoming wave.

3.1 BEM-solvers

BEM is a numerical technique which uses systems of partial differential equations formulated into the boundary integral form. BEM codes employ the method of Green's functions to transform a flow problem into a problem of source distribution on the body surface. BEM codes may be applied to varying engineering problems, and when used in a hydrodynamic context, BEM is used to solve for the scatter and radiated velocity potentials, which are solved separately, and which arise from the interaction of a harmonic linear wave field with a body located within that field. The scattering potential is solved for the body when it is held fixed and may be used to determine the exciting force acting on the body due to the wave action. The radiating potential, wherein the potential is found for a moving body in the absence of incident waves, is commonly resolved into components in phase with the body acceleration and the body velocity and gives rise to the added-mass and radiation damping terms. (Penalba, Kelly, & Ringwood, 2017)

Different BEM software packages for hydrodynamic calculations are available on the market, being for example:

- WAMIT
- Aquaplus
- Aqwa
- WADAM
- Diffrac
- NEMOH

Making use of commercial BEM software can be costly and several different simulations are mostly required. The following BEM solvers are issued in this study:

- DIFFRAC
  Scale model tests for floating solar panels have been executed by Marin (December 2017), and at the time simulations were performed with their in-house diffraction software.
- AQWA
  The TU Delft has license for ANSYS, including the package AQWA
- NEMOH
  This is an open source Matlab code developed by the École Centrale de Nantes in 2014

Important in all these BEM solvers is that it needs to be understood how it should be used in a proper way, to produce realistic results.

3.1.1 Assumptions in diffraction software

Some additional information is given about diffraction solvers. The solvers solve the potential functions, and this can be interpreted as the floater being excited with infinitely small amplitudes for different frequencies. For the forcing the results is then scaled to the amplitude response per meter wave amplitude. In general, this means that the linearization around waterline causes the problem that it is not good applicable for large excitations. Nevertheless, diffraction software has shown to be a commonly used tool in the modelling of wave energy converters (also small ones). For small floaters the effect of diffraction and wave shielding will be very low, compared to larger objects.

3.1.2 Mesh

A mesh of the floating body build of panels needs to be created to solve the potential equations in diffraction software. It should be mimicked that flow goes around the object. This can be achieved in two ways: implementing point sources on the grid panels or make use of distributed sources. Most diffraction software makes use of point sources. Therefor the number of panels should be sufficient for two reasons: to capture high wave frequencies (small wave lengths) and to simulate the right shape of the floater (sufficient point sources close to the boundary).

The floating body does not need to be modelled above the still waterline, since diffraction software linearizes around the waterline. Hence, the floating body is seen as an infinite high body with an extrusion at the waterline area. Most diffraction software's have their own meshing tool. An example of bodies with a different number of panels, generated with NEMOH's meshing tool are given in Figure 3.1.
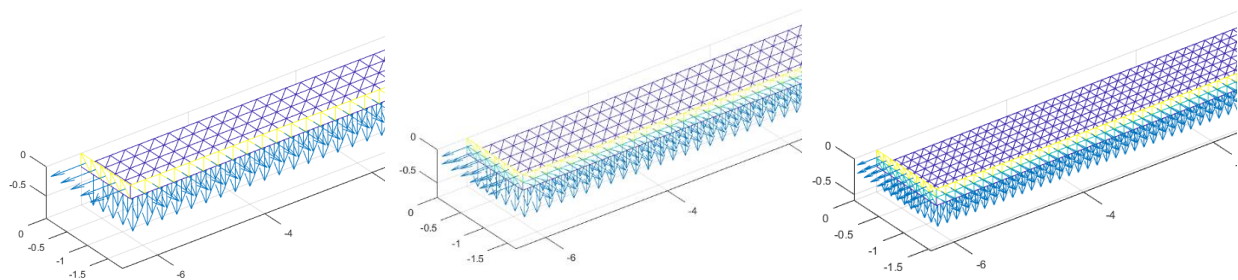

Figure 3.1: Mesh for a floater with 300, 500 and 1000 panels

The mesh is created for half the floater and mirrored in the y-axis. More information about creating a mesh can be found in Appendix E.

3.1.3   Joints

The application of joints in diffraction software for the calculation of the first order hydrodynamic forces is not necessary since not moving objects are considered in the calculation. Although when the size of the joints is not very small compared to the floater size (think about very large fenders), and are (partially) submerged, they can have an overall effect on the fluid behavior.

Note: For the calculation of second order wave drift forces the floaters motions are of importance and therefore the joints should be implemented beforehand for the calculation of the so-called drift quadratic transfer functions. Not further evaluated in this report.

3.2   Comparison for different BEM-solvers

In order to verify the open source software NEMOH, a comparison is made with the hydrodynamic coefficients (Hyd-files) obtained with DIFFRAC. This is done for a single floater, as described in Table 3.1. At the same time a comparison is made with ANSYS' AQWA, available via the TU Delft License.

Table 3.1: Steel floater used in Scale model tests:

$\rho_{water}\ \left[\dfrac{kg}{m^3}\right]$	1025
$d\ [m]$	24
$L\ [m]$	-
$B\ [m]$	-
$T\ [m]$	-
$KG\ [m]$	-
$m\ [kg]$	-
$[r_x, r_y, r_z]$	-

3.2.1   Number of panels

Different number of panels composed width NEMOH's built-in mesh tool can be seen in Figure 3.1. The appropriate number of panels needed is related to the wavelengths that is desired to be taken into account.

As a rule of thumb the minimum required number of panels (William Otto, Marin 2018) should be at least 5 per occurring wavelength. Knowing the wetted surface area an estimation can be made of the number of panels required per wave frequency that is calculated.

The wave length corresponds to the wave frequency via the dispersion relation and can be calculated iteratively:

$$\lambda = \frac{g}{2\pi} T^2 \tanh\left(2\pi \frac{h}{\lambda}\right)$$

(Eq. 3.1)

The minimum number of panels on the floater that are at least required per wave length can then be calculated accordingly:

$$N_{panels} = \frac{A_{wetted}}{\left(\frac{\lambda}{5}\right)^2}$$

The result is summed up in the following table:

Table 3.2: Estimation of the number of panels minimal required in mesh of the steel floater for higher frequencies

$\omega\ [rad/s]$	$\lambda\ [m]$	N_{panels}
8	0.96	955
10	0.62	2290
25	0.10	88056
50	0.024	1,528,750

Marin's DIFFRAC hyd-files consists of 2000 panels on one floater. The same floater is built in NEMOH and compared for different number of panels to optimize the code before scaling up to multiple floaters. NEMOH considers symmetry of the floater in the x-axis, this means that basically the number of panels can be halved.

3.2.2   Comparison with DIFFRAC

A comparison is made between the pre-delivered DIFFRAC Hyd-files by Marin and the created Hyd-files with NEMOH. In order to estimate the difference between the Hyd-files, the NEMOH files (with different amount of panels) are compared with the original DIFFRAC file (2000 panels). See for example Figure 3.2.
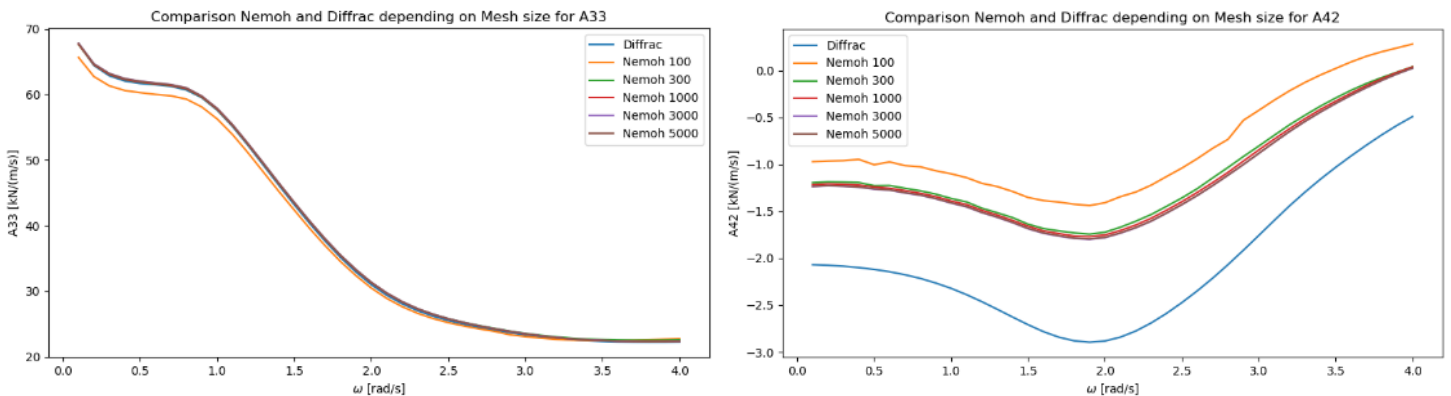

Figure 3.2: Added mass in heave-heave and roll-sway motion for different mesh sizes.

A good way to quickly analyze the similarity between both files is looking at the correlation between both. Where a value of 1 indicates a perfect positive correlation. Hence, this indicates if the coefficients

have a similar curve shape. Nevertheless, this gives no indication of the amplitude of the curves. Therefor the RMS-ratio is used: $RMSr = \frac{RMS_{Diffrac}}{RMS_{NEMOH}}$. When this value is around 1, the curves have equal values. When it is below 1, NEMOH gives higher values than DIFFRAC.

Since, the single floater's equation of motion can be decomposed in symmetric and anti-symmetric motions, only the non-zero coefficients (cross terms) are analyzed. Due to its double symmetry this concerns only the diagonal coefficients and surge-pitch and sway-roll coefficients.

By comparing these results on the above discussed criteria, leads to the plot shown in Figure 3.3 and Figure 3.4, respectively the correlation and RMSr for different amount of panels in NEMOH with the DIFFRAC file. The usage of lines instead of bullets is a not very proper manner of representing, since the correlation and RMSr are specific for a certain coefficient and has no values in between. Nevertheless, a line representation gives an overview of where certain values are higher than others.
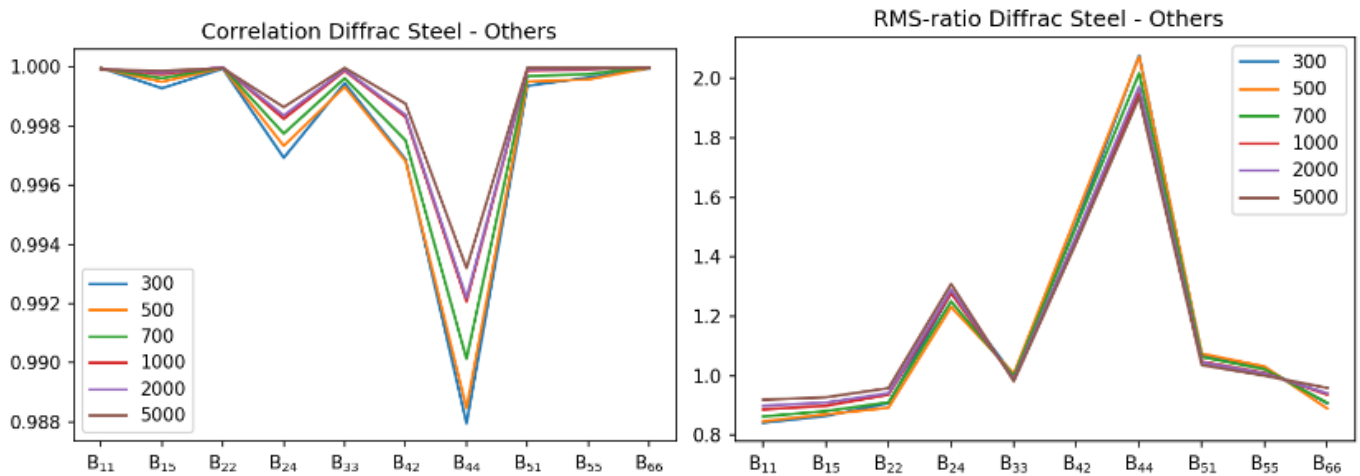

Figure 3.3: Correlation and RMS-ratio for damping coefficients for different number of panels in Nemoh w.r.t. Diffrac
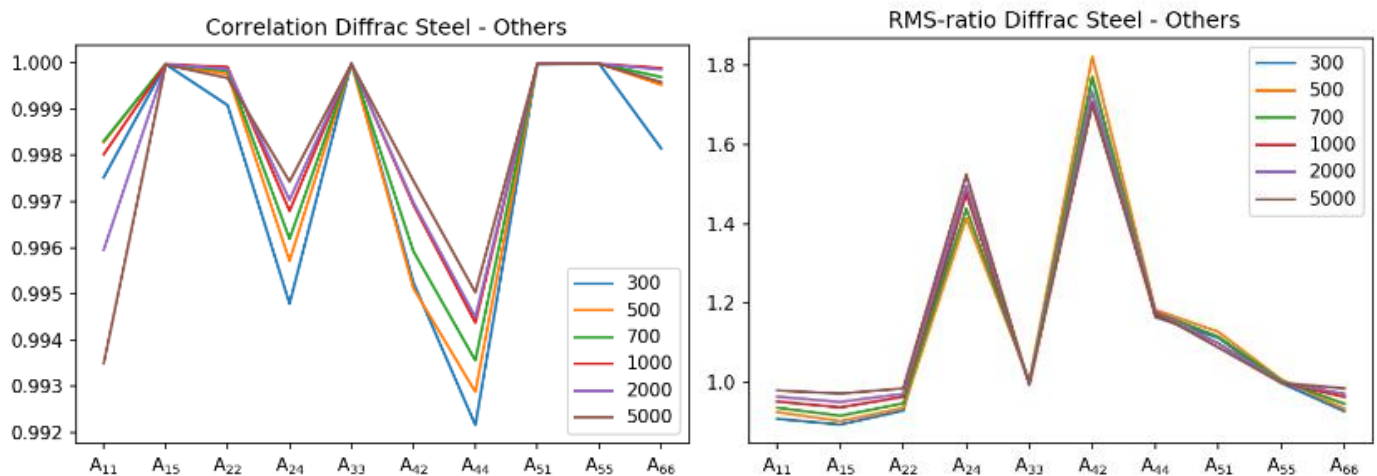
It can clearly be seen that the number of panels has an influence on the similarity of NEMOH's and DIFFRAC's result. The correlation is for all number of panels high and the RMS-ratio gives especially differences in the roll-motion, up to half the value of DIFFRAC.

For all cases the correlation is very close to 1, and therefore the coefficients have the same shape. But it can also be seen that the Added Mass and Hydrodynamic Damping have a large difference in RMS for the sway-roll direction. Up to 200% for 2000 panels.

3.2.3   Comparison with AQWA

A closer look is taken on the hydrodynamics coefficients that differ in Figure 3.3 and Figure 3.4, by modelling the floater in AQWA as well. For these coefficients also a difference with AQWA is observed.
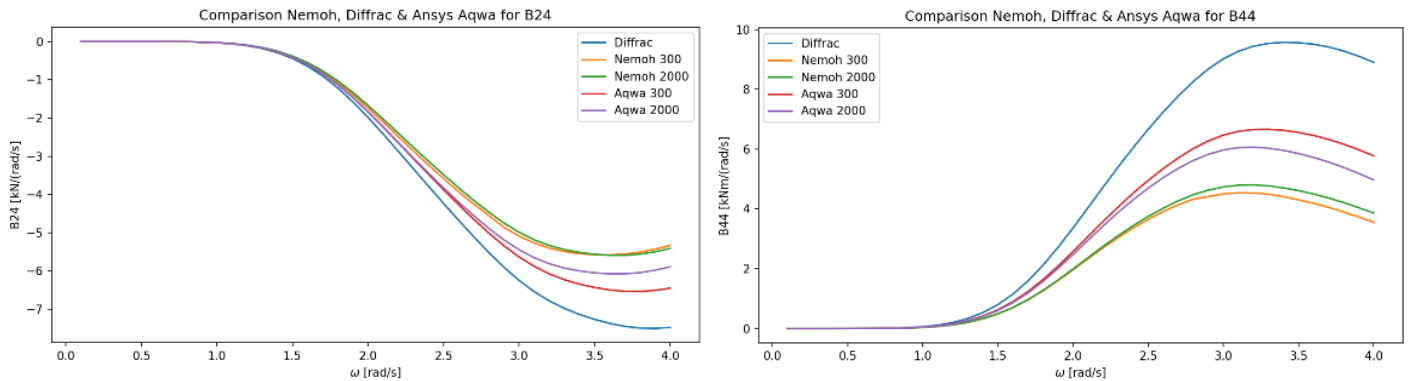

Figure 3.5: largest difference in hydrodynamic damping between AQWA, DIFFRAC and NEMOH for sway-roll and roll-roll motion.

A difference can also be observed between DIFFRAC and AQWA. This is reported to MARIN and the university de Nantes (the developers of DIFFRAC and NEMOH) and will be further investigated.

3.2.4   Phase shift

NEMOH and DIFFRAC have a different representation of the phase shift of the force. See Figure 3.6 and Figure 3.7 where a regular wavefield is applied on two floaters with a certain distance to each other. The forces on floater 1 and floater 2 in heave direction are almost in phase in Figure 3.6, while they follow the wave elevation in Figure 3.7.
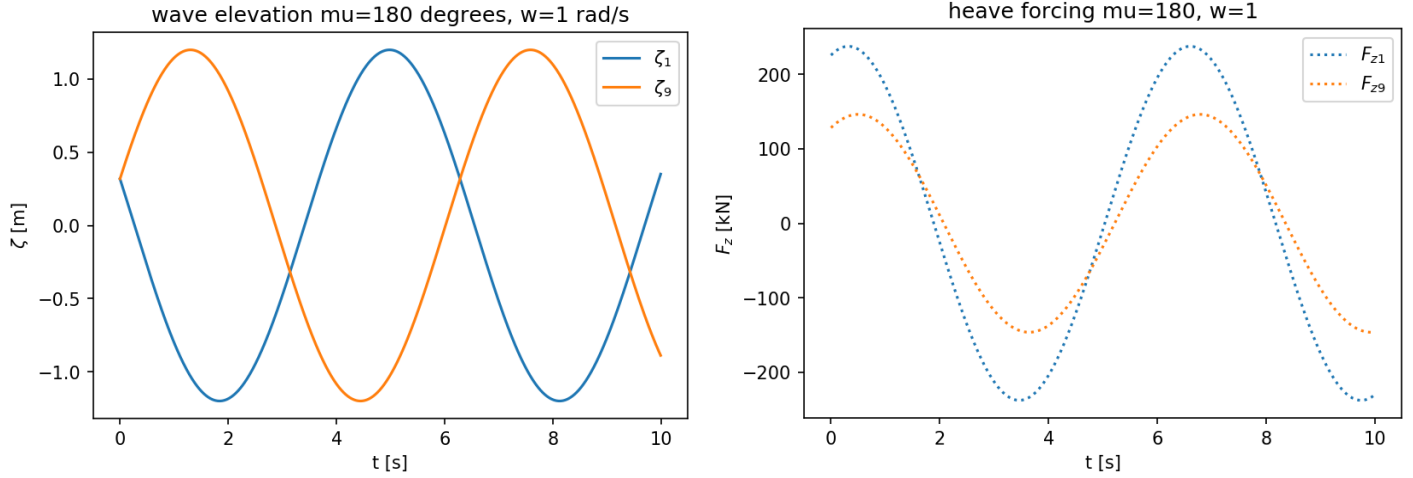
Figure 3.6: Result for DIFFRAC. Wave elevation at CoG of floater 1 and 2 in time (left), heave forcing in time (right)
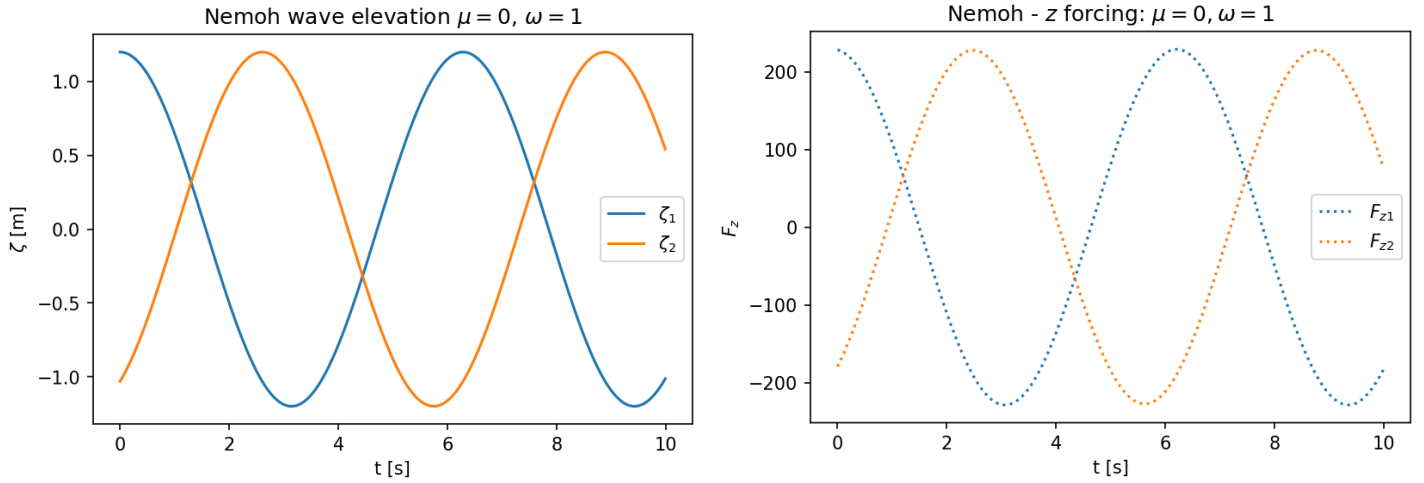

Figure 3.7: Result for NEMOH. Wave elevation at CoG of floater 1 and 2 in time (left), heave forcing in time (right).

This reason for this is that the phase shift in DIFFRAC is with respect to the wave arriving at the floaters own center of gravity. While in NEMOH the phase shift is with respect to the origin in a global axis system. This makes NEMOH's phase shift more applicable for direct use in frequency domain calculations, because the phase shift between the forces on two floaters is correct. DIFFRAC's representation of the phase shift is more applicable for time domain calculations, since the location of the floater could change and with that the location of the floaters center of gravity in the global axis system. The real phase shift with respect to the origin of a global axis system can then be obtained for every time step. The relation between the both phase shifts can be calculated:

$$\epsilon_{DIFFRAC,global} = \epsilon_{DIFFRAC}(\omega) - kx_{CoG}\cos(\mu) - ky_{CoG}\sin(\mu) \qquad \text{(Eq. 3.3)}$$

$$\epsilon_{NEMOH} = -\epsilon_{DIFFRAC,global}$$

Where k is the wavenumber corresponding with the wave frequency via the dispersion relation, see equation 3.1. The reason of the amplitude-decrease noticeable in Figure 3.6 is due to wave shielding

42

effects of other floaters in between the DIFFRAC model used for this phase shift comparison. On top of that the interpretation of the phase shifts in the forcing equation is different in both BEM-solvers, therefor a minus sign is needed to complete the transition. There is more elaborated on the phase shifts in Appendix F.

3.3 Computational time

3.3.1 Convergence

In Figure 3.3 and Figure 3.4 it can be seen that the difference to DIFFRAC converges for a larger number of panels in NEMOH. Therefor it is chosen to make use of 1000 panels per floater (2000 accounting for symmetry). Same as the DIFFRAC file. This is also in accordance with the number of panels needed to capture higher required frequencies, see Table 3.2. Next to that it limits the computational time of the BEM-solver.

3.3.2 Interpolation

Hydrodynamic coefficients are characterized by slowly changing slopes, therefor it is possible to let the BEM-solver calculate the hydrodynamic coefficients with a respectively large frequency step ($\Delta\omega = 0.1\ rad/s$). Although this is quite large for further calculations in time and frequency domain, since the occurring wave frequencies in the wave spectrum are quite narrow, see Figure 1.4. Therefore, it is advisable to interpolate the hydrodynamic coefficients for a smaller frequency step size afterwards (in this case $\Delta\omega = 0.01 rad/s$). The added mass and hydrodynamic damping coefficients can be linearly straight away, while the forcing phase shift needs some extra attention. Where the phase shift is in the range $[-\pi, \pi)$, an interpolation would cause errors. Therefor first the frequency response function is composed of the phase shift and the amplitude response.

$$H_{F\zeta} = \frac{F_a}{\zeta_a} e^{i\epsilon_{F\zeta}}$$

(Eq. 3.4)

The real and imaginary part of the frequency response function are then interpolated. The interpolated phase shift and amplitude response are then obtained with the principles of a complex plane:

$$\frac{F_a}{\zeta_a} = |H_{F\zeta}|, \epsilon_{F\zeta} = \arg(H_{F\zeta})$$

(Eq. 3.5)

3.4 Conclusion

There are multiple commercial software's available that solve BEM-problems. Nevertheless, the only widely used open source-tool to do this is NEMOH. NEMOH gives good global results in the calculation of all hydrodynamic coefficients compared to commercial software's like DIFFRAC and AQWA.

Phase shifts in BEM solvers are treated differently. In NEMOH the phase shift is given with respect to the incident wave at a global origin, whereas in DIFFRAC these are given with respect to the incident wave at the floaters own center of gravity.

An important factor in the generation of the coefficients is the number of panels for the mesh of the floaters being modelled. This number of panels is based on the highest wave frequency that needs to be considered (see also appendix I).

Interpolation of the hydrodynamic coefficients afterwards is beneficial. It decreases the computational time of NEMOH and increases the ability to capture the whole narrow-banded wave spectrum.

4. Numerical models

This section elaborates on the implementation of the presented system with the equations of motion and the accessory coefficients presented in chapter 2. Firstly, the time domain model is discussed, followed by the frequency domain model.

4.1 Time-domain model

Equation of motion

The MDoF time domain equation of motion was shown, known as Cummin's equation. Where from now on $F(t)$ is represented as the sum of wave forcing and the forcing from the interconnecting joints between two floaters (12 DoF): $F(t) = F_w(t) + F_{joint}(t)$.

$$\left(M + \begin{bmatrix} a_{1,1,\infty} & \cdots & a_{1,12,\infty} \\ \vdots & \ddots & \vdots \\ a_{12,1,\infty} & \cdots & a_{12,12,\infty} \end{bmatrix}\right)\begin{bmatrix} \ddot{u}_1 \\ \vdots \\ \ddot{u}_{12} \end{bmatrix} + \int_0^\infty \begin{bmatrix} R_{1,1}(\tau) & \cdots & R_{1,12}(\tau) \\ \vdots & \ddots & \vdots \\ R_{12,1}(\tau) & \cdots & R_{12,12}(\tau) \end{bmatrix}\begin{bmatrix} \dot{u}_1(t-\tau) \\ \vdots \\ \dot{u}_{12}(t-\tau) \end{bmatrix} d\tau \hspace{1cm} \textit{(Eq. 4.1)}$$

$$+ \begin{bmatrix} c_{1,1} & \cdots & c_{1,12} \\ \vdots & \ddots & \vdots \\ c_{12,1} & \cdots & c_{12,12} \end{bmatrix}\begin{bmatrix} u_1 \\ \vdots \\ u_{12} \end{bmatrix} = \begin{bmatrix} F_{w,1}(t) \\ \vdots \\ F_{w,12}(t) \end{bmatrix} + \begin{bmatrix} F_{joint,1}\left(\underline{u}(t)\right) \\ \vdots \\ F_{joint,12}\left(\underline{u}(t)\right) \end{bmatrix}$$

4.1.1 Model overview

A time integration model is created to solve the motions of 2 interconnected floating bodies, with the open source code NEMOH in MATLAB and Python. The following inputs are required for the calculation of the motions:

- Wave Environment
- Geometry of the floaters and joints
- Specific time input
- Initial conditions

The basic overview of the calculation procedure is given in the flow chart presented in Figure 4.1 and the most important steps will be discussed in the following section.
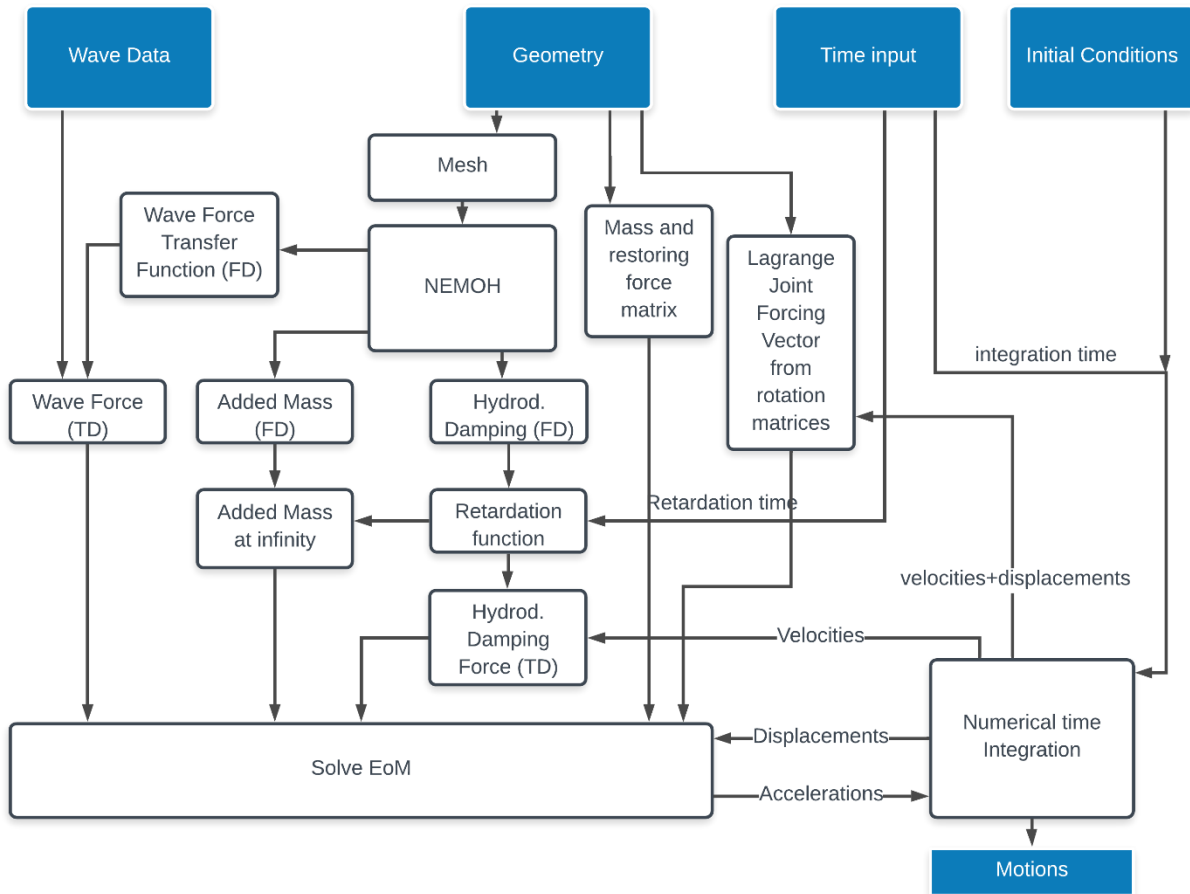
Figure 4.1: Flow chart of the calculation procedure of the Time Domain model

4.1.2 Numerical time integration

Different Numerical time integration methods for initial value problems exist and the following are further discussed in Appendix G:

- Modified Euler
- RK4
- ODE45 (Python)

4.1.3 Wave force input

The wave force input at a certain time t is derived from a wave energy density spectrum $\left(S_\zeta(\omega)\right)$, a phase shift $\left(\epsilon_\zeta(\omega)\right)$, the first order wave force transfer function, $H_{F\zeta}(\omega)$, by means of the superposition principle:

$$F_w(t) = \sum_{n=1}^{N} \Re\left(F_{a_n} e^{-i(\omega t - \epsilon_{F\zeta n} - \epsilon_{\zeta n})}\right)$$

(Eq. 4.2)

With:

Force amplitude component: $\quad\quad\quad\quad\quad F_{a_n} = \sqrt{2 S_{F_n} \Delta\omega}$ *(Eq. 4.3)*

Force energy density spectrum: $\quad\quad\quad S_{F_n} = \left|H_{F\zeta_n}\right|^2 S_{\zeta_n}$ *(Eq. 4.4)*

Phase shift between wave and force amplitude: $\epsilon_{F\zeta_n} = \arg\left(H_{F\zeta_n}\right)$ *(Eq. 4.5)*

The wave component phase shift, ϵ_{ζ_n}, is randomly chosen in the interval $[-\pi; \pi)$ rad. This is because the phase shifts of the individual wave components is lost. Adding a random phase shift, in combination with the wave energy density spectrum will result in a statistically equal wave environment.

4.1.4 Retardation function

As presented in section 2.3.5 the retardation function $R(\tau)$ can be obtained from the hydrodynamic damping coefficient in frequency domain.

$$R(\tau) = \frac{2}{\pi} \int_0^\infty b(\omega) \cos(\omega\tau)\, d\omega$$

(Eq. 4.6)

This means that in a 12DoF system there are as many retardation functions as hydrodynamic damping coefficients in frequency domain: namely 12x12=144. Numerically the integral can be approximated with a summation of the part in the integral:

$$R(\tau) = \sum_{i=1}^{N} b(\omega_i) \cos(\omega_i\tau)\, \Delta\omega$$

(Eq. 4.7)

It automatically follows that when the hydrodynamic damping factor $b(\omega_i)$ has not converged towards zero at ω_N, there could arise in-accuracies in the determination of the Retardation function when truncating in numerical simulations. There will be more elaborated on this influence in Appendix H.

4.1.5 Added Mass at infinite frequency

The formula for the added mass can be reduced to $A = A_\infty = \lim_{\omega\to\infty} a(\omega)$ (Journee & Massie, 2001).

Two ways are presented to obtain this added mass at infinity, namely:

- Higher frequencies can be evaluated by stating them manually in NEMOH and convergence of the added mass to a single value for higher frequencies can be assumed as the added mass at infinity.

- Another method is presented by (Babarit & Delhommeau, Theoretical and numerical aspects of the open source BEM solver NEMOH, 2015) of the Ecole of Nantes, in a more numerical form, encrypted in NEMOH's post processor, where the mean is taken from the added mass formula presented in section 2.3.5. The exact and numerical form of this method is given in equation 4.8 and 4.9. The fact that the frequency dependent added mass, obtained with NEMOH, is finite and the data could be not long enough the results could be inaccurate.

$$\overline{a_{ij,\infty} = a_{ij,\infty}(\omega) + \frac{1}{\omega}\int_{0}^{\infty} R_{ij}(\tau)\sin(\omega\tau)\,d\tau}$$

$$\rightarrow \quad a_{ij,\infty} = \frac{1}{n_\omega}\sum_{n=1}^{N_\omega}\left(a_{ij}(\omega_n) + \frac{1}{\omega_n}\sum_{k=0}^{N_t} R_{ij,k}\sin(\omega_n t_k)\,\Delta t\right)$$

With:

ω	Frequency vector of Hydro coefficients
t	Time vector of retardation function
A	Added mass in time domain
$a(\omega)$	Frequency dependent added mass
R	Retardation function

On the different ways of calculating the added mass is further elaborated on in Appendix I. The method applied in the model is based on adding higher frequencies in the NEMOH model and analyze its convergence.

4.1.6 Convolution integral

Using the convolution integral numerically as a forcing on the floater can be done in the following manner:

$$F_B(t) = \int_{0}^{\infty} R(\tau)\dot{x}(t-\tau)d\tau \quad \rightarrow F_{B_n} = \sum_{i=0}^{n} R_i \dot{x}_{n-i}\Delta t$$

Every time step the retardation function is multiplied with the velocities of previous steps. Meaning that for every time step in the numerical integration scheme the velocities of every previous time step needs to be evaluated.

4.1.7 Limiting convolution time

As can be seen in the retardation function is a decaying function, therefor the amount of velocities at previous time steps back can be limited. This is further evaluated in Appendix H.

4.1.8 Convolution with ODE45

To apply the evaluation of previous time steps in a convenient and not computationally intensive way, variable time stepping is not desired. In that case it is not needed to recompute the retardation function at every time step, since the time step size are known beforehand.

This means that the Python ODE45 solver, with variable time stepping, presented in section 0 is not convenient to use for convolution with one of the output motions. (namely velocity).

There are possibilities to use a state-space model as presented by (Perez & Fossen, 2009) to substitute the convolution integral for calculations with an ODE-solver. This is not further applied in this research.

4.1.9 Convolution with RK4

A 4th order Runge-Kutta (RK4) integration scheme, in comparison to the RK2, uses half time steps in its predictor formulations $\left(t_n + \frac{1}{2}\Delta t\right)$. This implicates that also the retardation function should be calculated at half the time steps. In this way a desired shift can be achieved for the calculation of the predictors. For the predictors the following time steps of the retardation function should be evaluated:

k_1 and k_4: R at $0, 1\Delta t, 2\Delta t, 3\Delta t, ...$

k_2 and k_3: R at $0, \frac{1}{2}\Delta t, \frac{3}{2}\Delta t, \frac{5}{2}\Delta t, ...$

4.1.10 Model specifics

The retardation function and added mass can be calculated upfront for RK4 and RK2 time integration schemes, when the hydrodynamic coefficients of the system in frequency domain are known. Hence, this does need to be done for every single time step in the TD-simulation.

4.1.11 Initial conditions

As a start of the time domain solver, initial conditions need to be stated. Choosing the initial conditions wisely, improves the stability of the model. The implemented initial displacement is based on the static displacement to the force at $t = 0$, based on the forcing in equation 4.11, and the initial velocity is kept trivial:

$$\underline{u}_{initial} = C^{-1}\underline{F}_w(t = 0) \qquad \text{(Eq. 4.11)}$$

$$\underline{v}_{initial} = 0$$

This is only working for initial conditions that experience hydrostatic forcing (i.e. heave, roll and pitch). For other degrees of freedom initial conditions should be stated separately.

4.1.12 Verification

In order to verify the model two adjustments are made to make a comparison with the exact solution and the python ODE-solver.

Comparison with exact solution

By implementing the retardation function as a unit impulse in the following form:

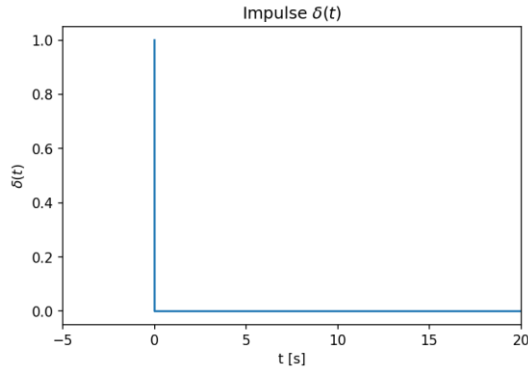$$R(\tau) = \delta(\tau) \cdot b \, dt \qquad \text{(Eq. 4.12)}$$

Figure 4.2: Unit Impulse at t =0

The damping part of the equation of motion is then reduced to a single mass-damper-spring system as we know:

$$\int_0^\infty R(\tau)\dot{u}(t-\tau)d\tau = \int_0^\infty R_u(t-\tau)\dot{u}(t)d\tau = \int_0^\infty b \cdot \delta(t-\tau)\dot{u}(t)d\tau = b\dot{u}(t)$$

(Eq. 4.13)

$$(m + a_\infty)\ddot{u}(t) + b\dot{u}(t) + cu(t) = F_w(t)$$

(Eq. 4.14)

A comparison for the pitch motion is shown in Figure 4.3 together with the absolute error compared to the exact solution, for $\zeta = 0.05 \rightarrow b = 2\zeta\sqrt{c \cdot m}$.
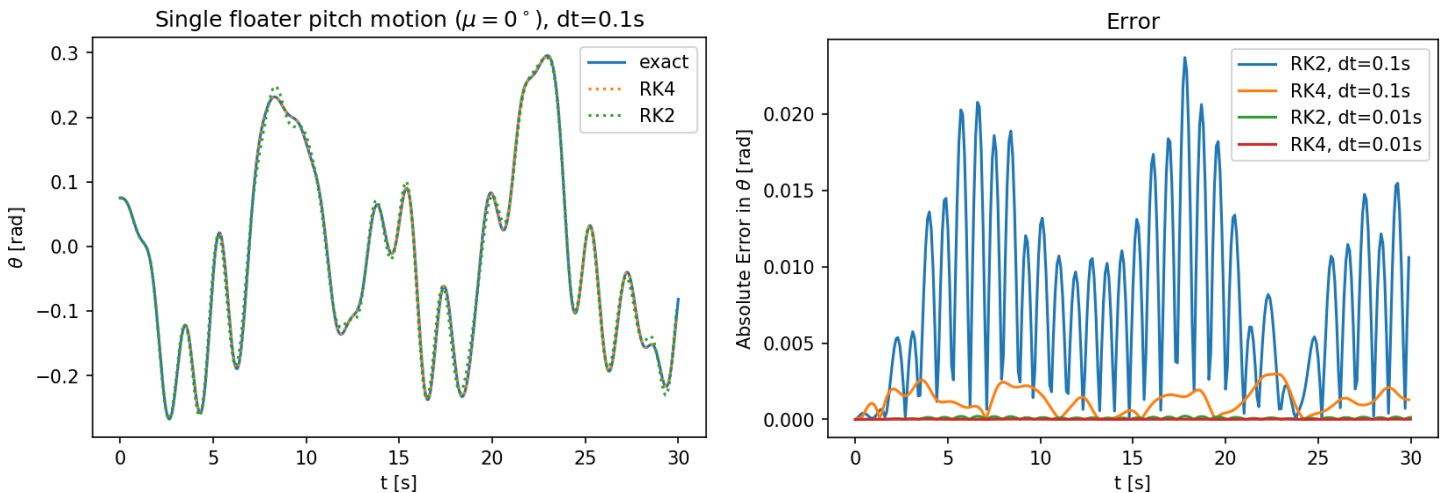

Figure 4.3: comparison of the motion in SDoF floater in pitch for RK2 and RK4 with exact (left) and the absolute error for different time step (right).

It shows that for this case the implemented convolution in the RK2 and RK4 scheme goes well. Decreasing the step size improves the result significantly and that RK4 is more accurate due to its smaller truncation error as described in section 0.

Multiple degrees of freedom
The verification with the exact solution was straightforward to implement for a single degree of freedom system. For multiple degrees of freedom, it is more convenient to verify the model with an ODE45

solver. As mentioned before an ODE45 is not fit to implement a convolution of a retardation function and the velocity vector. Therefor the same procedure with an impulse function as retardation function is applied for every degree of freedom and the equation of motion shown in equation 4.1 reduces to:

$$(M + A_\infty)\,\underline{\ddot{u}}(t) + B\underline{\dot{u}}(t) + C\underline{u}(t) = \underline{F_w}(t) + \underline{F_{joint}}(t) \qquad \text{(Eq. 4.15)}$$

In Figure 4.4 **Fout! Verwijzingsbron niet gevonden.**the results are shown for pitch of the second floater for a model of two floaters in heave and pitch (4DoF) under beam waves ($\mu = 0°$), with the non-linear joint stiffness forcing and a damping ratio of $\zeta = 0.5$ for every degree of freedom.
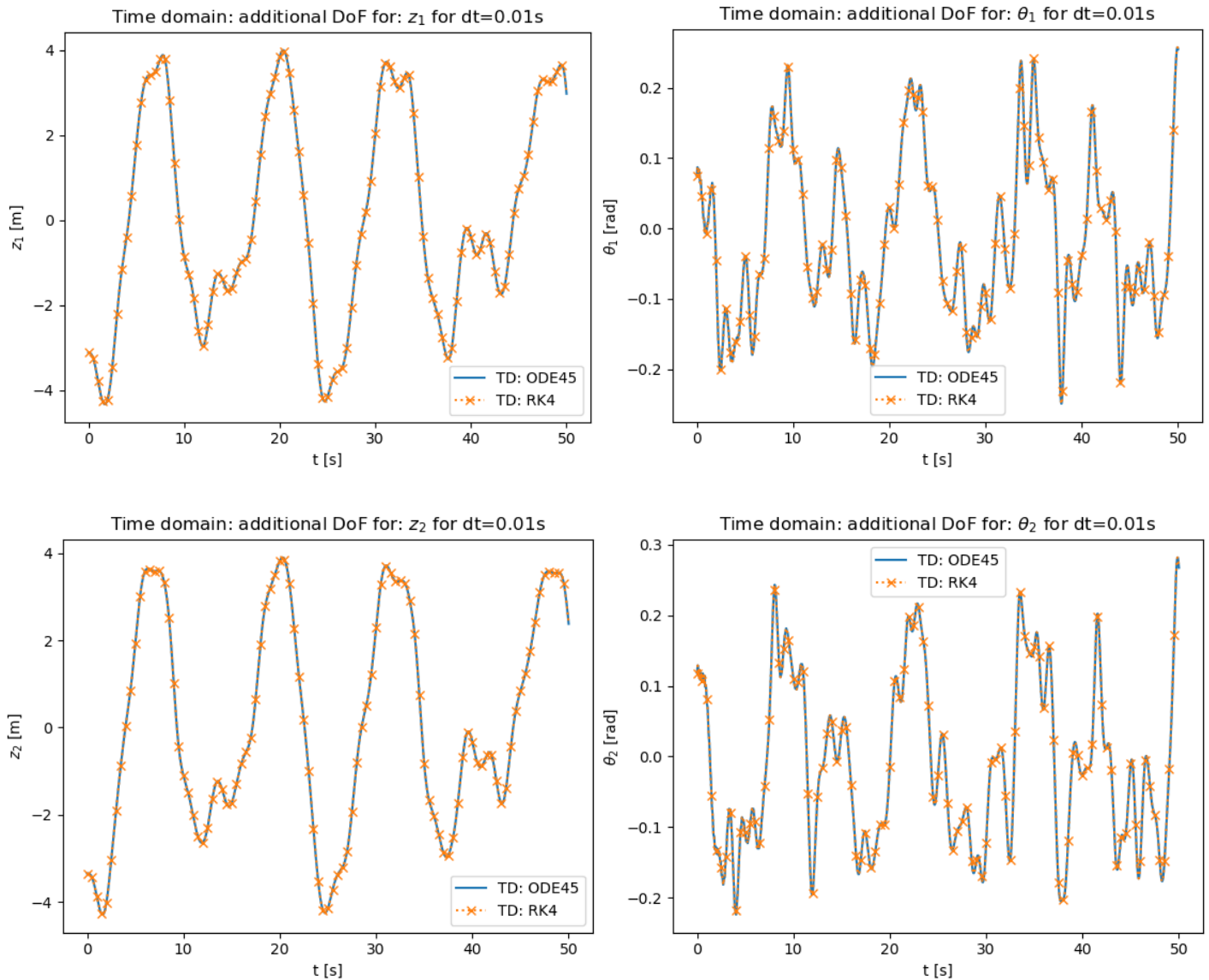

Figure 4.4: comparison of the motion in SDoF floater in pitch for RK2 and RK4 with exact for a 4DoF system (heave and pitch) for a unit pulse retardation function.

Visually it can be seen that the results match. The Error is kept constant, as can be seen in Figure 4.5 for a step size of 0.01s. For multiple degrees of freedom with joint constrains 2nd order Runge-Kutta is not sufficient anymore.
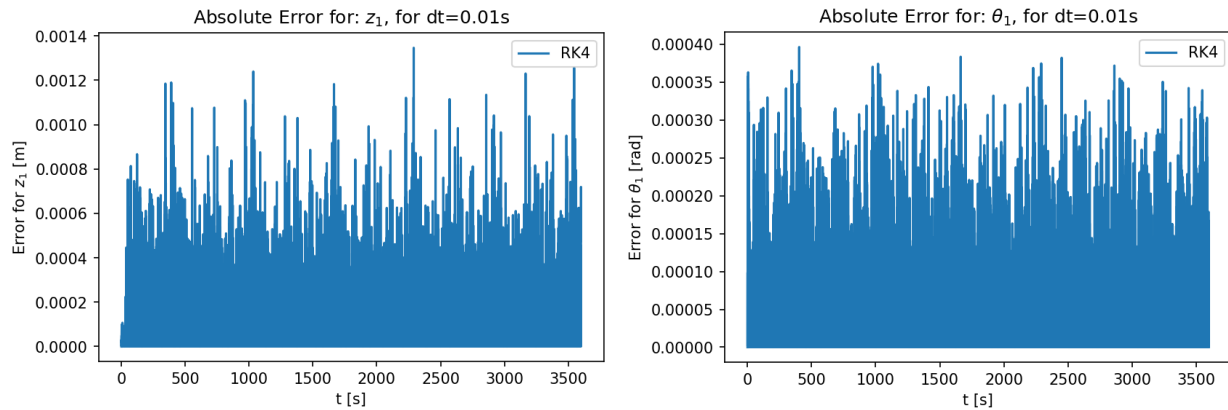

Figure 4.5: Error between ODE45 solver and RK4 solver for first two DoF's in 4 DoF model (heave and pitch of two floaters) for a unit pulse retardation function.

4.1.13 Conclusion

The equation of motion in time domain for multiple degrees of freedom can become rather extensive. The added mass at infinite frequency has to be determined for 12x12DoF, next that the retardation function must be evaluated for a sufficient length in time and convoluted with the velocities at previous time steps. Different time integration methods have been evaluated, whereas a RK4 solver is most applicable to solve the problem. RK2 is not accurate enough and an ODE45 solver is not convenient for taking into account the convolution integral due to its controlled time stepping.

Clear comparisons can be made between the RK4-solver and exact and ODE45 solutions, by replacing the retardation function with a unit impulse function at t=0s. The errors in the RK4 solver with fixed time stepping are then minimal.

4.2 Frequency domain model

Equation of motion

The equation of motion for multiple degrees of freedom is shown in equation 4.16. By implementing the connection matrix, stated in section 0, the equation of motion in frequency domain is:

$$\left(-\omega^2\big(M + A_H(\omega)\big) + i\omega B_H(\omega) + C + C_{joint}\right)\underline{\tilde{u}}(\omega) = \underline{\widetilde{F_w}}(\omega) \qquad \text{(Eq. 4.16)}$$
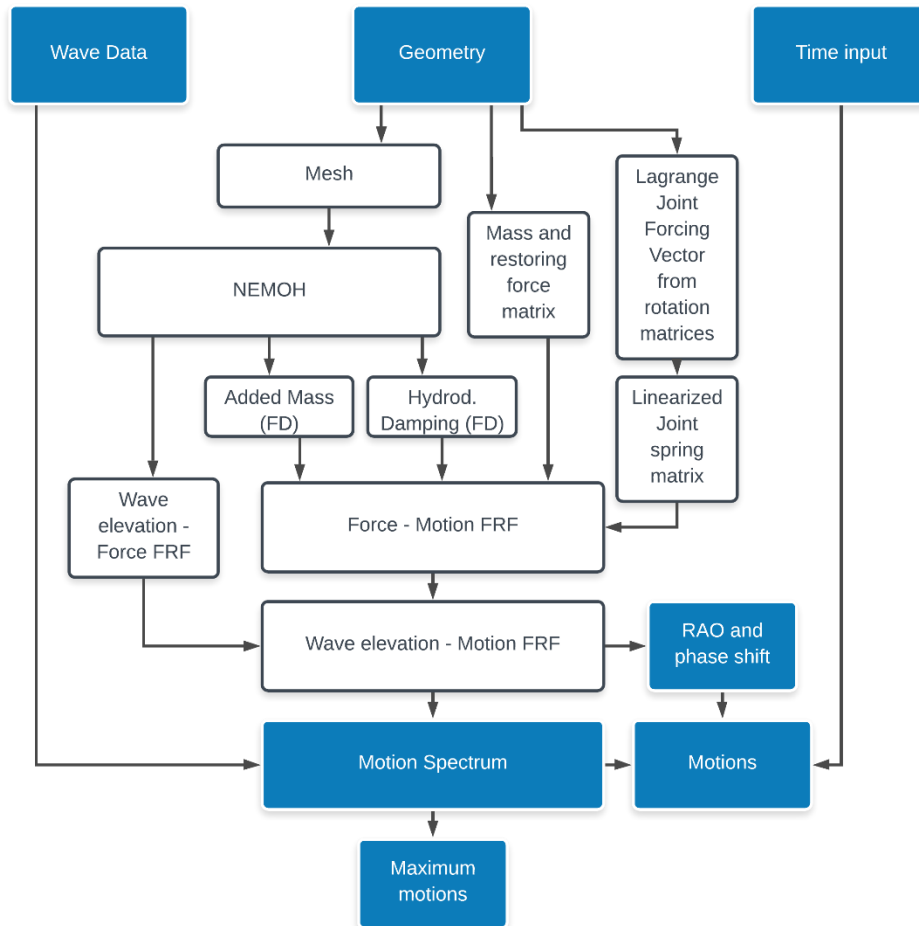
4.2.1 Model overview

Figure 4.6: Flow chart of the calculation procedure of the Frequency Domain model

A frequency domain model based on linear equations of motions can be summarized with the basic overview shown in Figure 4.6. The following inputs are required for the calculation of the motions:

- Wave Environment
- Geometry of the floaters and joints

4.2.2   Transfer functions

By NEMOH the wave-force amplitude frequency response $\left(\frac{F_a}{\zeta_a}\right)$ and the wave-force phase shift $\left(\epsilon_{F\zeta}\right)$ are known and solved in this diffraction software. With these the frequency response function (FRF) from wave motion to forcing in several directions can be composed for the 12 degrees of freedom.

$$H_{F\zeta}(\omega) = \frac{F_a}{\zeta_a}(\omega)e^{i\epsilon_{F\zeta}(\omega)}$$

(Eq. 4.17)

The frequency response function for the force to the displacements can directly be obtained from the equation of motion:

$$H_{uF}(\omega) = \frac{\tilde{u}(\omega)}{\tilde{\tilde{F}}(\omega)} = \left(-\omega^2\big(M + A_H(\omega)\big) + i\omega B_H(\omega) + C\right)^{-1}$$

(Eq. 4.18)

Where $H_{uF}(\omega)$ is a DoF x DoF matrix with frequency response functions.

$$H_{uF}(\omega) = \begin{bmatrix} H_{u_1 F_1} & \cdots & H_{u_1 F_{12}} \\ \vdots & \ddots & \vdots \\ H_{u_{12} F_1} & \cdots & H_{u_{12} F_{12}} \end{bmatrix}$$

(Eq. 4.19)

Since the two frequency response functions are known, the direct FRF from wave elevation to motion can be computed.

$$H_{u\zeta}(\omega) = H_{uF}(\omega)H_{F\zeta}(\omega)$$

(Eq. 4.20)

Similar as equation 4.17 the amplitude and phase shift can be obtained by decomposing the complex frequency response function:

$$\frac{u_a}{\zeta_a}(\omega) = RAO_{u\zeta}(\omega) = |H_{u\zeta}(\omega)|$$

(Eq. 4.21)

$$\epsilon_{u\zeta}(\omega) = \arg\left(H_{u\zeta}(\omega)\right)$$

(Eq. 4.22)

In ship motion terms, there is often referred to the Response Amplitude Operator (RAO) for the amplitude frequency response between motion and wave amplitudes.

4.2.3   Spectral analysis

Knowing the wave to motion function, a motion energy density spectrum can be created with the wave energy density spectrum:

$$S_u(\omega) = |H_{u\zeta}(\omega)|^2 S_\zeta(\omega)$$

(Eq. 4.23)

The moments of area of the spectrum, gives different information about the motion. The nth order moment of area of the spectrum can be calculated in the following manner:

$$m_{nu} = \int_0^\infty \omega^n S_u(\omega)d\omega$$

(Eq. 4.24)

With: $\sigma_u = \sqrt{m_{0\zeta}}$, $T_1 = 2\pi\frac{m_{0\zeta}}{m_{1\zeta}}$, $T_2 = 2\pi\sqrt{\frac{m_{0\zeta}}{m_{2\zeta}}}$

The mean period is: $T_m = T_1$ and the zero upcrossing period: $T_z = T_2$.

4.2.4 Maxima analysis

If the range of frequencies in a wave field is not too large, one speaks of a narrow-banded frequency spectrum. Luckily, waves - a sea or a swell - generally satisfy this condition quite well. If this is the case - and the water surface elevation is a Gaussian distribution - then the wave amplitude statistics will obey a Rayleigh distribution (Journée & Massie, 2001).

The probability density function of the Rayleigh distribution for a given amplitude u_a is:

$$f(u_a) = \frac{u_a}{\sigma_u^2} \exp\left(-\left(\frac{u_a}{\sigma_u \sqrt{2}}\right)^2\right) = \frac{x_a}{m_{0u}} \exp\left(-\frac{x_a^2}{2m_{0u}}\right) \qquad \text{(Eq. 4.25)}$$

And its cumulative distribution function:

$$F(u_a) = 1 - \exp\left(-\frac{u_a^2}{2m_{0u}}\right) \qquad \text{(Eq. 4.26)}$$

It is more interesting to have an idea what the chance is that a certain motion amplitude is exceeded.

$$P\{u_a > a\} = 1 - F(a) = \exp\left(-\frac{a^2}{2m_{0u}}\right) \qquad \text{(Eq. 4.27)}$$

The maximum motion amplitude can be approximated with the above stated Rayleigh distribution. The spectrum S_u derived from the equation of motion and a wave spectrum input, represents a 3-hour storm condition, where with the spectral area moments the zeros-upcrossing period, T_z has been determined. The average number of cycles in these three hours is therefor:

$$N = 3 * \frac{3600}{T_z} \qquad \text{(Eq. 4.28)}$$

Since the maximum amplitude should only occur once in these three hours, the chance that this happens is equal to $1/N$. Rewriting equation 4.27 and 4.28 will give the following equation for the maximum motion amplitude where this is the case:

$$u_{max} = \sqrt{-2m_{0u} \ln\left(\frac{1}{N}\right)} \qquad \text{(Eq. 4.29)}$$

4.2.5 Conclusion

The linear frequency domain equation of motion can be rewritten into a set of transfer functions between forcing and motion. A multiplication with the wave to force transfer function gives the immediate complex transfer function between wave elevation and motion.

From a wave spectrum, the motion spectrum can be obtained. For narrow banded spectra the maxima are Rayleigh distributed and with spectral analysis occurring maxima can be determined rapidly.

5. Gap Resonance

Since the prior performed calculations assume a constant draft of the floater in the water, the part of the floater above the water is not further specified, and therefore it is seen as infinitely high. A common problem encountered in applying potential theory in offshore applications is gap resonance. Since no breaking of waves is taken into account or overtopping of water over the floaters, this contributes to unrealistic calculations of wave elevations in the gap (Dinoi, 2016).

5.1   Gap resonant frequencies

In order to estimate gap resonances of rectangular barges, (Molin, 2009) presented a paper based on earlier studies about piston and sloshing modes in moonpools. By assuming the moonpool as a narrow gap without ends the following approximation could be derived:

$$\omega_n^2 \simeq g\lambda_n \frac{1 + J_n \tanh(\lambda_n h)}{J_n + \tanh(\lambda_n h)} \qquad \text{(Eq. 5.1)}$$

Where:

$$J_n(r) = \frac{2}{n\pi^2 r}\left\{\int_0^1 \frac{r^2}{u^2\sqrt{u^2 + r^2}}\left[1 + 2u + (u-1)\cos(n\pi u) - \frac{3}{n\pi}\sin(n\pi u)\right] du \;-\; \frac{1}{\sin(\theta_0)} + 1 \right.$$

$$\left. + 2r\ln\left(\frac{1 + \cos(\theta_0)}{1 - \cos(\theta_0)}\right)\right\}$$

With $\lambda_n = \frac{n\pi}{l}, r = \frac{b}{l}, \tan(\theta_0) = r^{-1}$

- ω Natural frequency
- n Mode
- l Length of gap
- b Width of gap
- h Draft

For different gap widths the resonant frequency can be studied, see Table 5.1. It is visible that for a wider gap (0.6 instead of 0.3m) the resonant frequencies decrease and are getting more in the range of the occurring wave frequencies.

Table 5.1: Resonant frequencies for different gap width between the floaters

Gap width [m]	Natural frequency ω_n [rad/s]				
	ω_1	ω_2	ω_3	ω_4	ω_5
0.3 m	3.82	4.17	4.41	4.62	4.81
0.6 m	3.14	3.56	3.86	4.12	4.36

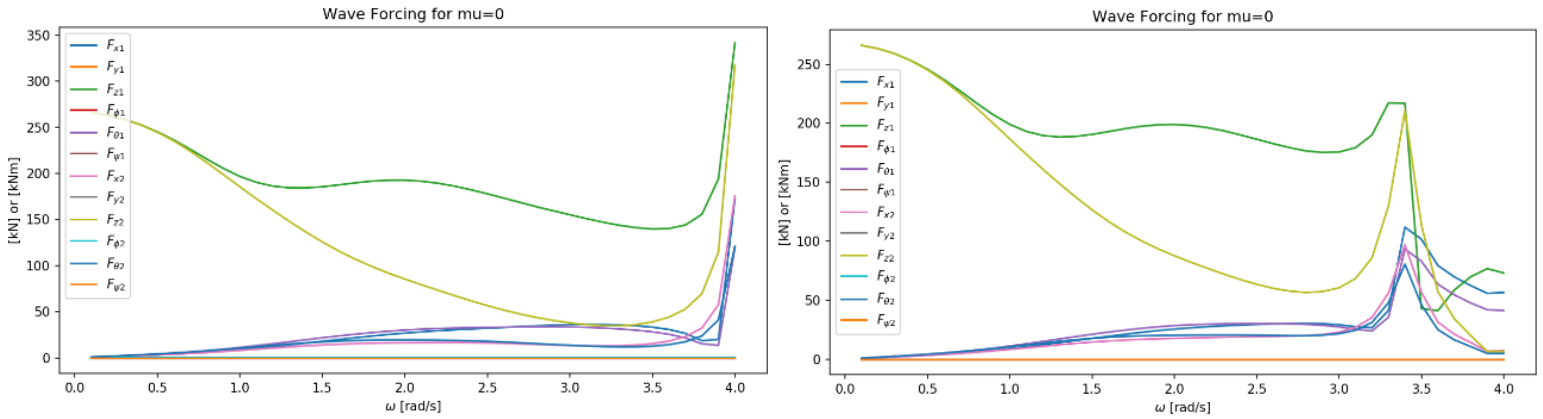This gap resonance is clearly visible in the hyd-files, see Figure 5.1.

Figure 5.1: Wave forcing amplitude response from hyd-file for two floaters with different gap width: 0.3m (left) and 0.6m (right). With $\mu = 0°$ wave heading.

In Figure 5.1 clearly the first resonant frequency can be recognized in the wave forcing. Nevertheless, it is not exactly the estimated value as described by Molins equation, (Molin, 2009) describes that in the studied case of rectangular barges, the first resonant frequency is underestimated by the equation.
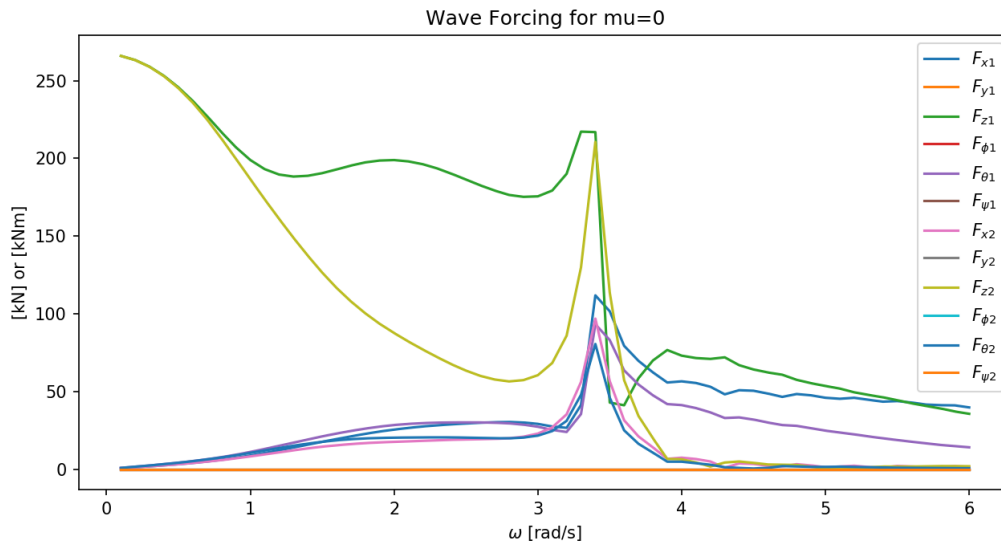

Figure 5.2: Wave forcing amplitude response from hyd-file for two floaters with 0.6m gap. With $\mu = 0°$ wave heading.

5.2   Gap resonance suppression

Different ways of gap resonance suppression have been developed (Bunnik, Pauw, & Voogt, 2009):

- Placing a rigid lid on the free surface of the gap. (Huijsmans, Pinkster, & Wilde, 2001)
- Damping of wave modes. (Newman, 2003)
- A damping lid method, where a certain damping factor is applied to the wave elevation in the gap. (Fournier, Naciri, & Chen, 2006)

None of these methods has been included in NEMOH for the suppression of the gap resonance.

Nevertheless, (Pena & McDougall, 2016) states that it is not of a very big issue for small gaps. The following observations were made by applying different suppression methods:

- The more damped the system, the added mass tends to decrease when positive and increase when negative.
- An abrupt change in sign is seen at the gap resonant frequencies for several hydrodynamic coefficients.
- Increasing the distance seems to increasingly affect the damping coefficient assigned to the flexible lid. The system becomes sensitive to that coefficient at big gap distances.
- The system seems to be overdamped for a damping factor of 1 and 0.3 for big gap distances.
- The added mass of the ship takes values bigger than the real mass of the vessel.
- It can be concluded that the addition of lids is necessary when the gap distance takes significant values.

Meaning that especially the changing shape of the hydrodynamic coefficients is of great influence for larger gaps.

In order to overcome any influences of gap resonance In this research the location of the gap resonance in the hydro-dynamic coefficients is traced and around this point, cut out and linearly interpolated. Sharp edges are smoothened, see Figure 5.3 as example for the linear interpolation and smoothening of the hydro-dynamic coefficients.
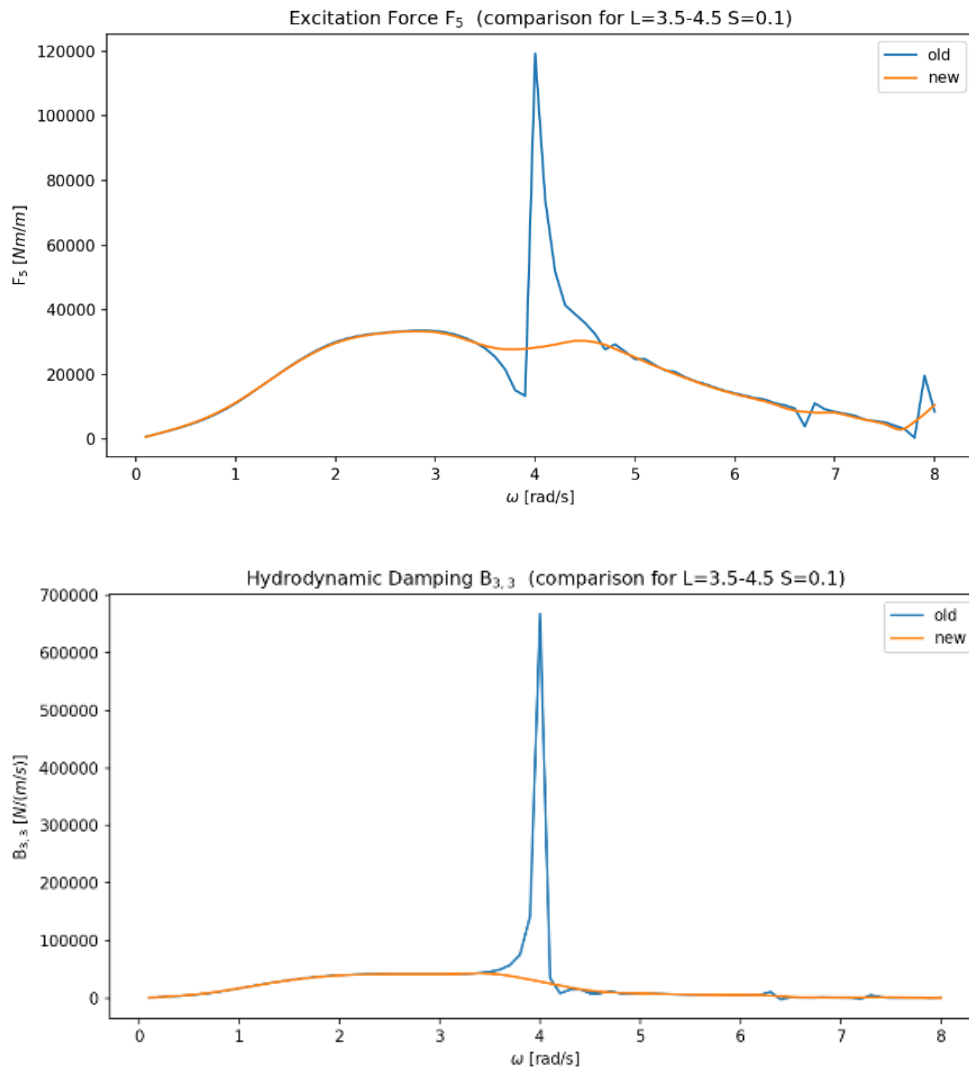
Figure 5.3: Gap resonant peak shown for forcing in pitch direction (left) and the hydrodynamic damping in heave. The suppression method is shown in orange.

Since the gap is not very large, the change will be of minor influence on the total system. Suppressing the resonance peaks is acceptable for the analyzed system, since the freeboard and draft are very small and resonance of the waves in between the floaters is most likely not able to develop into modes of resonance (standing waves). There is more elaborated on the gap resonance interpolation in Appendix K.

On the other hand, the gap resonance peaks have a large influence on the retardation time. As described in section 4.1.4 the retardation function is a decaying function calculated from an integral of the damping coefficient in frequency domain. With a not suppressed gap resonance peak the retardation function will have fluctuation with a larger amplitude and therefor it takes a longer time before the retardation function has decayed to zero (see Figure 5.4).
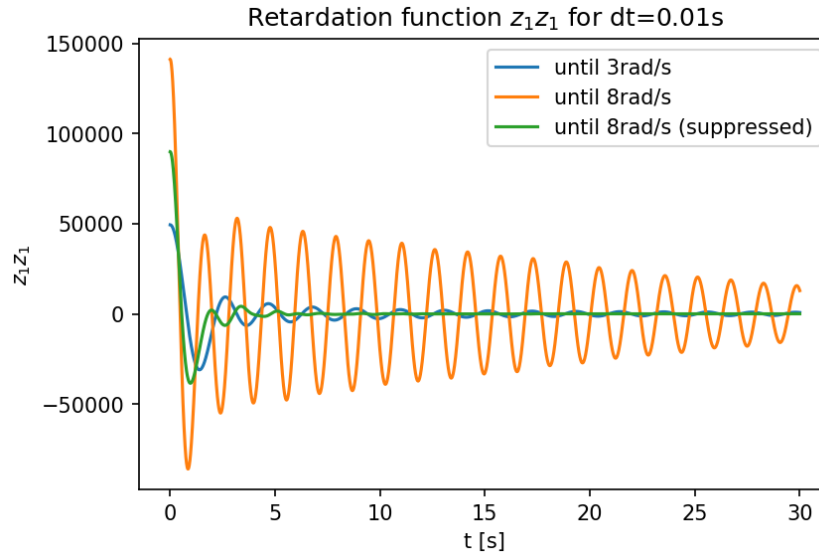
Figure 5.4: heave retardation function for unchanged, cut-off and suppressed hydrodynamic damping coefficient at resonant frequency

To capture the right behavior of the floater the convolution of the retardation function with the velocity needs to be evaluated for more time steps every time step. Stopping the retardation function to early tends the error to increase and the time domain solver to become unstable. It literally resonates then, but for another reason in this case.

5.3   Conclusion

Gap resonance in the hydrodynamic coefficients is clearly visible for floating objects next to each other. This is a result of the assumption in BEM-solvers that the floaters are infinitely high above the water line and the water in the gap 'can go nowhere'. Molin described an approach to identify these gap resonant frequencies based on moonpool calculations, without a piston mode.

The influence on the model is not very large but visible. It has an effect on the overall calculation time, since the retardation function needs to be evaluated for a longer period in time and with that the velocity back in time.

Several techniques exist to suppress gap resonance in BEM-solvers, nevertheless in NEMOH these are not incorporated, therefor the hydrodynamic coefficients at the first gap resonant frequency are cut out and linearly interpolated in that range. A smoothening of 10% is applied to take out the sharp edged of the coefficients.

6. Comparing Time and Frequency domain

Two different approaches have been presented in solving the motions of two interconnected floaters: A time domain and a frequency domain approach. In order to determine if both are stated correctly, a transform from one domain to the other is applied. Nevertheless, the frequency domain approach can only be used for linear calculations and therefor only a comparison with a linear time domain model would give a good comparison.

The linearized joint forcing from equation 2.40 is used in the time domain model, as is the linear joint matrix from equation 2.41 in the frequency domain.

The results of both models could ether be compared in frequency domain or in time domain, with the following procedures:

- Fourier Transform of time domain signal
- Inverse Fourier Transform of frequency domain signal
- Superposition principle of frequency domain signal

6.1 Comparison in frequency domain

In order to verify both systems, a comparison is made between the time domain and frequency domain model in the frequency domain. A spectrum from a time trace can be composed with a Fourier Transform.

The Forward Fourier Transform is denoted as $\mathcal{F}$, and is:

$$\tilde{U}(\omega) = \mathcal{F}\big(u(t)\big) = \int_{-\infty}^{\infty} u(t)e^{-i\omega t}dt$$

(Eq. 6.1)

For finite time signals there exists a Discrete Fourier Transform (DFT). This breaks up a periodic digital signal into a finite number of digital sinusoids (Brandt, 2011).

$$\tilde{U}_k = \sum_{k=0}^{N-1} u_n e^{-i2\pi nk/N} \ , \ \ for \ k = 0,1,\dots,N-1$$

(Eq. 6.2)

The single sided frequency domain signal is then the multiplication with its complex conjugate:

$$\tilde{U}_{single}(k) = \tilde{U}_k \tilde{U}_k^*$$

In Python the computation can be performed by a system that consists of several algorithms called the Fast Fourier Transform (FFT). This calculates the result to equation 6.2 in a faster way.

There exist some differences between the DFT and the continuous Fourier Transform as shown in equation 6.2. Important differences were described by (Brandt, 2011):

- The DFT is computed from a finite number of samples, whereas the analog Fourier transform is an integral from minus infinity to infinity.
- The DFT is not scaled in the same units as the analog Fourier transform, since the differentiator dt is missing. The analog Fourier transform of a signal with units of m/s2 would have units of m/s, whereas the DFT will have units of m/s2.
- The DFT is calculated in a non-symmetrical way, from n = 0 to n = N−1, and not symmetrically as the analog Fourier transform.

The FFT results in a two-sided spectrum of the time trace in frequency domain. The motion energy density spectrum can be obtained from this (Stewart, 2000).

$$S_{u,k} = \frac{1}{2\Delta\omega} \left| 2\tilde{U}_k \right|^2, \quad (k = 1, 2, \dots, (N/2 - 1))$$

(Eq. 6.4)

Where: $\Delta\omega = 2\pi/T_{meas}$.

The result for two interconnected floaters under beam waves ($\mu = 0°$) in heave and pitch motion are shown in Figure 6.1. It can be observed that the pitch gives slightly different results for higher frequencies.
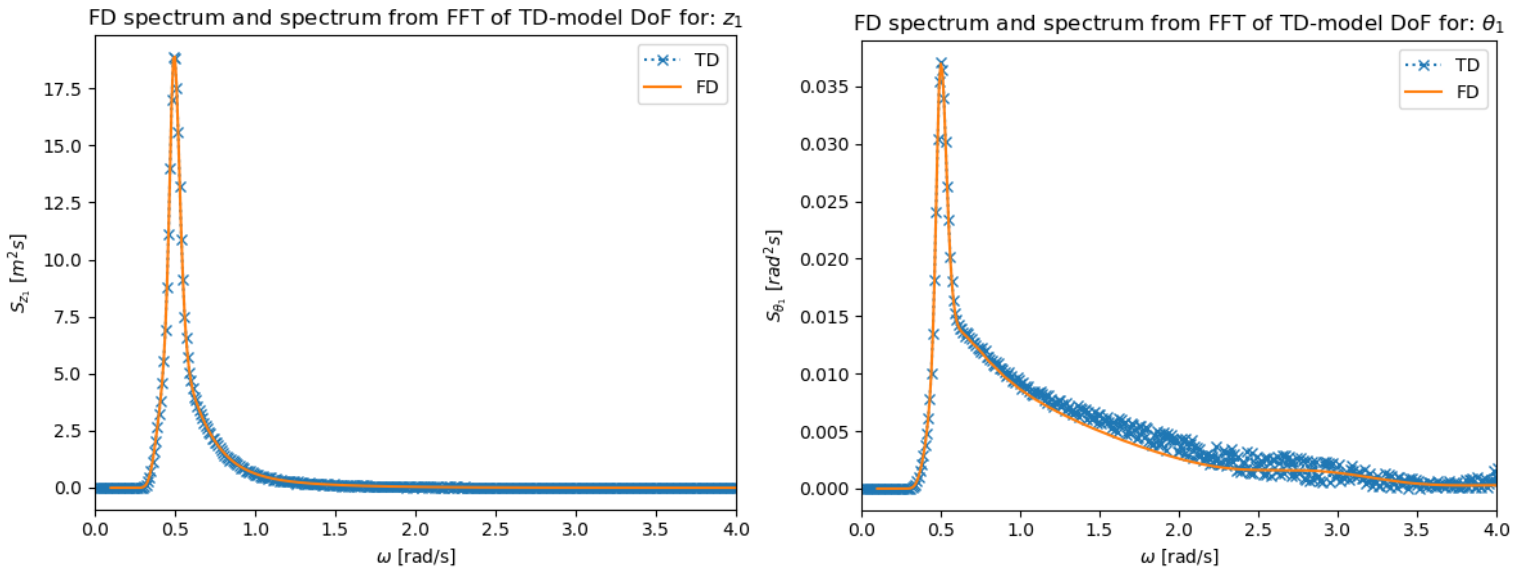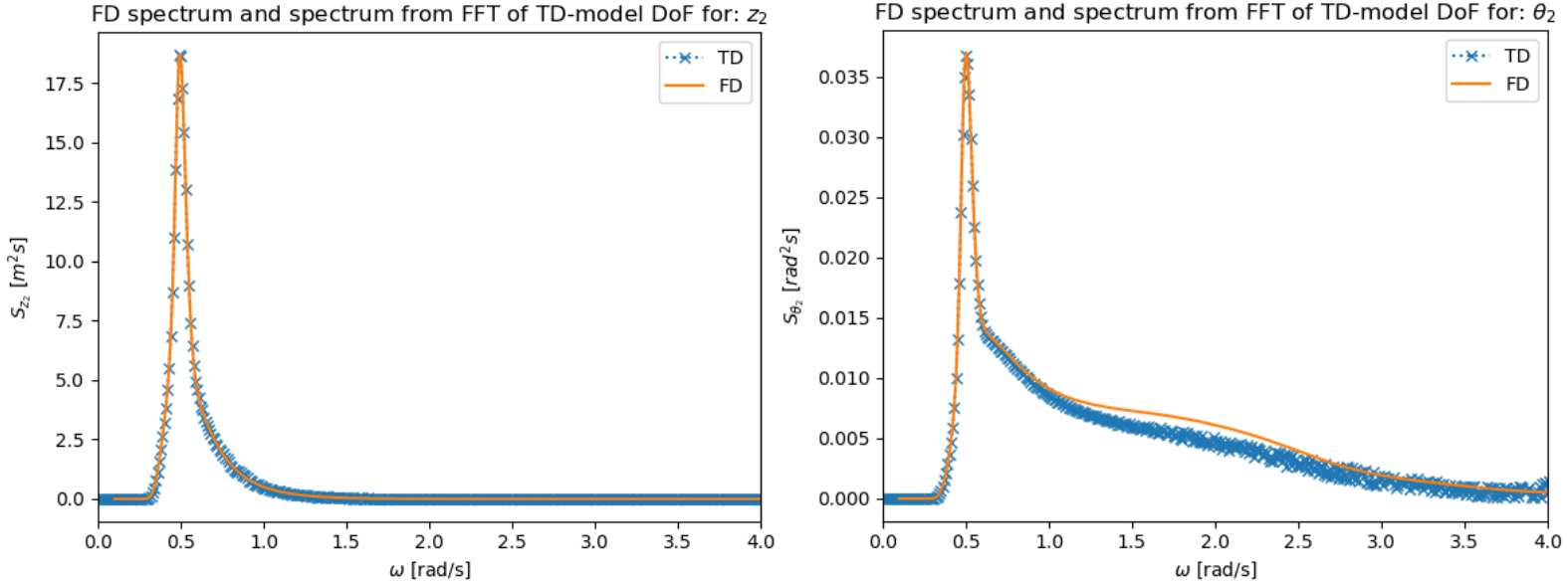
Figure 6.1: motion energy density spectra for 4DoF's in ULS waves, derived from the frequency- and linear time-domain model

6.2 Comparison in time domain

As can be seen in the comparison in frequency domain, they are only based on occurring amplitudes (energy density spectra) and not on phase shifts. On top of that a direct numerical comparison is more preferred. This is possible in time domain, in two ways. Namely by means of the inverse Fourier Transform or the superposition principle.

6.2.1 Inverse Fourier Transform

The Inverse Fourier Transform is denoted as $\mathcal{F}^{-1}$, and is therefore:

$$u(t) = \mathcal{F}^{-1}\left(\widetilde{U}(\omega)\right) = \frac{1}{2\pi}\int_{-\infty}^{\infty}\widetilde{U}(\omega)e^{i\omega t}d\omega \qquad \textit{(Eq. 6.5)}$$

For a discrete finite frequency signal the Discrete Inverse Fourier Transform (DIFT) can be applied on a spectrum (Brandt, 2011):

$$u(n) = \frac{1}{N}\sum_{k=0}^{N-1}\widetilde{U}(k)e^{i2\pi nk/N} \ , \ \ for \ n = 0,1,\dots,N-1 \qquad \textit{(Eq. 6.6)}$$

A build in algorithm in programming languages called the Inverse Fast Fourier Transform (IFFT) has a fast way of performing the calculation in equation 6.6.

There are several things that need to be addressed to perform a successful Inverse Fourier Transform of the frequency domain model to the time domain, being the following:

- Double sided spectrum generation
- Frequency resolution
- Hydrodynamic Coefficient Interpolation Issues
- Discretization

6.2.2 Double-sided spectrum generation

The obtained energy density spectrum in frequency domain is a single sided spectrum. In order to fulfil the requirements of the IFFT a complex double-sided spectrum needs to be composed first from the phase shift spectrum and the energy density spectrum. On top of that a random phase shift was added to the wave spectrum in the Time domain model (equation 4.2) for the force generation. In the same manner the same random phase shift should be added to the frequency domain spectrum.

The single sided amplitude spectrum can be calculated from the motions energy density spectrum:

$$u_a(\omega) = \sqrt{2S_u(\omega)\Delta\omega}$$

(Eq. 6.7)

The complex single sided spectrum can be composed of the combination of the wave-to-motion phase spectrum $\epsilon_{u\zeta}(\omega)$, the random wave-phase spectrum $\epsilon_\zeta(\omega)$ and the amplitude spectrum $u_a(\omega)$.

$$\tilde{u}_s(\omega) = u_a(\omega)e^{\left(\epsilon_{u\zeta}(\omega)+\epsilon_\zeta(\omega)\right)i}$$

(Eq. 6.8)

The double-sided complex frequency domain signal can be obtained by taking the complex conjugate for the negative frequencies.

$$U_D(\omega) = \begin{cases} \overline{\dfrac{1}{2}\tilde{u}_s(\omega)} & for\ \omega < 0 \\ 0 & for\ \omega = 0 \\ \dfrac{1}{2}\tilde{u}_s(\omega) & for\ \omega \geq 0 \end{cases}$$

(Eq. 6.9)

Note: When comparing the spectrum with a time domain signal in time domain via an Inverse Fourier Transform, the added random wave phase shift must be equal at every frequency in both cases. Firstly, for the superposition that is used to obtain the time-signal-forcing and secondly for the composition of the complex frequency domain signal before applying the IFFT.

6.2.3 Frequency resolution

The frequency step size (resolution) is prescribed in Frequency Domain and is 0.01 rad/s, see section 3.3.2.

$$\Delta\omega = 0.01\frac{rad}{s} \rightarrow \Delta f = \frac{\Delta\omega}{2\pi}$$

(Eq. 6.10)

Therefore, the following will apply in the following reference case: $T_{meas} = \frac{1}{f_0} = 628.3s$. Since the spectrum is double sided the number of samples is $N = 2\frac{\omega_{max}}{\Delta\omega}, t_s = \frac{T_{meas}}{N}, f_s = \frac{1}{t_s}$.

This means that the length of the data record and the step size in time domain after the IFFT is prescribed by the data-record in the frequency domain. In vibration analysis there exist several methods to improve this, but there is no need to implement it in this analysis.

6.2.4 Hydrodynamic coefficient interpolation issues

Applying the above method to the frequency domain model output needs some extra attention. The inputs of the model by NEMOH, i.e. forcing and hydrodynamic coefficients, were calculated with a frequency resolution of 0.1 rad/s, [0.1, 8rad/s]. The evaluation of the coefficients at 0 rad/s is not performed in a BEM-solver and is not possible for numerical reasons.

As described in section 3.3.2, the hydrodynamic coefficients were interpolated for a step size of 0.01 rad/s in order to best cover the narrow banded JONSWAP wave spectrum. Meaning that the hydrodynamic coefficients are interpolated between 0.1 and 8 rad/s with a step size of 0.01 rad/s.

In order to perform the IFFT in a proper way the values for 0 up to 0.09 rad/s need to be added manually in the spectrum as zero at all these points. This will give the complete spectrum so that the IFFT can be performed.

6.2.5 Discretization

The frequency signal is a continuous signal derived from the energy density spectrum and in order to perform an IFFT, where discrete sampling is applied, the signal has to be made discrete. This means that the signal is only able to contain information at multiples of the base frequency $\Delta\omega$. Hence, before applying the DFT the signal is multiplied with the number of samples:

$$u(t) = ifft(U_D N)$$
*(Eq. 6.11)*

6.2.6 Superposition

The superposition principle, as described in section 4.1.3, for the calculation of the wave force acting on the floaters in time domain, can also be used for switching from the frequency domain model results of the motion to time domain.

$$u(t) = \sum_{n=1}^{N} \Re\left(u_{a_n} e^{-i\left(\omega_n t - \epsilon_{u\zeta n} - \epsilon_{\zeta n}\right)}\right)$$
(Eq. 6.12)

This method is a more intuitive way for linear systems and allows changing the time step as wanted.

6.2.7 Comparison

Plots of the first 100 seconds of the IFFT of the frequency domain result and the linear time domain result are shown in Figure 6.2.
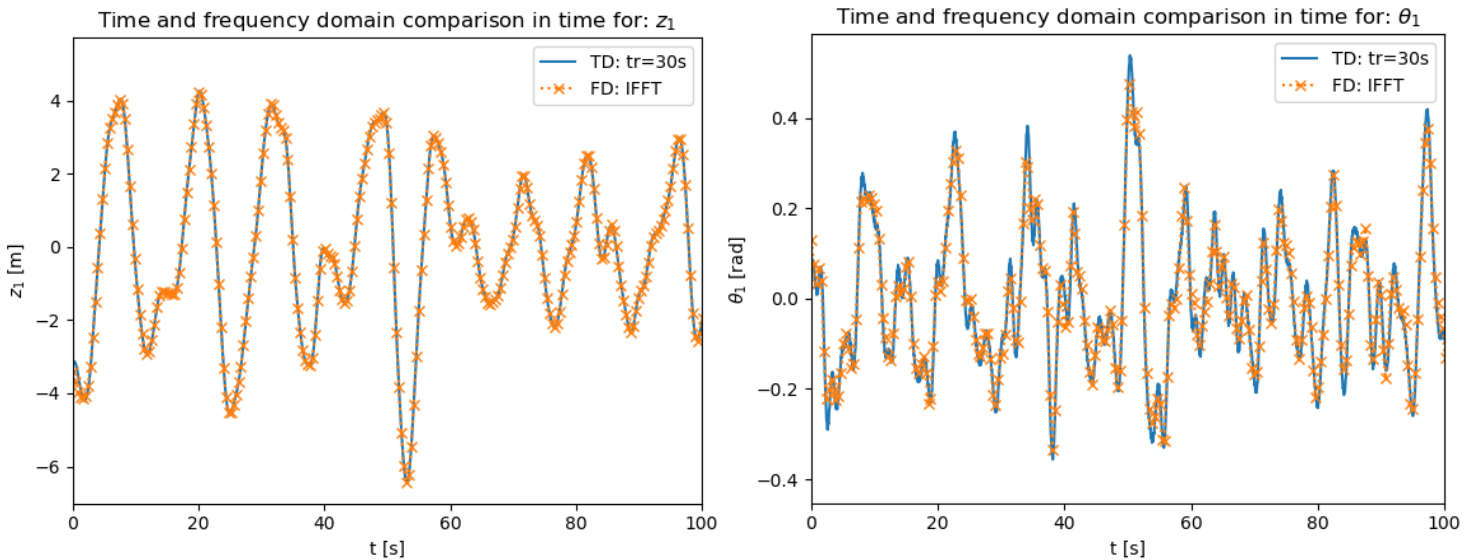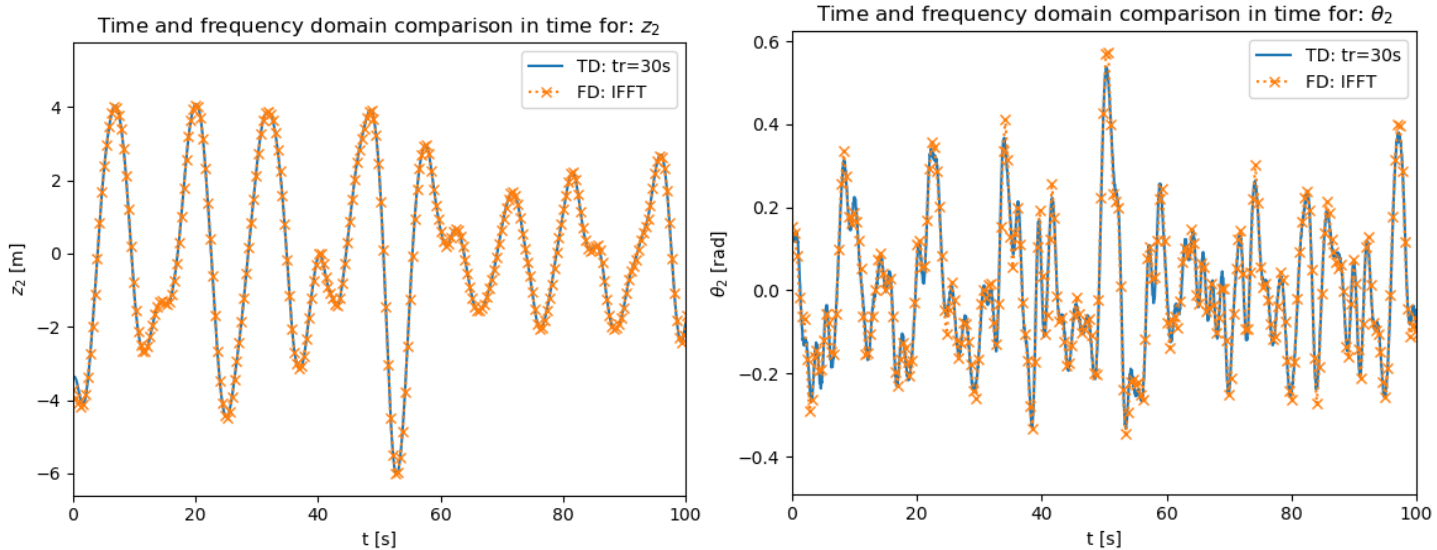
Figure 6.2: first 100 seconds of the IFFT of the frequency domain model and the linear time domain model

Also here a small difference can be observed in the pitch motion. Next to that the first part shows slight differences, since the time domain model, has initial conditions as input and the convolution integral is not 'fully' evaluated for past velocities. Therefor it is more convenient to study the behaviour after some time steps. Figure 6.3 shows the time where the largest difference between the linear time-domain model and the frequency domain model is observed, namely in this case in θ_2.
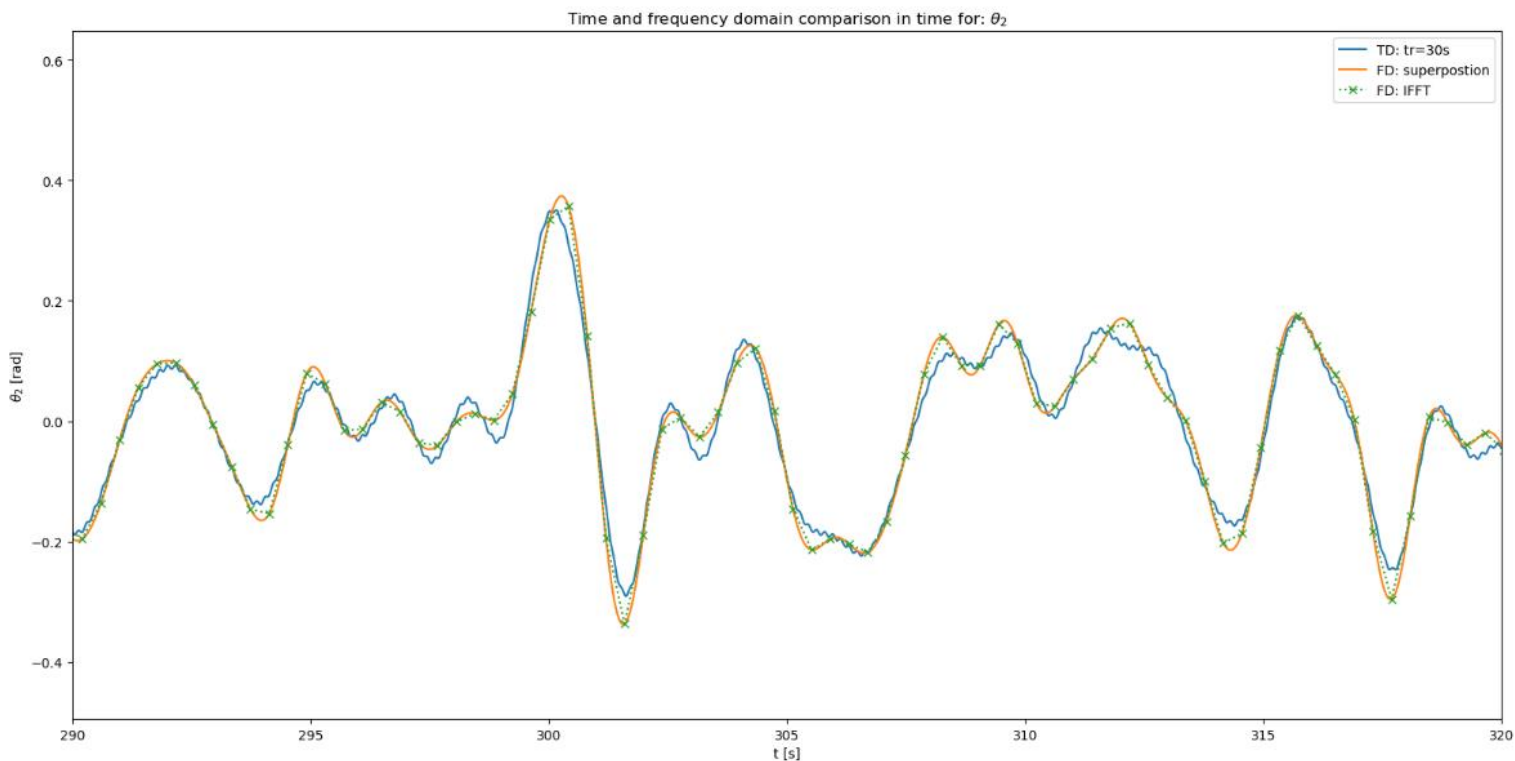

Figure 6.3: Moment in time where the largest difference is found in the response between the time domain and frequency domain model, namely in θ_2.

67

These differences in pitch, are most likely due to the determination of the infinite added mass in the time domain. For a further evaluation of the influence of the infinite added mass see Appendix I.

6.3 Comparing reaction forces and stresses

When the motions in time domain (either from the frequency domain or time domain model) are obtained, the local acting reaction forces at the interconnections can be recomposed and compared in the following manner:

$$\underline{F}_{local} = \underline{\Delta u}_{\text{joint}}\underline{k}^T + \underline{\Delta \dot{u}}_{\text{joint}}\underline{d}^T$$

This will result in non-linear equations for the acting reaction forces. For frequency domain or linear time domain calculations these need to be linearized, to derive the appropriate reaction forces that were acting in the used model.

To get an indication of what this would mean in terms of stresses in a hypothetical joint (see Appendix M), the reaction forces can be combined into stresses. The occurring shear stress (τ) due to torsion ($\tau_{torsion}$) and shear ($\tau_{transversal}$), and the occurring compressive/tensile stress (σ) due to bending ($\sigma_{bending}$) and axial stress (σ_{axial}) can be evaluated at the connection point, when the local reaction forces are known. There is more elaborated on this in Appendix M.

6.4 Conclusion

The frequency model and the linear time domain model can be compared in either frequency domain or time domain. A Fourier Transform gives the opportunity to make an energy density spectrum from the time domain signal, but it is hard to analyze the phase shifts of the response to the incident wave, due to the addition of the random phase shifts. The preferred method to make a comparison is to compare it in time domain. The Inverse Fourier Transform or the superposition principle can be carried out to analyze the result. In the case of an IFT there should be taken care of the appropriate addition of the random wave phase shifts in the frequency domain model before making the transition to time domain.

The results of the frequency and time domain model look very similar in heave but have some small differences in pitch. This is most likely due to the determination of the infinite added mass (see Appendix I).

7. Results

In this section three different case studies are evaluated. Firstly, a comparison is made between the frequency domain model and the linear time domain model. Secondly, the linear and non-linear time domain model is compared. In all the cases firstly the motion and forcing presented for 4 degrees of freedom (heave and pitch of each floater), followed by all degrees of freedom (each floater 6) and different wave directions. At last the convergence to a maximum reaction force in the connection point is presented for different joint stiffness. The obtained results are discussed in each section. In Appendix N the obtained maxima of each model with these inputs is given in table form.

Table 7.1: Inputs in model. n stands for number. Some are intentionally kept blank.

Waves	Significant wave height	H_s	7.0 m
	Peak period	T_p	12.7 s
	Peakedness factor	γ	3.3
	Wave direction	μ	0-90°
Joints	Material		-
	Young's Modulus	E	0.01 GPa
	Outer radius	r_o	294 mm
	thickness	t_j	127 mm
	Poisson's ratio	ν	0.5
DoF	Number of Floaters	$nofl$	2
	Number of DoF's	$nDoF$	12
Time	Time of run	t_{max}	3 hr (10800 s)
	Retardation time	t_r	30 s
	Time step size	Δt	0.05 s
Hydrodynamics	Frequency range	ω	0-8 rad/s
	Frequency step size	$\Delta \omega$	0.01 rad/s
	Added mass	$A(\omega)$	$(12 \times 12 \times n\omega)$
	Hydrodynamic damping	$B(\omega)$	$(12 \times 12 \times n\omega)$
	Wave force amplitude response	$\frac{F_a}{\zeta_a}(\omega)$	$(n\mu \times 12 \times n\omega)$
	Wave force phase shift	$\epsilon_{F\zeta}(\omega)$	$(n\mu \times 12 \times n\omega)$
Geometrics	Length of floater	l	
	Width of floater	b	
	Draft	T	
	Center of Gravity	(x_c, y_c, z_c)	
	Distance to keel	KG	
	Mass	m	
	Gyradii	$[r_x, r_y, r_z]$	
	Inter floater gap	d	

7.1 Case 1: Linear TD vs. FD

As explained in chapter 6, the most appropriate manner to compare the frequency domain with the time domain is by applying the superposition principle to the calculated complex frequency domain motions and compare them in time domain. From the motions in time domain the relative motion between the connection points (ΔP), reaction forces (F_{local}) and local joint stresses (σ, τ) at the connection points can be calculated as presented in Appendix M.

7.1.1 Two floaters under beam waves in heave and pitch

In Figure 7.1, the heave and pitch motions of the floater under beam waves are shown after a certain time (when the effect of initial conditions has vanished). It can clearly be seen that especially in pitching motion they do not coincide exactly. The reason for this can be given to the fact that the determination of the hydrodynamic coefficients $(a_{ij,\infty}, R_{ij})$ in time domain is causing slightly different results than the coefficients (a_{ij}, b_{ij}) in frequency domain. The effect of a change in these coefficients can have a major impact on the behaviour. In Appendix I the effect of change in added mass in time domain is shown.
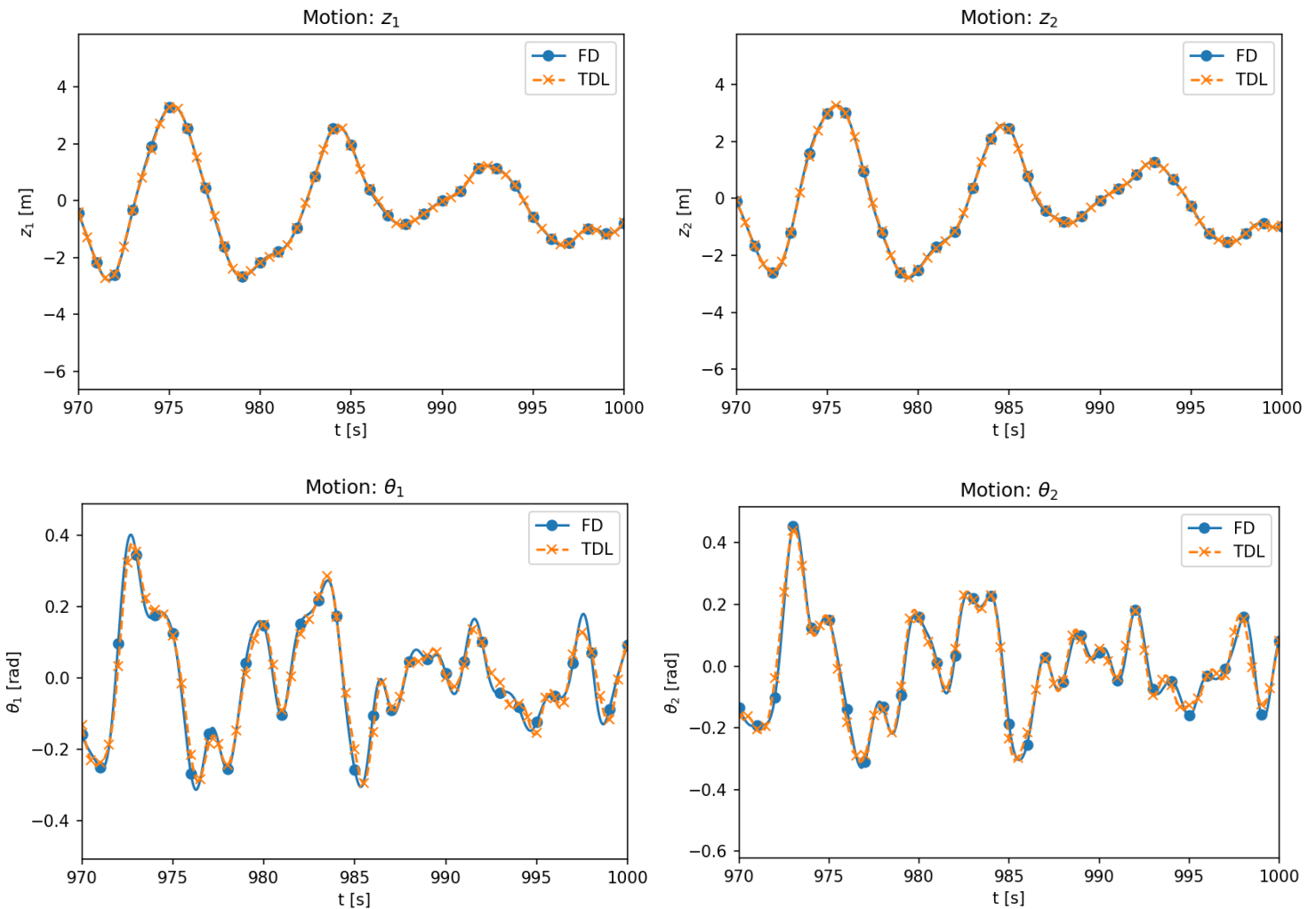

Figure 7.1 Heave and pitch motion of both floaters under beam waves with calculations in linear time domain (TDL) and frequency domain (FD)

Especially in pitch the motions of the interconnected floating bodies, do not match exactly. The difference in results is not that large but can be of significance for further evaluation. Plotting the pitch motions of both floaters together results in the figure shown in Figure 7.2 (left). Although the FD and TDL look similar, the relative pitch motion ($\Delta\theta = \theta_1 - \theta_2$) between both floaters looks very different (see Figure 7.2 (right)). The relative pitch in the connection between both floaters, determines the reaction moment (F_θ) at the connection point (also in pitch direction). The relative motion in pitch is especially high when the gradient of the motion is high (around 972 seconds in this case), i.e. from positive to negative pitch.
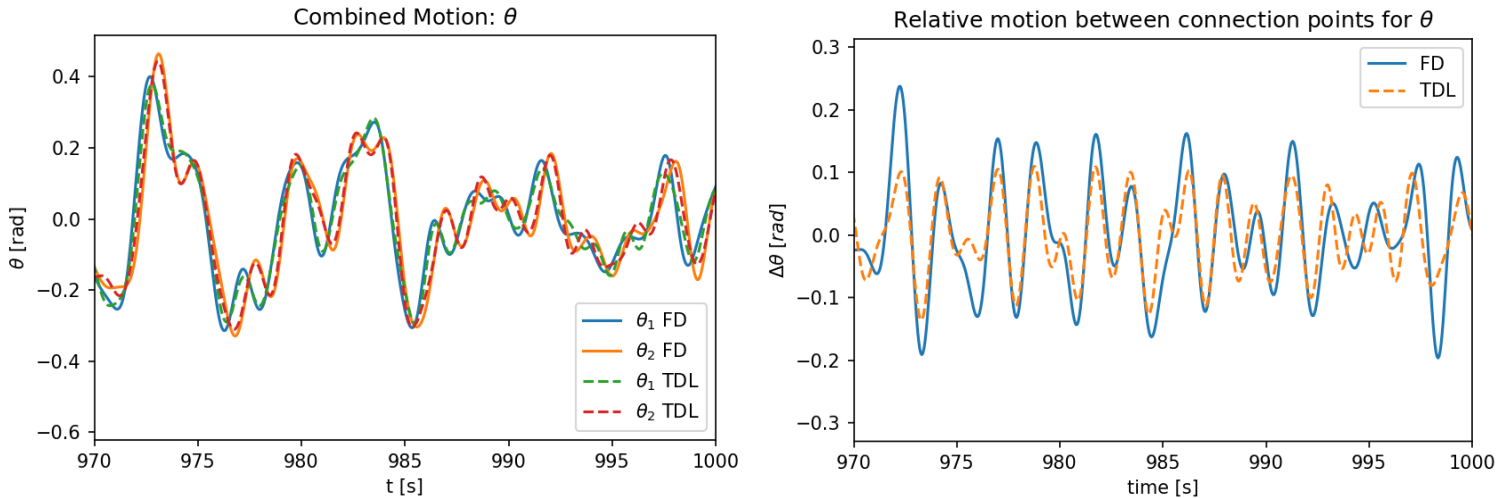
Figure 7.2: Left: Motion in pitch of both floaters for the frequency domain model (FD) and linear time domain model (TDL), Right: Relative motion in pitch between both floaters in FD and TDL.

This minor difference in the motion causes that the reaction forces in the FD-model can become twice as high as in the TDL-model. See Figure 7.3, where the reaction force is given at the point P11 in time and as a boxplot of a 3-hour storm.
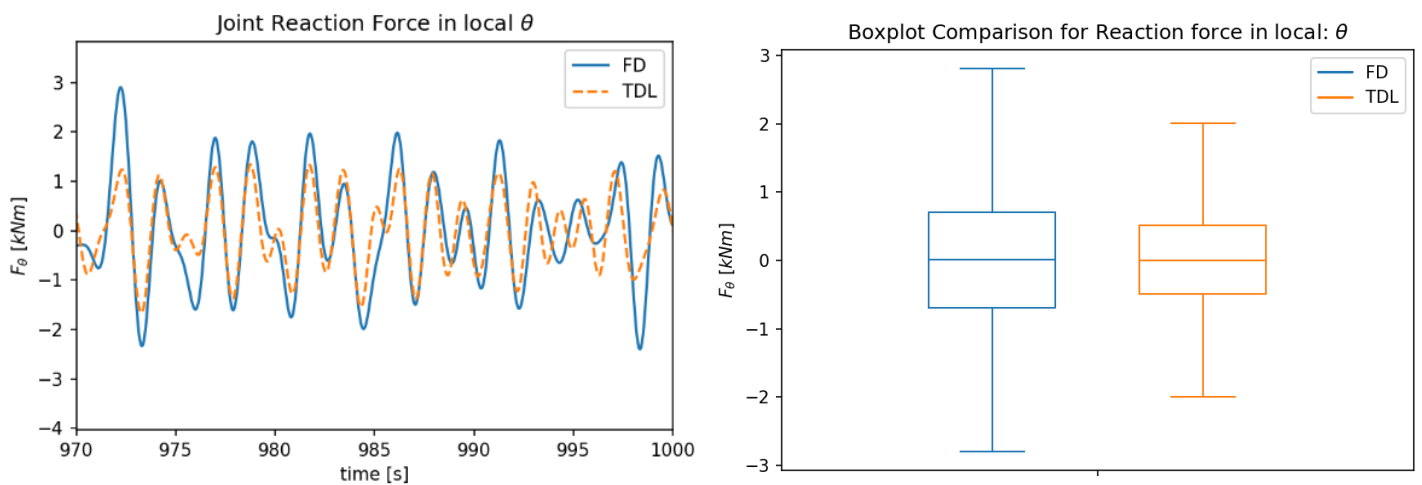

Figure 7.3: Left: Reaction moment at connection point on floater for two floaters in heave and pitch in beam waves. Right: Boxplot of the occurring reaction moments in pitch direction for two floaters in heave and pitch in beam waves.

7.1.2　Two floaters in heave and pitch under various wave directions

As mentioned, under beam waves, a certain difference can be observed in the reaction moment in pitch direction, due to minor differences in the calculation of the motions of the interconnected bodies. In Figure 7.4 the heave and pitch motion of the first floater are shown for varying wave directions. The result of the second floater look similar and are therefore not shown. The reaction force at the connection point resulting from these motions can be found in Figure 7.5. For small wave directions the reaction moment for θ-direction is higher for the FD-model due to the reason described in section 7.1.1. The reaction force in z-direction decreases when going from beam to head waves. In head waves the excitation force in heave direction on the two floaters will be in phase and have the same magnitude. Causing no relative displacement in z-direction between the connection points. However, a relative displacement between the connection points in z-direction can also be caused by pitching of the floaters (see equation 2.34). It can be seen in Figure 7.4 that higher pitching motions are observed in the TDL-model for head waves ($\mu = 90°$).

In Figure 7.7 the motions in pitch and the relative pitch between the floaters are presented, to study this effect. The floaters experience no wave excitation forcing in pitch under head waves, but the motion is caused through a relation with the heave motion. Since the heave excitation force on both floaters is equal in this case, this is a relation rather caused by wave radiation than reaction forces in the connecting joints, i.e. caused by the cross related hydrodynamic damping and added mass terms. In the left plot of Figure 7.7 the floaters will pitch in anti-phase due to this effect. Meaning that the relative motion between the connection points in z-direction and therewith the vertical forcing by this will be very close to zero, but the reaction moments will be higher due to this effect (Figure 7.7 right), although the pitching angles at the center of gravity will be very small (Figure 7.7 left). It can clearly be seen that the pitching angles in the TDL are larger than the ones in FD causing the reaction moments to be higher. This effect on the reaction moment at the connection point in pitch direction to be higher in the TD-case than the FD-case can be observed in Figure 7.5 for higher wave directions ($\mu > 45°$).
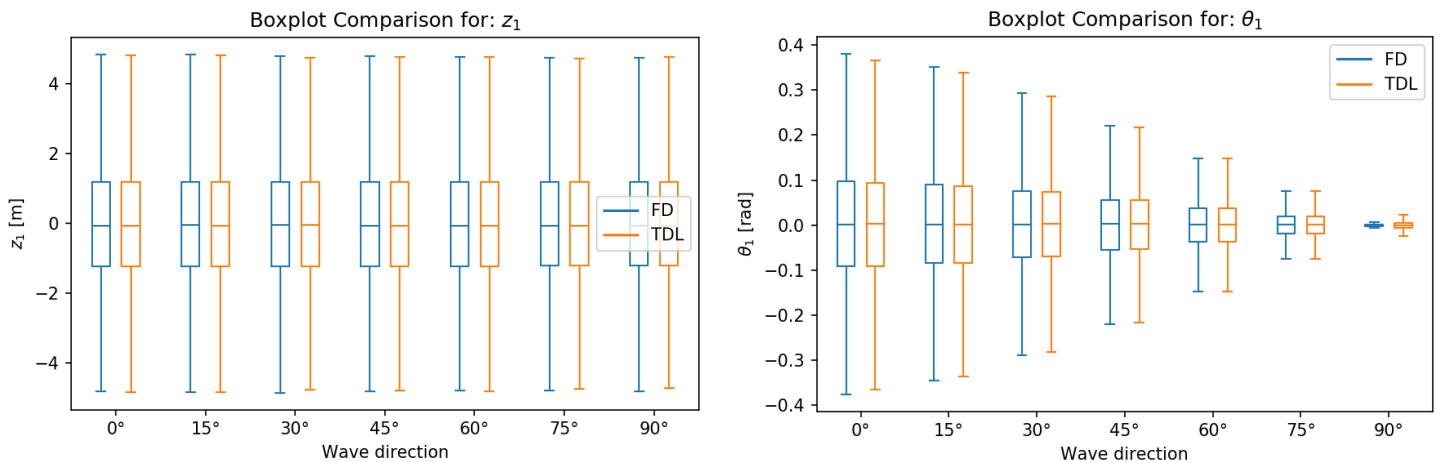

Figure 7.4: Boxplot of motion in heave and pitch for FD and TDL for different wave directions.
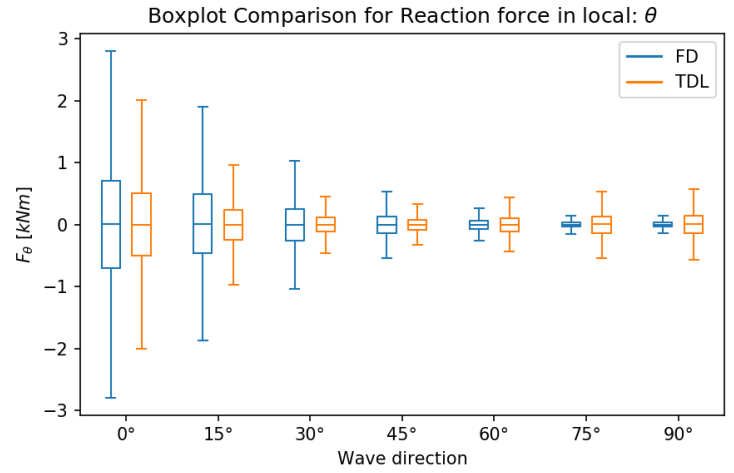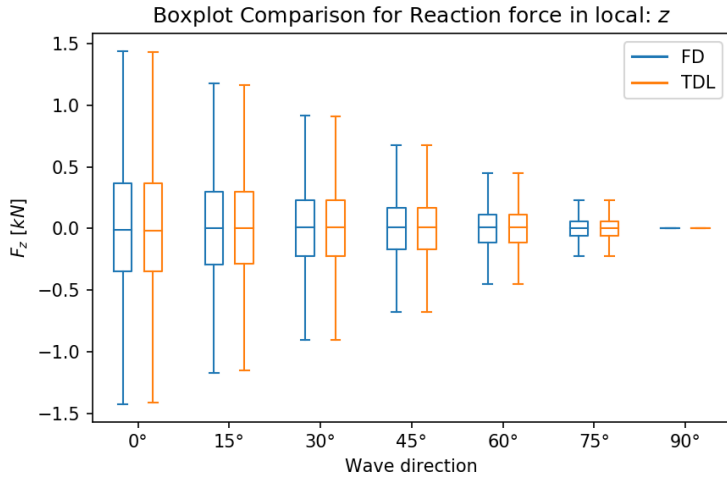
Figure 7.5: Boxplot of reaction force at floaters interconnector point in local z and θ for FD and TDL for different wave directions.
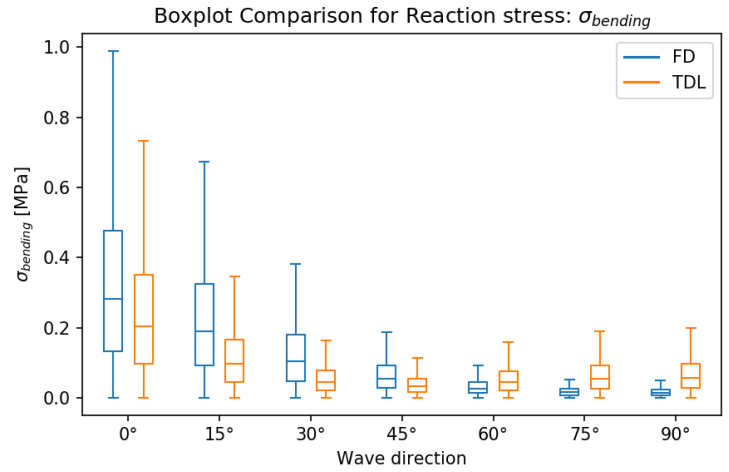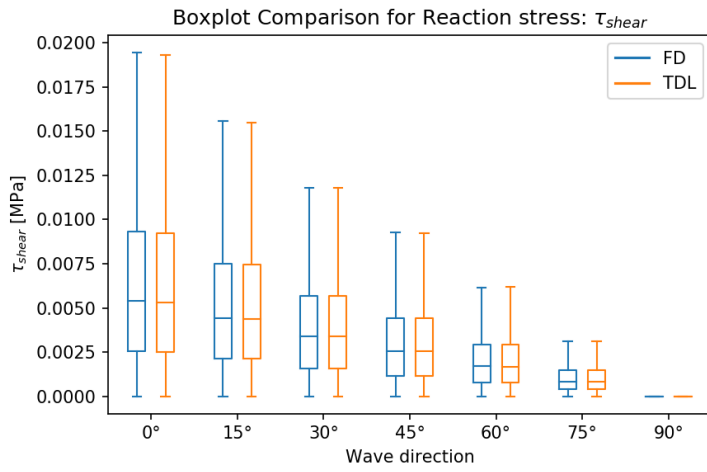

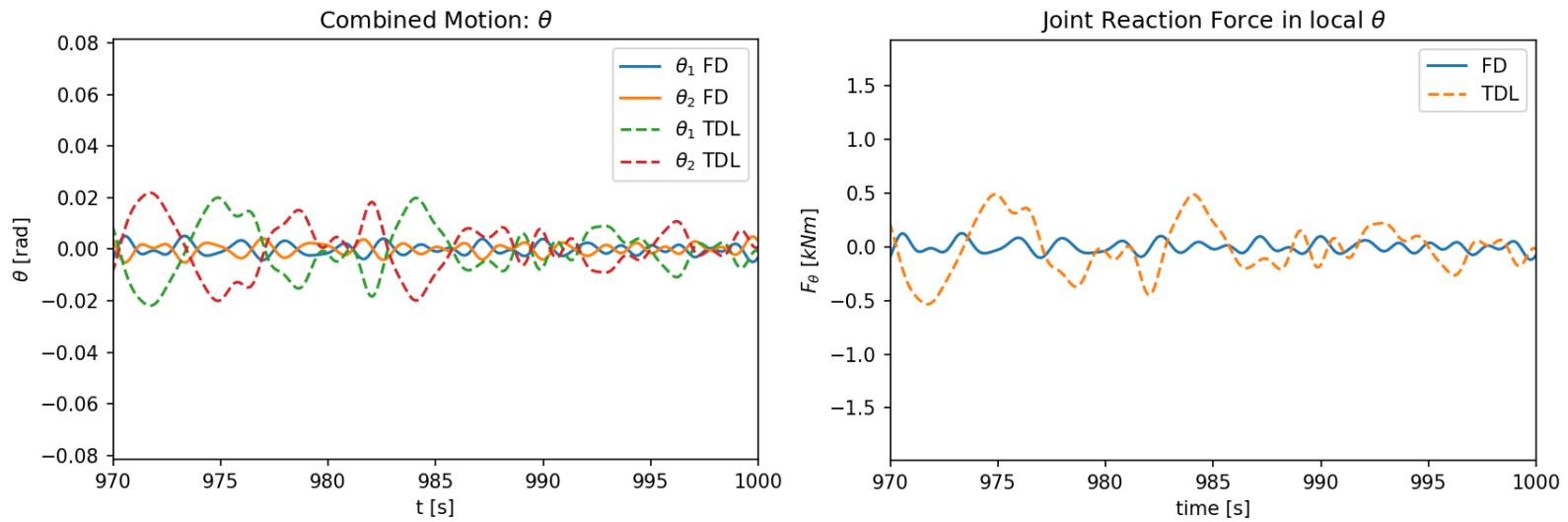*Figure 7.6: Absolute reaction stress at interconnector point in joint.*

Figure 7.7: Left: Motion in pitch of both floaters for FD and TDL for two floaters in heave and pitch in head waves, Right: Reaction force at point P1 for FD and TD for two floaters in heave and pitch in head waves.

7.1.3   Two floaters in 12DoF under various wave directions

In this case the calculation for all degrees of freedom are switched on in both models. Increasing the amount of degrees of freedom, the following should be considered:

- The calculation time of the time domain model will rapidly increase.
- Not all initial conditions can be calculated with the static displacement (see section 4.1.11), since surge, sway and yaw experience no hydrostatic counter reaction force (no mooring was included). Therefor trivial initial conditions are chosen for these degrees of freedom. This will cause that the model needs some time to settle and find a stable position. Since only first order wave forces are considered, the stable position should be reached.
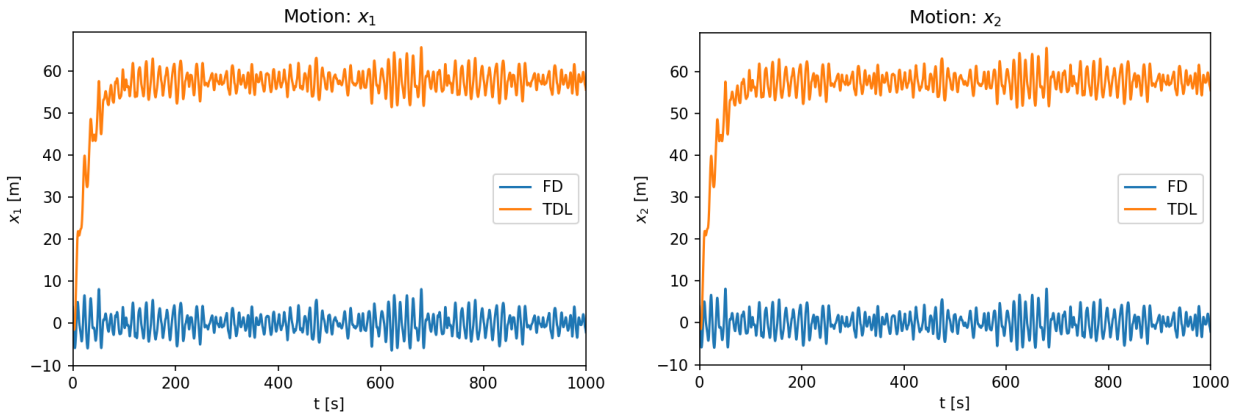

Figure 7.8: Motion of floater 1 and 2 in surge direction and finding a stable position after time

Especially in the modes that experience no hydrostatic forcing the stabilizing of the motion is clearly visible. Even with an offset of tens of meters for surge and sway direction. This effect is caused by the fact that the system is not moored and has no restoring force. There is no need for this either in this model, since the influence of the connections is studied. As described in section 2.4.4 the

74

implementation of the forcing by the connections is relative to the floaters CoG's. In Figure 7.8 the floaters seem to "drift away", but they drift away together, meaning that relatively to each other the appropriate inter floater motions keep intact. When studying the motions, the time record is taken sufficiently long for the floaters to find their 'stable position' and the first part is cut off before subtracting the average (this should be zero under linear first order wave forces) from the result and compare it with the frequency model.

In Figure 7.9 the boxplots are shown of the motions that are found for the first floaters for various wave directions (the second floater gives similar results). Followed by the reaction force at the connection point in Figure 7.10. Reaction force in z, can either be caused by difference in z-motion between both floaters, but also by difference in ϕ and θ. It can be seen that the plot of the forcing in z-direction at the connection point (upper right plot of Figure 7.10) is in shape a combination of these three motions in Figure 7.9. The forces in x-direction at the connection point are large and show different results for both models, this can be assigned to the relatively high axial stiffness of the joints. In Figure 7.11 the relative x-displacement between both floaters is given and is very small, but with a high axial stiffness of the joints the forces still become high. Meaning that minor differences in the calculations between both models can have high impact on this result. The major differences between the models are the added mass and hydrodynamic damping, which should be studied carefully in a follow up study.
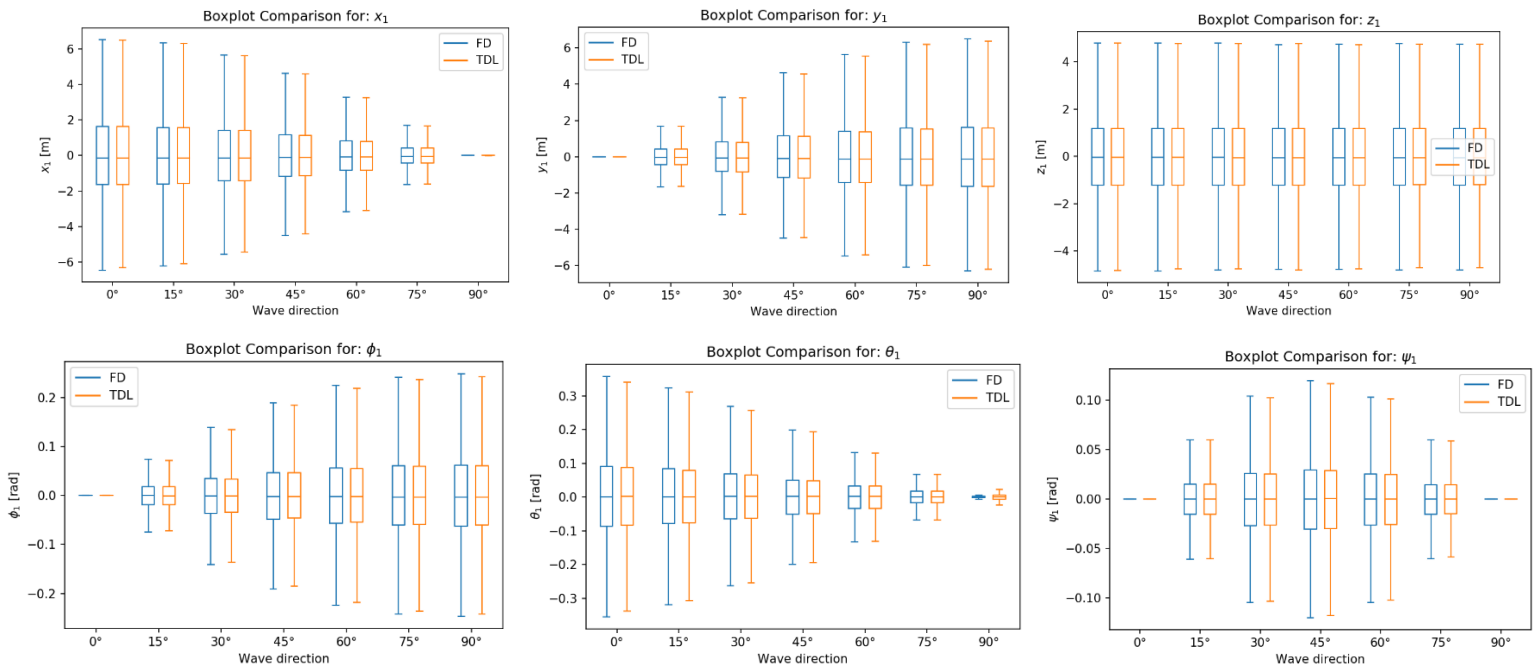

Figure 7.9: Boxplot comparison of motions in TDL and FD in a two interconnected floater model subject to various wave directions.
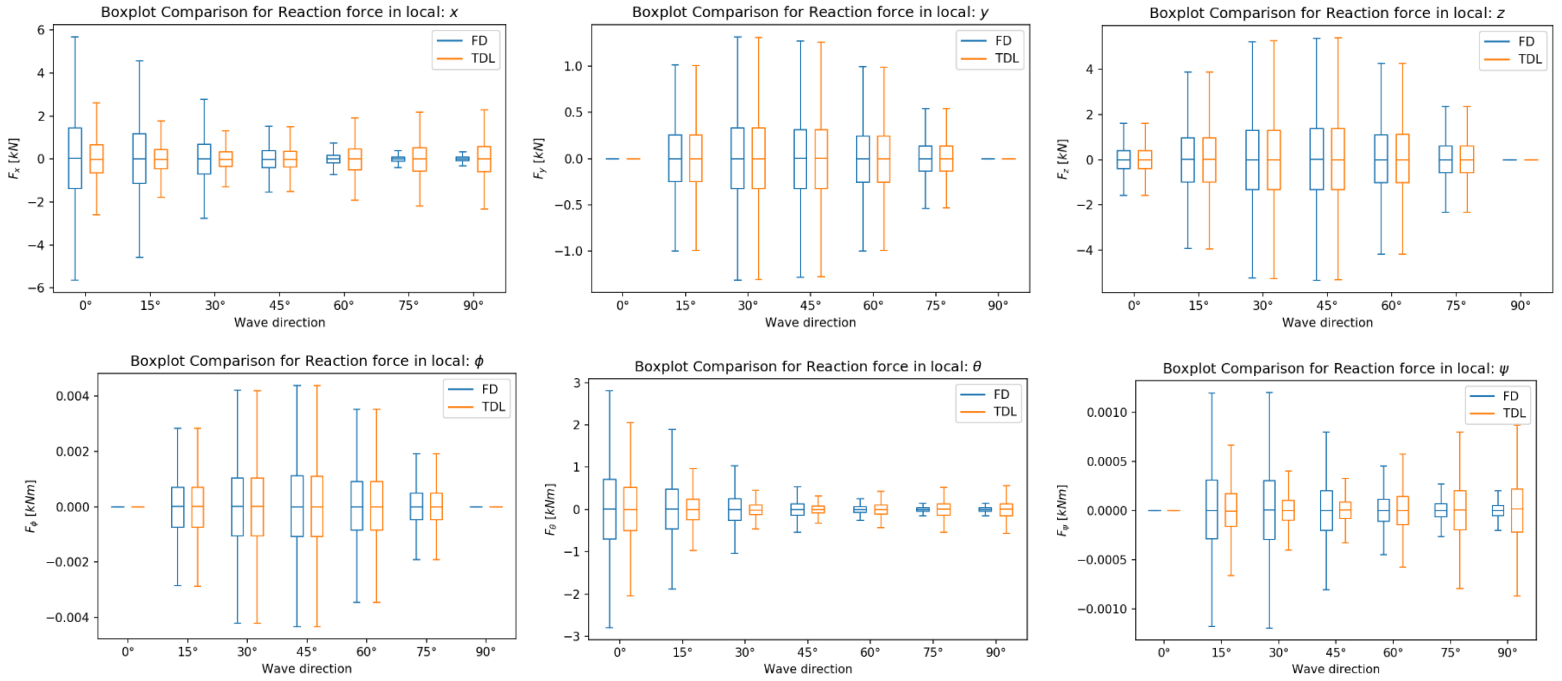
Figure 7.10: Boxplot comparison of reaction force at connection point in TDL and FD in a two interconnected floater model subject to various wave directions.
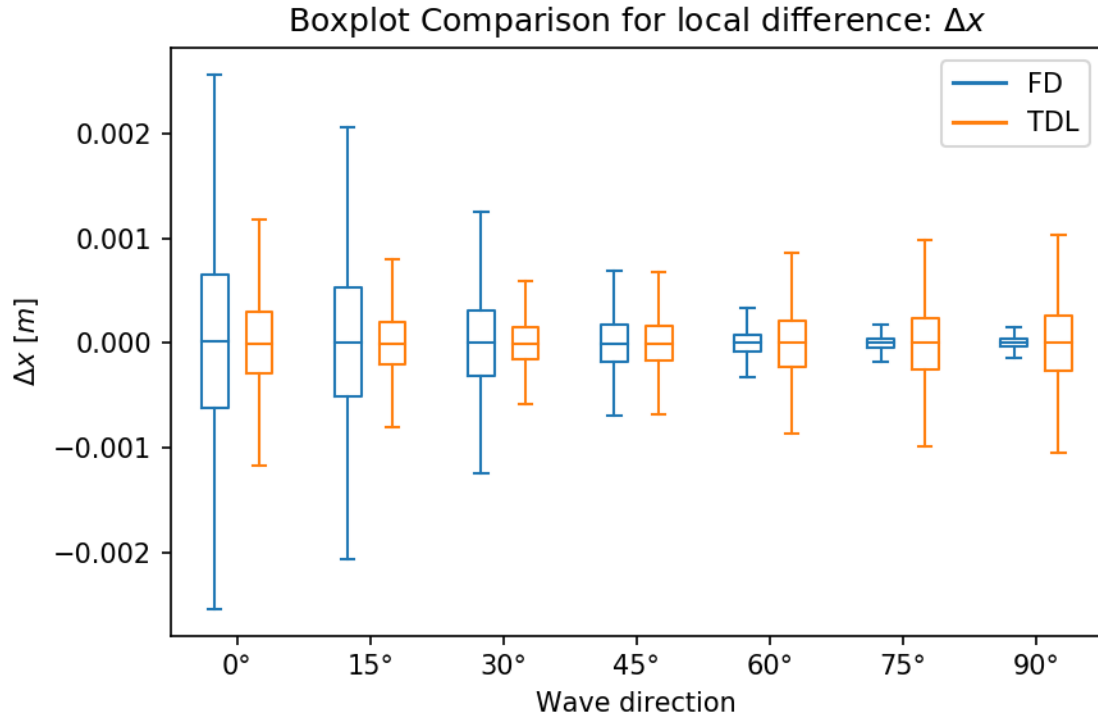

Figure 7.11: Relative motions between both floaters for various wave directions.

7.1.4 Conclusion

The frequency domain and time domain model show very strong similarity in the resulting motions of both the floaters. Nevertheless, recalculation of the occurring reaction forces at the connection points shows that small differences in the motion causes significant changes in these forces. Especially pitching motions have the largest influence on this. This causes higher axial forces and moments in the yz-plane at the connection point for beam waves in the FD-model and for head waves in the TDL-model. A re-evaluation of all hydrodynamic coefficients resulting from the radiation potential in the time domain model could be a solution to this.

7.2   Case 2: Non-Linear vs. Linear TD

In this study there is focused on the effect of linearizing the applied joint reaction forces with respect to each floater's center of gravity. The previous section showed that a direct comparison between the frequency domain and linear time domain is not convenient and therefore the comparison between the non-linear and linear joint reaction forces is performed with the time domain model (named TDL and TDNL). From the obtained motions, the relative motion between the connection points (ΔP), reaction forces (F_{local}) and local joint stresses (σ, τ) at the connection points can be calculated. Important to note is that these values need to be calculated with the linear and non-linear formula's for TDL and TDNL respectively.

7.2.1   Two floaters under beam waves in heave and pitch (4DoF)

In Figure 7.12, the heave and pitch motions of the floater under beam waves are shown after a certain time. The motion is over estimated by the linear model, which is because the small angle approximation causes that higher forces are being exerted on each floaters center of gravity from the joint reaction forces. Nevertheless, the relative motion between both floaters determines the reaction forces that were acting at the connection points. Figure 7.13 and Figure 7.14 show these reaction forces and for the non-linear model there is now also a reaction force in x-direction at the connection point. Due to linearization this axial force is not considered in the linear model with heave and pitch. Since only these two degrees of freedom for each floater are used in this case, the axial force will only give negative values (tension in this case). In other words, when there are no translational motions in the horizontal plane stated in the model and the floaters pitch, only tension occurs in the joint because of the connection points moving away from each other.

The force in z-direction at the connection point also increases in the non-linear case. This effect is also caused by exerting the axial spring in this model by the pitch motion. A transversal stiffness (in z-direction) causes that the floaters tend to pitch in anti-phase, while an axial stiffness tends the floaters to pitch with similar phase. This means that by exerting the axial spring in the non-linear model influences (increases) the relative z-motion between the connection points.
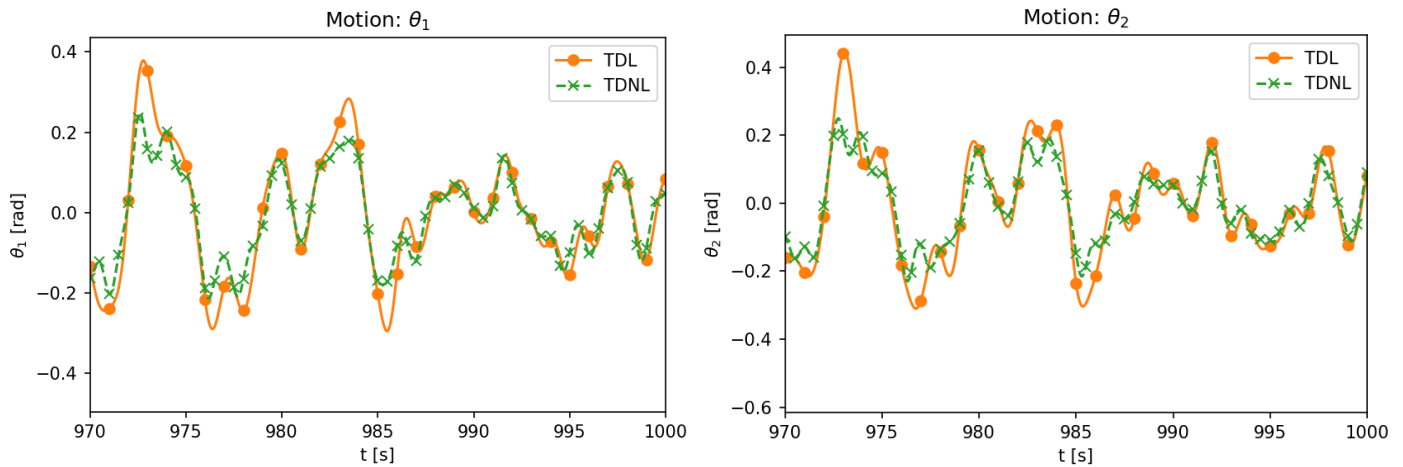

78
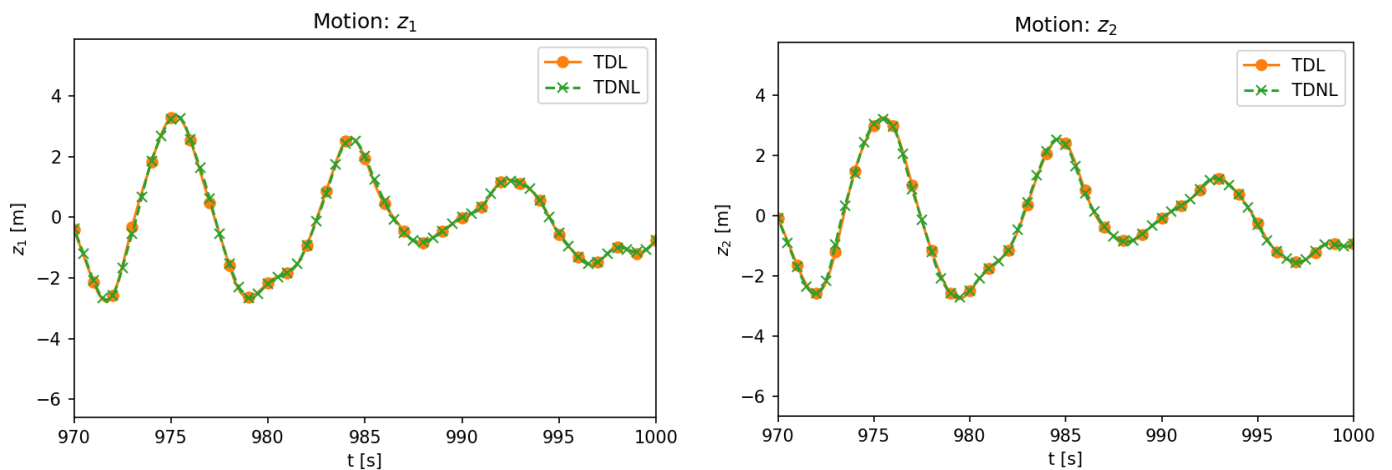
Figure 7.12 Heave and pitch motion of both floaters under beam waves with calculations in linear (TDL) and non-linear time domain (TDL).
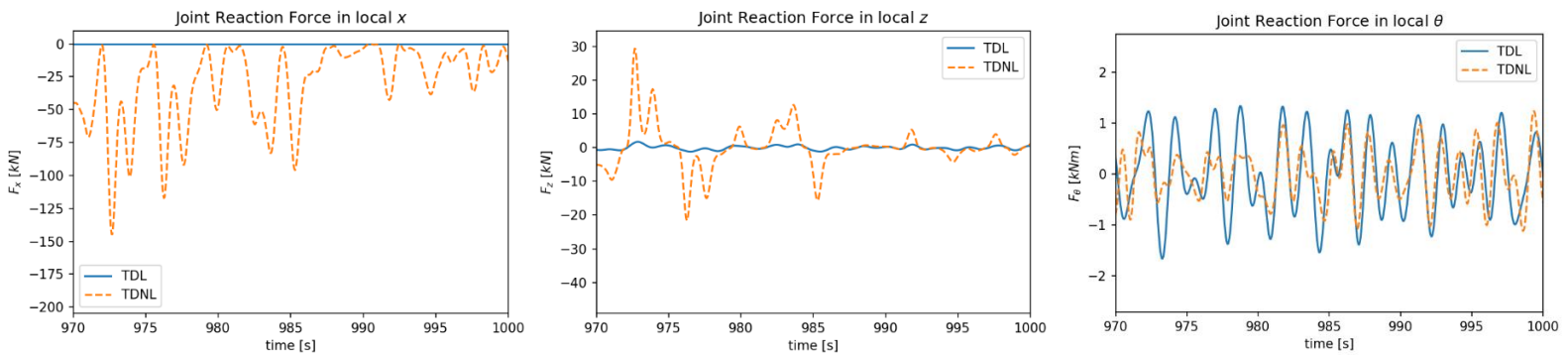

Figure 7.13: Reaction force at the connection point for TDL and TDNL for two floaters in heave and pitch in beam waves.
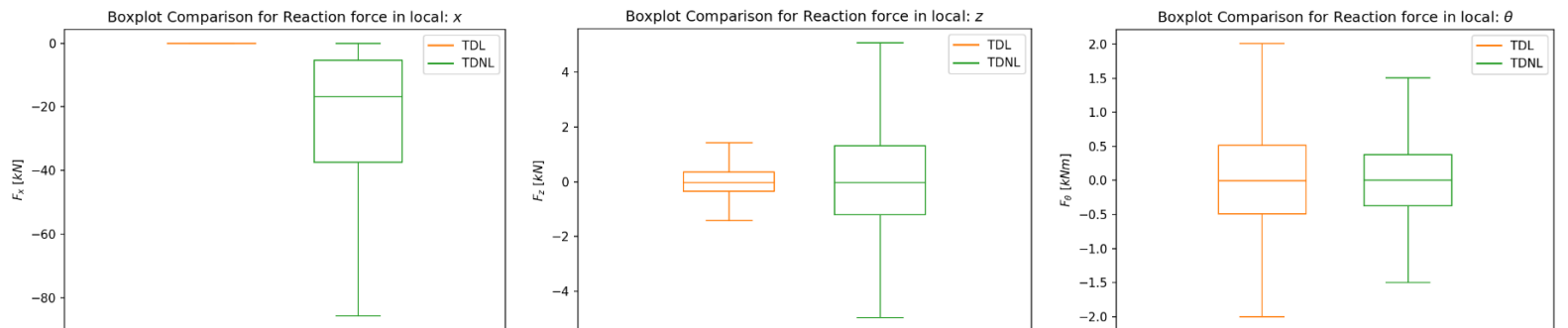

Figure 7.14: Boxplots of reaction forces at the connection point for TDL and TDNL for two floaters in heave and pitch in beam waves.

7.2.2   Two floaters in heave and pitch under various wave directions

When the wave directions are varied, it can be observed that the effect of additional axial stiffness vanishes when going towards 90°-waves. The pitching becomes less in this case, see Figure 7.15 and with that the reaction forcing of the joints in linear and non-linear time domain, become similar again. In Figure 7.17 the stresses in the joint at the connection point is shown. It can be observed that the compressive stress and tensional stress are the same in the linear time domain, since they are only

79

caused by stress by bending. The non-linear model gives very high tensional stresses due to the additional axial effect on the axial spring.
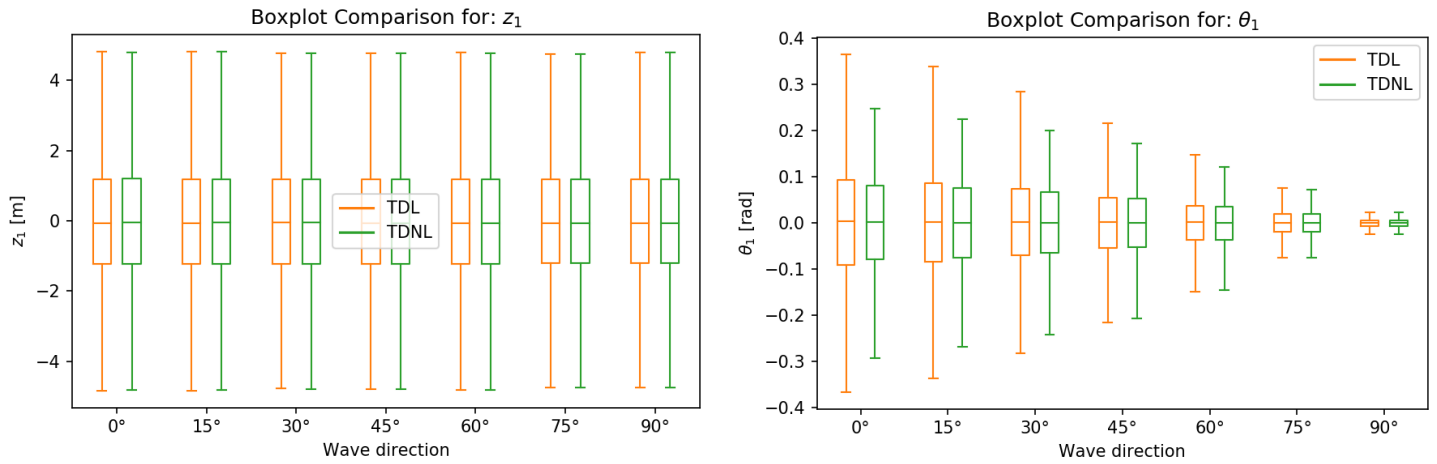

Figure 7.15: Motion in heave and pitch for TDL and TDNL for different wave directions.
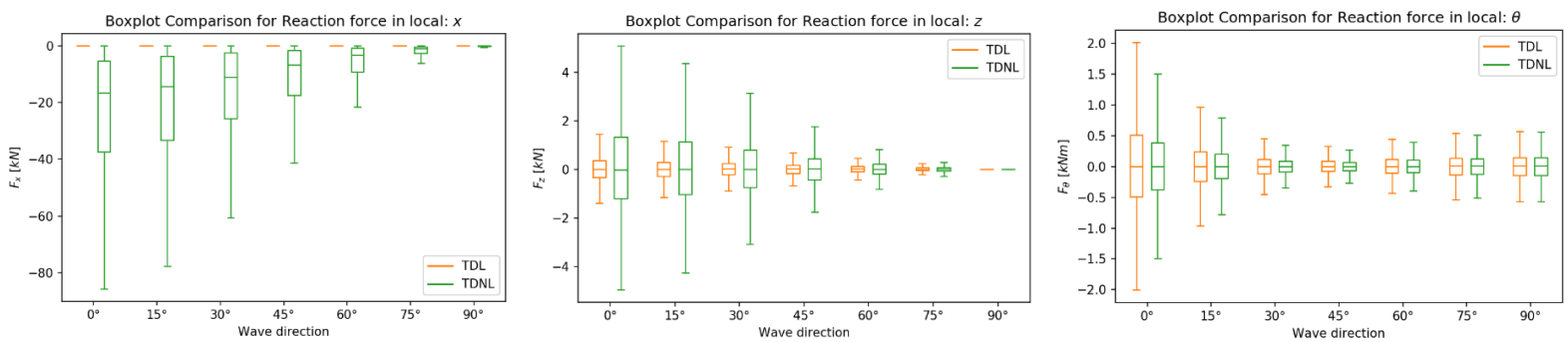
Figure 7.16: Reaction force at floaters interconnector point in local z and θ pitch for FD and TDL for different wave directions.
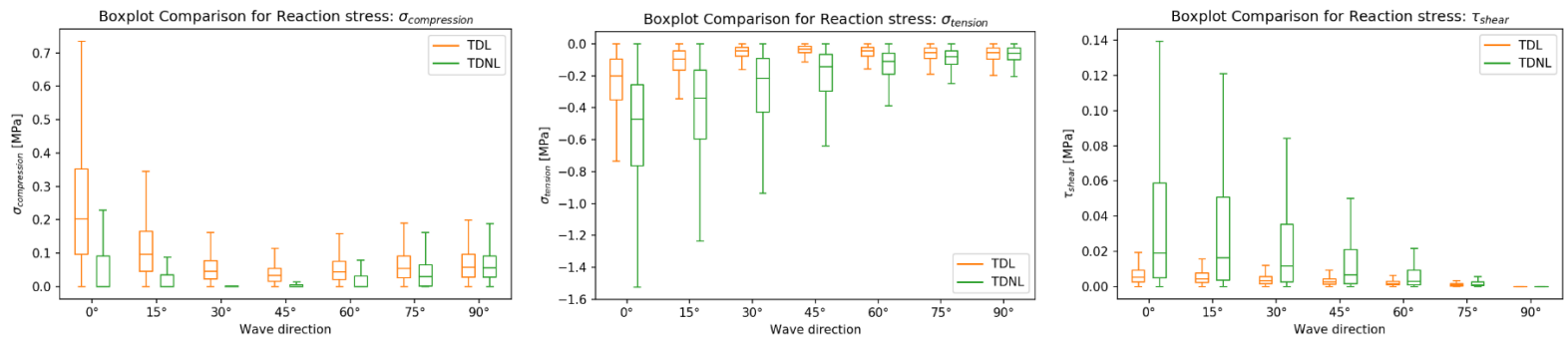
Figure 7.17: Reaction stress at interconnector point in joint.

7.2.3 Two floaters in 12DoF under various wave directions

In this case the calculation for all degrees of freedom are switched on for the linear and non-linear time domain model. In Figure 7.18 the boxplots are shown of the motions that are found for the first floaters for various wave directions (the second floater gives similar results). The two models show similar results, except in yaw (ψ). In low frequency motion the floater tends to make a larger rotational angle for wave directions below $45°$. Figure 6.2 shows the reaction force at the connection point P1 for

various wave directions. Due to the additional degrees of freedom, compared to the heave-pitch case, it can be observed that the effect of the force in the axial spring due to pitching has minimal effect on the total force in x-direction in the non-linear case, since the boxplots show similarities. The yawing gives very low reaction moments at the connection point, as the floaters tend to yaw in phase. The force in y-direction is over-estimated in the linear case. Except for $\mu = 75°$. In this case the effect of the small angle approximation in the linear time domain underestimates the forcing. Due to roll motion in the linear model vertical forces will arise at the connection points, whereas in the non-linear case also forces in the y-direction. For 75°-waves this effect of roll is significant for the acting reaction force in y-direction.
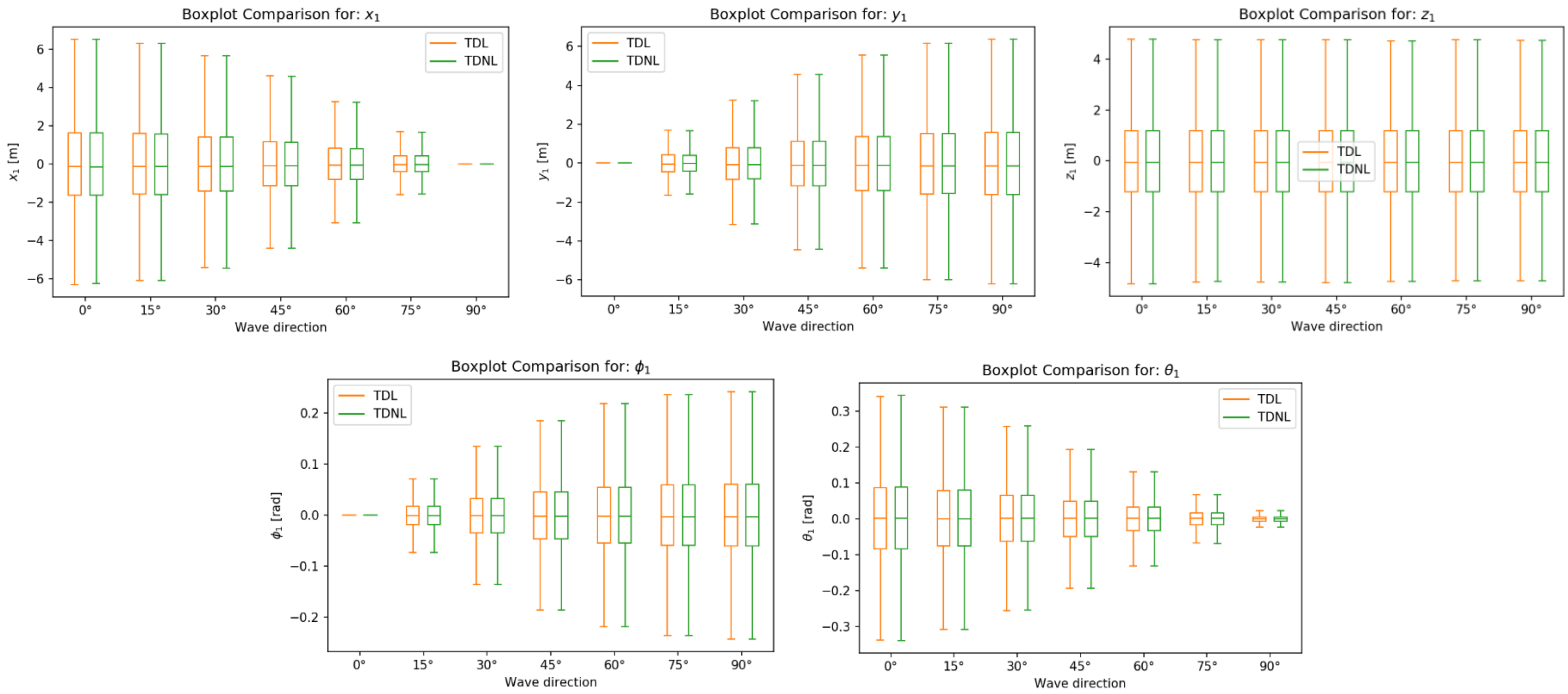
Figure 7.18: Boxplot comparison of motions in TDL and TDNL in a two interconnected floater model subject to various wave directions.
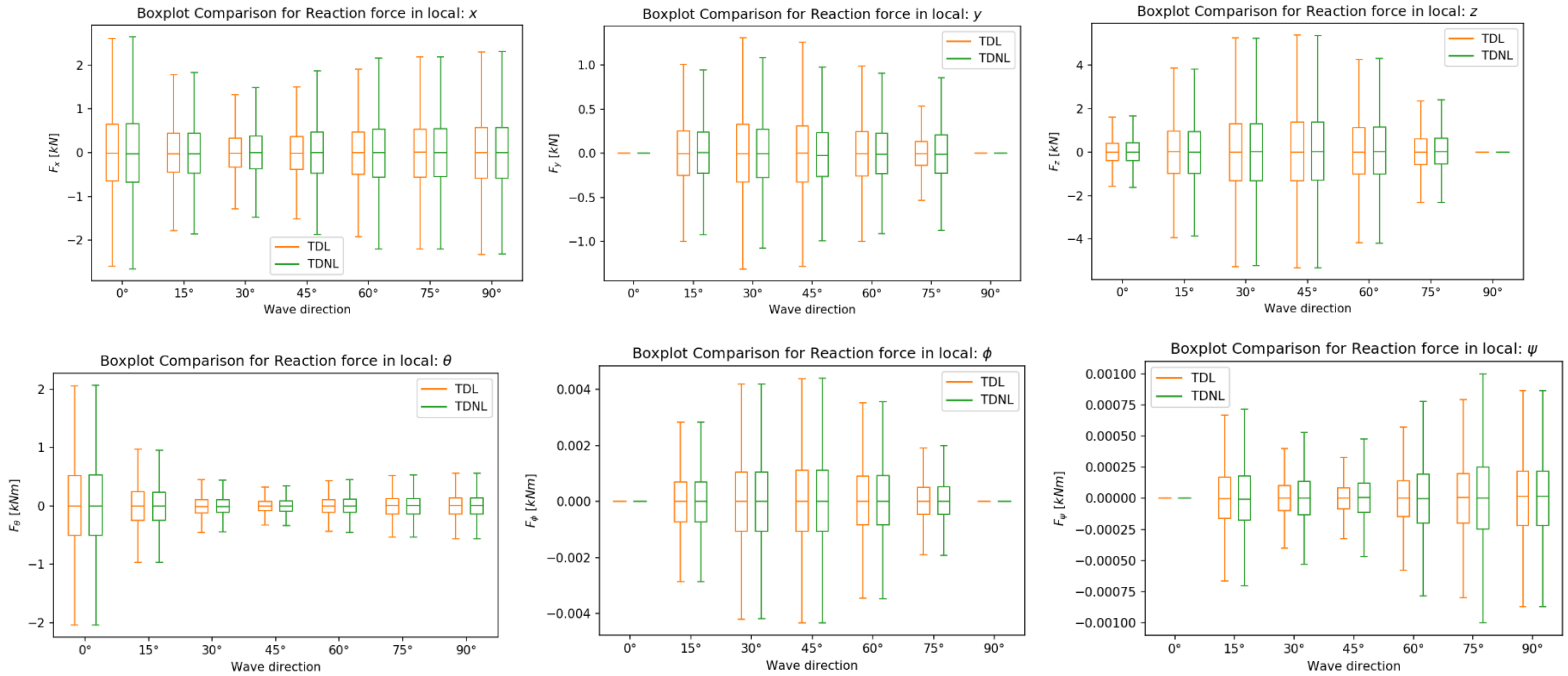
Figure 7.19: Boxplot comparison of reaction forces at the connection point in TDL and TDNL in a two interconnected floater model subject to various wave directions.

7.2.1 Conclusion

The linear and non-linear time domain model show similar results for motions of the floaters and the acting reaction forcing at the connection points when all degrees of freedom are applied. When limiting the amount of degrees of freedom (heave and pitch) the exact effect of the linearization can be studied, see section 7.2.1.. Important differences are the exertion of the axial spring when pitching and the transversal spring when rolling in the non-linear model. This last effect is noticeable in the reaction forcing for 75° wave heading, where the forces are higher in the non-linear case.

7.3   Case 3: Different joint stiffness

The joint stiffness is varied in the frequency domain model for a wave heading of $45°$, because in this case wave excitation forces will arise in all directions. Time domain calculation is possible, but a decrease in step-size would be required and this results in a significant increase in computational time for stiffer connections. Hence, the model tends to become unstable, when the time step is not small enough.

The joint dimensions are kept the same and the Young's modulus of the joint material is varied. In Figure 7.20 the maximum local reaction forces at the connection points is given for various Young's moduli. Due to the stiffer connection, some forces will decrease, due to the decrease of the relative motion between the connection points on each floater, while on the other hand forces in other directions increase. Combining these forces and calculating the overall stresses that arise at the connection point, shows that these stresses clearly increase for stiffer springs in the model, see Figure 7.21.
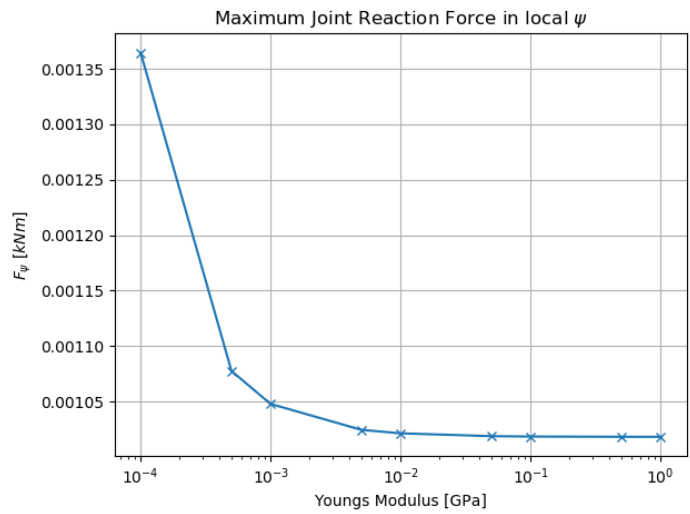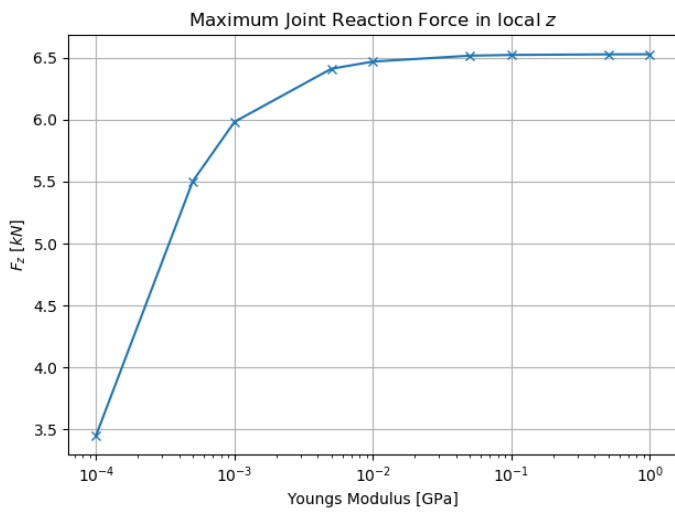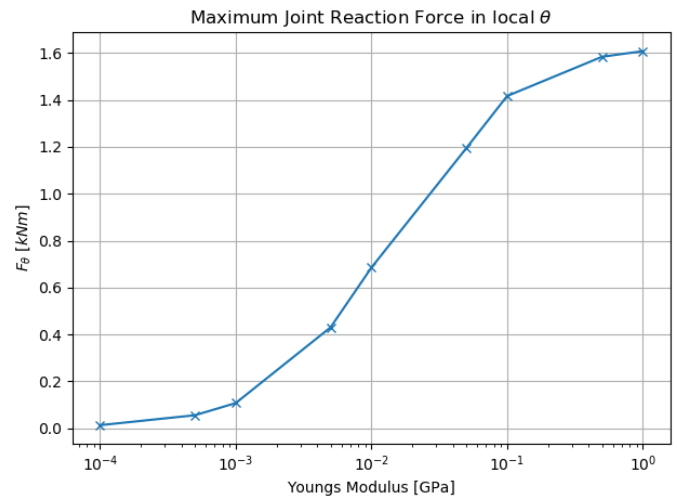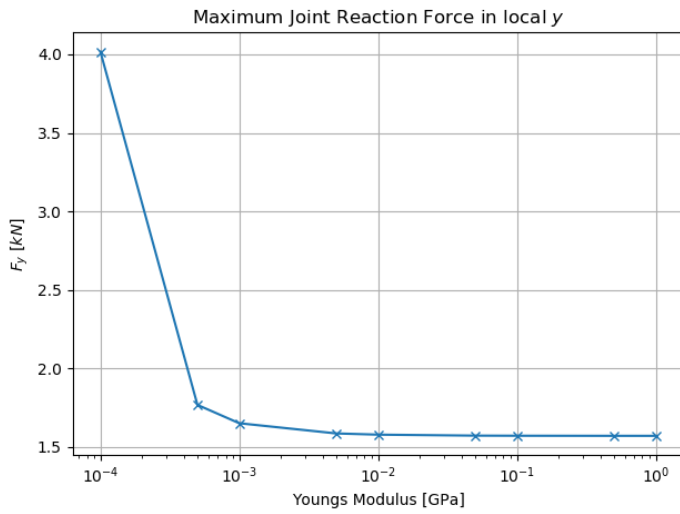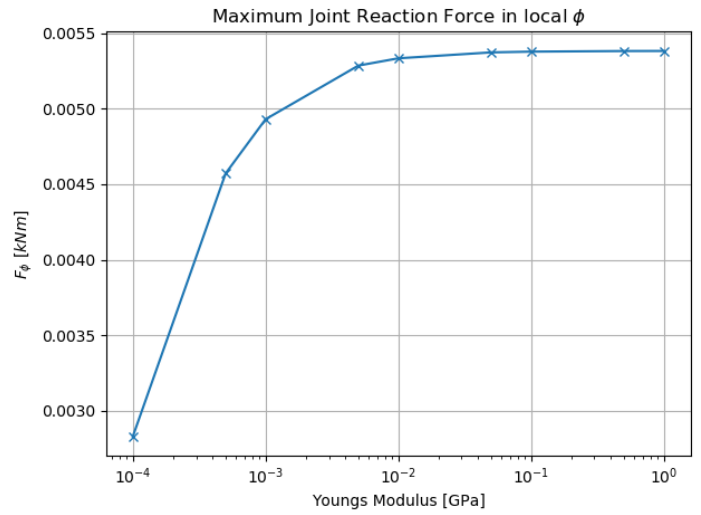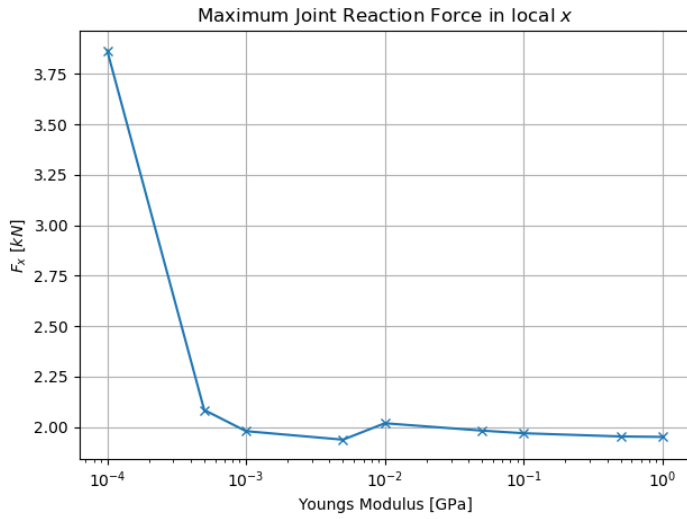
Figure 7.20: Local reaction force for different joint stiffness (Young's modulus) for wave direction $\mu = 45°$, calculated with the FD-model.
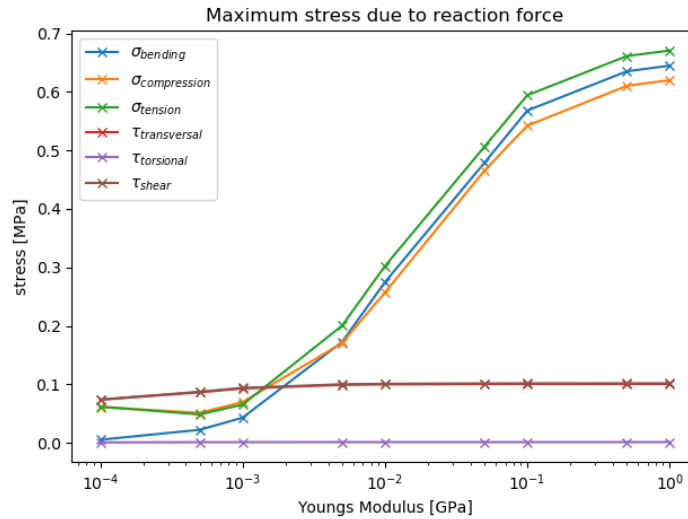
Figure 7.21: Local stress in joint at connection point on the floater for different joint stiffness (Young's modulus) for wave direction $\mu = 45°$.

The forces and stresses in Figure 7.20 and Figure 7.21 converge to a certain value. This is the joint reaction force acting where the floaters start to move together as one. As an example, Figure 7.22 shows the motion in pitch for different stiffnesses under beam waves, where clearly can be seen that the pitch of the first and second platform is the same for both.
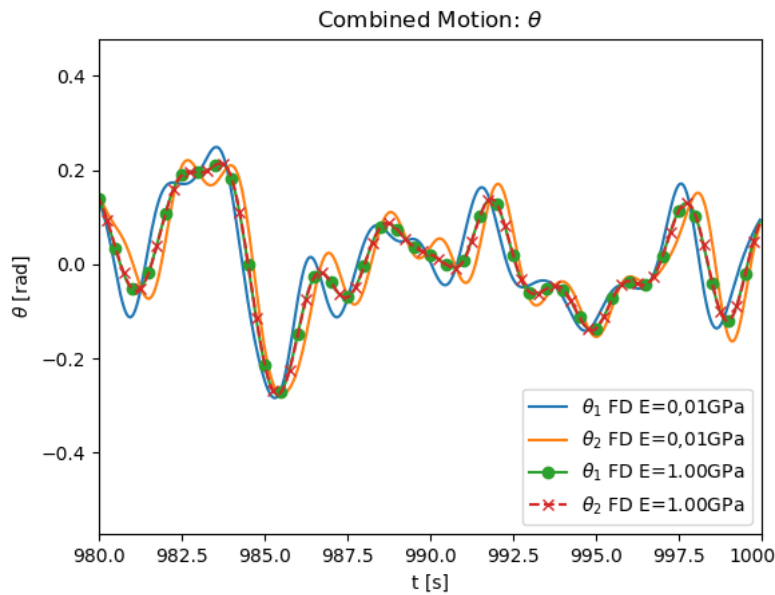
Figure 7.22: motion in pitch for different joint stiffness for wave direction $\mu = 0°$.

7.4 Conclusion

The frequency domain and linear time domain model motions are quite similar but have differences in the reaction forces at the connection points. Small differences in the motion have an impact on the calculation of the reaction forces. The small differences in the motion are caused by the calculation of the hydrodynamic coefficients in time domain.

The linear time domain model has been compared with the non-linear. The motions and reaction forces give similar results, but one should be aware of the effects of linearizing. For some wave directions the forcing can show higher results. But overall the forces in the linear model are over-estimated.

8. Discussion & Conclusion

In this chapter the research is summarized in the discussion and the findings discussed. After which recommendations are drawn from these findings. Next, the limitations of the applied theory and modelling are given, resulting in suggestions for future research. At last the main conclusions from the research are drawn.

8.1 Discussion

This study focused on the development of linear and non-linear models for interconnected offshore floating modules subject to first order wave forces, with open source software. Increasing the amount of floating bodies increases the calculation time of time-domain models, and a need for fast calculations is desired. Therefor a comparison between different models by solving the floaters' equations of motion in frequency domain (linear) and time domain (linear and non-linear). The interaction with the water (hydromechanics coefficients) is in both cases based on potential flow theory.

The most important findings can be subdivided into the following subsections: Solving potentials, Modelling in time and frequency domain, Implementation of joints and Results.

Solving potentials
Floating rigid bodies can be modelled with potential theory. Meaning that based on the radiation, diffraction and wave excitation potential the dynamic forces on the floater can be evaluated. This results in cross related frequency dependent added mass, hydrodynamic damping, wave excitation force amplitude and wave force phase shift coefficients for all degrees of freedom. These can be obtained with the open-source BEM-solver, NEMOH, and implemented in either the frequency domain or time domain (Cummin's equation) equation of motion.

Important factors to bear in mind in the generation of these coefficients is the number of panels for the mesh of the floaters being modelled. This number of panels is based on the highest wave frequency that needs to be taken into account for the time domain calculations. This is highest of the following two: the maximum occurring wave frequency or the frequency where all of the hydrodynamic damping coefficients has become zero. In this research it is always governed by the damping coefficients (modelling till 8 rad/s).

Interpolation of the hydrodynamic coefficients afterwards is convenient because it decreases the computational time of NEMOH and increases the ability to capture the whole narrow-banded wave spectrum.

As a result of modelling multiple floaters, BEM-solvers predict gap-resonances that are physically not there. Tracing the location of these resonant frequencies, cutting them out, replace them with an interpolated part and smooth the coefficients gives stable and more accurate results.

Modeling in time and frequency domain

A time domain model can be set up with several time integration schemes. For the interconnected floaters described in this report a 4th order Runge-Kutta scheme is sufficient with a step size of dt=0.05 seconds. With increasing joint stiffness, the time step needs to be further decreased to capture higher frequency motions. Firstly, the cross-related retardation function and infinite added mass matrices need to be obtained from the frequency dependent coefficients. In order to perform the convolution of the retardation function and velocity in Cummin's equation, variable time stepping is not practical and therefor a standard ODE45 solver with step size control is not convenient for solving these kinds of differential equations. Calculations in frequency domain can easily be performed with a series of matrix multiplications representing the transfer functions between motions and forces. Spectral analysis shows insight in maximum motions.

Implementation of Joints

A joint between two floaters can be implemented as six springs in each local degree of freedom. The relative displacement of each spring determines the potential energy in the system, which can be translated to forces at the floaters center of gravity with Euler-Lagrange equations. The implementation of this is performed with symbolic programming in Python, which gives the opportunity to change the characteristics of the joint (location, stiffness etc.) at all time. A linear model of the joint reaction forces can be derived assuming small angles. The implementation of the joints with Euler-Lagrange equations have shown to be a straightforward method that can be standardized for multiple floating bodies, and even can be adjusted for stopping chains for example during the calculation process.

Results

The motions in frequency domain are comparable to the ones in linear time domain. Small differences in the determination of the hydrodynamic coefficients in the time domain, can cause significant differences in the forcing at the connection points of the joints. The effect on the pitch motion (rotation around the y-axis) is most significant.

Motions are overestimated, resulting in higher amplitudes when comparing the linear and non-linear time domain model. By analyzing the degrees of freedom separate (switching them on or off in the model) the effect of the linearization can be observed, causing higher or lower forces and motions in different cases. Nevertheless, for all degrees of freedom (12DoF for two interconnected floaters), these effects are minor and the overall resulting motions and forces are of the same order for both models subject to various wave directions.

For first order wave forces the expected reaction forces and stresses are the highest in beam waves ($\mu = 0°$) and slowly decrease towards head waves. In this case the bending stresses that arise due to pitching are leading. Stresses in the joints naturally increase when the joint stiffness increases, they converge to an equilibrium for higher stiffness. This is where the floaters start to move together as one and all the forces go 'through' the connection. Especially the bending moment increases significantly in the joints, since the floaters motions are more restrained, the independent pitching of the floaters is suppressed the most.

8.2 Recommendations

This study showed that a linear model for two interconnected floating solar platforms with springs gives a good estimation of the occurring motions and interconnector reaction forces compared to a non-linear model. Both being based on potential flow theory and subject to first order wave forces. Frequency domain calculations give a good impression of the occurring motions and can be used for pre-analysis of floating solar arrays. For including significant other non-linear effects there should be switched to a time domain model.

8.3 Limitations

Several limitations of the current models are described here and subdivided into hydromechanics, joints, additional non-linear effects.

Hydromechanics

- The models in this study are based on potential theory, where normally is assumed that wave heights are small compared to the structures draft. Forces and motions are therefore more of an indication and scale model testing should be needed for validation. Next to that non-linear effects like water overflowing the structure, breaking of waves, spraying of water, partially submersion/lifting of the platform in/from the water are harder to be modelled in this way.

- The study showed that for these relatively small floaters the hydrodynamic coefficients in time domain are quite prone to inaccuracies and can lead to different behavior of the floaters and resulting forces. Meaning that standard calculation procedures for these coefficients need to be treated carefully.

- Change of the restoring force due to change of direction of gravity relative to the floaters axis systems is not considered and could play a major role on the behavior.

- For large arrays of floating solar units, wave attenuation throughout the array can play a role, which is not incorporated in the model.

Joints

- The joints are modelled as 6 springs, for the 6 degrees of freedom at the interconnections. Which can induce higher forcing on the floaters. Modelling with 4 springs (axial, transversal, bending and torsion) could give more realistic results, when the relative displacements between the connection points are evaluated and concentrated to bending or shear in one combined direction. This direction of the bending/shear can be found with vector projection of the two transversal/bending motions at the connection points.

- The reaction forces at the connection points are caused by a linear spring. Higher forces can arise in the joints due to inertial effects in the joint itself. Implementation of the joint as a finite element or -difference scheme, can give insight in this effect.

- The location of the floaters with respect to each other should carefully be analyzed when the joint stiffness is decreased. This could change the initial hydrodynamic coefficients, due to the increase in gap distance.

- The joints have been implemented as linear springs. In time domain calculations, these can also be modified to non-linear springs with stop-chains for example. That has not been applied in this research.

- No mooring is applied to the system. Mooring causes pre-tension in the system and with that increases the mean joint force or can influence the overall joint behavior.

Additional effects

Other non-linear effects not considered in the model but can be added in a follow up study, are presented below:

- Change of wave load due to change of orientation of floater

- Change in phase of load due to motions in horizontal plane

- Mooring connected to the system

- Secundary wave loads

- Viscous damping effects

8.4   Suggestions for further research

Further research should continue on the implementation of additional non-linear effects in the time domain model and study their influence on the complete system. The limitations not based on the application of potential theory can be added to the developed models.

Frequency domain calculations for larger arrays of interconnected solar panels should give insight in which interconnections the forces will become the highest. The implementation of wave attenuation throughout a large array can be studied carefully.

8.5　Conclusion

A frequency domain (linear) and time domain (linear and non-linear) model has been developed of two interconnected floating bodies, with open source tools NEMOH and Python. NEMOH gives good global results in the calculation of all hydrodynamic coefficients compared to commercial software's, whereas the understanding of the result of the software is key, to optimally use it. Especially the number of panels, phase shifts of the wave excitation force and gap resonance effects have impact on further calculations.

For the equation of motion in time domain hydrodynamic coefficients need to be calculated from the frequency domain coefficients. The added mass at infinite frequency and the retardation function must be evaluated for sufficient length in time and convoluted with the velocities at previous time steps. An RK4 integration scheme with fixed time stepping is most convenient for this application.

While the linear frequency domain equation of motion can be rewritten into a set of transfer functions between forcing and motion. A multiplication with the wave to force transfer function gives the immediate complex transfer function between wave elevation and motion.

The interconnections are modelled as springs between the floaters and the influence on the motions in the floaters center of gravity is found by evaluating the potential energy stored in the springs. A linear model of the joint reaction forces can be derived assuming small angles. The implementation of the joint reaction forces with Euler-Lagrange equations have shown to be a straightforward method that can be standardized for multiple floating bodies, and even can be adjusted for stopping chains.

The effect of gap resonance, due to assumptions in BEM-solvers, is clearly visible in the hydrodynamic coefficients. It has mainly an effect on the overall calculation time in time domain, since the convolution of the retardation function needs to be evaluated for a longer period in time. A suppression of the gap resonant peaks with linear interpolation and smoothening showed significant improvement in the calculation time.

The frequency domain and linear time domain model motions are quite similar but have differences in the reaction forces at the connection points. Small differences in the motion have an impact on the calculation of the reaction forces. The small differences in the motion are caused by the calculation of the hydrodynamic coefficients in time domain.

The linear time domain model has been compared with the non-linear. The motions and reaction forces give similar results, but one should be aware of the effects of linearizing. For some wave directions the forcing can show higher results. But overall the forces in the linear model are over-estimated.

9. References

(n.d.).

Babarit, A. (2014). *General Notations and Conventions.* Nantes: LHEEA Centrale.

Babarit, A., & Delhommeau, G. (2015). *Theoretical and numerical aspects of the open source BEM solver NEMOH.* Nantes: 11th European Wave and Tidal Energy Conference (EWTEC2015).

Babarit, A., & Delhommeau, G. (2015). *Theoretical and numerical aspects of the open source BEM solver NEMOH.* Nantes, France: 11th European Wave and Tidal Energy Conference.

Brandt, A. (2011). *Noise and Vibration Analysis.* Chichester: John Wiley & Sons, Ltd.

Bunnik, T., Pauw, W., & Voogt, A. (2009). *Hydrodynamic Analysis for Side-by-Side Offloading.* Osaka: International Offshore and Polar Engineering Conference.

Cruz, J., & Salter, S. (2006). *Numerical and experimental modelling of a modified version of the Edinburgh Duck wave energy device.* Edinburgh: IMechE.

Dinoi, P. (2016). *Analysis of wave resonant effects in-between offshore vessels arranged side-by-side.* Madrid: Universidad Politécna de Madrid.

DNV. (2010). *Environmental Conditions and Environmental Loads.* Det Norske Veritas.

Folley, M., Babarit, A., Child, B., Forehand, D., O'Boyle, L., Silverthorne, K., . . . Troch, P. (2012). *A REVIEW OF NUMERICAL MODELLING OF WAVE ENERGY CONVERTER ARRAYS.* Rio de Janeiro: 31st International Conference on Ocean, Offshore and Arctic Engineering.

Fournier, J., Naciri, M., & Chen, X. (2006). *Hydrodynamics of two side-by-side vessels, experiments and numerical simulations.* San Francisco: International Offshore and Polar Engineering Conference.

Hairer, E., Norsett, S., & Wanner, G. (1993). *Solving Ordinary Differential Equations i. Nonstiff Problems.* Geneve: Springer Series in Computational Mathematics.

Holhuijsen, L. H. (2010). *Waves in oceanic and coastal waters.* Camebridge University.

Huijsmans, R., Pinkster, J., & Wilde, J. (2001). *Diffraction and radiation of waves around side by side moored vessels.* Stavanger, Norway: International Offshore and Polar Eng Conference.

Journee, & Massie. (2001). *Offshore Hydromechanics.* TU Delft.

Journée, J., & Massie, W. (2001). *Offshore Hydromechanics.* Delft: Delft University of Technology.

Koo, W., & Kim, J.-D. (2015). *Simplified formulas of heave added mass coefficients at high frequency for various two-dimensional bodies in a finite water depth.* Incheon: Int. J. Nav. Archit. Ocean Eng.

Marin. (2018). *aNySIM theory documentation.* Wageningen: Marin.

MARIN. (2018). *aNySIM Theory Documentation.* Wageningen: MARIN.

Molin, B. (2009). *Experimental and numerical study of the gap resonances in-between two rectangular barges.* Istanbul: 13th Congress of Intl. Maritime Assoc. of Mediterranean.

Newman. (2003). *Application of generalized modes for the simulation of free surface patches in multi body hydrodynamics.* Wamit consortium report.

Oceans of Energy B.V. (2018, Februari 06). *New consortium builds first offshore floating solar energy farm in the world Project 'Solar-at-Sea' starts*. Retrieved from Oceansofenergy.blue: https://oceansofenergy.blue/press-release-1-new-consortium-builds-first-offshore/

Ogilvie, T. (1964). *Recent progress towards the understanding and prediction of ship motions.* Proc. 5th Symposium on Naval Hydrodynamics.

Pena, B., & McDougall, A. (2016). *An investigation into the limitations of the panel method and the gap effect for a fixed and a floating structure subject to waves.* Busan, South Korea: International Conference on Ocean, Offshore and Arctic Engineering.

Penalba, M., Kelly, T., & Ringwood, J. V. (2017). *Using NEMOH for Modelling Wave Energy Converters: A Comparative Study with WAMIT.* Co.Kildare, Ireland: Centre for Ocean Energy Research (COER), Maynooth University.

Perez, T., & Fossen, T. (2009). *A Matlab Toolbox for Parametric Identification of Radiation-Force Models of Ships and Offshore Structures.* Callaghan, Australia: Modelling, Identification and Control.

Stewart, R. (2000). *Introduction to Physical Oceanagrophy.* Texas: A & M University.

The SciPy community. (2019). *docs.scipy.org*. Retrieved from scipy.org: https://docs.scipy.org/doc/scipy/reference/generated/scipy.integrate.ode.html

Trapani, K., & Redon Santafe, M. (2014). *A review of floating photovoltaic installations 2007–2013.* Prog. Photovolt: Res. Appl.

Vuik, C., van Beek, P., Vermolen, F., & van Kan, J. (2006). *Numerieke Methoden voor Differentiaalvergelijkingen.* Delft: VSSD.

10. Appendices

Contents

A: 3D Potential flow theory

For a free-floating body, with its own axis system in its center of gravity as shown in Figure 2.1, the potentials are with respect to a fixed earth-bound axes system. The following appendix is based on findings in (Journée & Massie, 2001).

The total potential is a superposition of the radiation, wave excitation and diffraction potential:

$$\Phi = \sum_{j=1}^{6} \Phi_{r,j} + \Phi_w + \Phi_d$$

Main assumptions in potential theory are:

- The fluid is incompressible
- Inviscid
- Irrotational
- And no effects of surface tension

The potentials have to satisfy the following boundary conditions (Journée & Massie, 2001):

1. Laplace equation:
$$\frac{\partial^2 \Phi}{\partial x^2} + \frac{\partial^2 \Phi}{\partial y^2} + \frac{\partial^2 \Phi}{\partial z^2} = 0$$

2. Sea bed boundary condition:
$$\frac{\partial \Phi}{\partial z} = 0 \ at \ z = -h_o$$

3. Free surface boundary condition:
$$g\frac{\partial \Phi}{\partial z} + \frac{\partial^2 \Phi}{\partial t^2} = 0 \ at \ z = \eta$$

4. Kinematic boundary condition on the oscillating body surface:
$$g\frac{\partial \Phi}{\partial z} = \vec{v}.\vec{z}$$

5. Radiation condition:
$$\lim_{R \to \infty} \Phi = 0$$

6. Symmetric and anti-symmetric condition
$$\Phi_2(-x,y) = -\Phi_2(x,y)$$
$$\Phi_3(-x,y) = \Phi_3(x,y)$$
$$\Phi_4(-x,y) = -\Phi_4(x,y)$$

A.1 Radiation potential

With the radiation potential the radiation force F_r can be calculated. The radiation potential is given as:

$$\Phi_r = \Phi_{r,a}\cos\left(\omega_t + \epsilon_{\Phi_r,u} + \epsilon_{u,\zeta}\right) = \Re\left[\Phi_{r,a}e^{-i\epsilon_{\Phi_r,u}}e^{-i\epsilon_{\zeta,u}}e^{-i\omega t}\right] = \Re\left[\widehat{\Phi}_r e^{-i\epsilon_{\zeta,\omega}}e^{-i\omega t}\right]$$

The radiation potential is the summation of the radiation potential in all directions: $\Phi_r = \sum_{j=1}^{6}\Phi_{r,j}$

The radiation potential can be written in terms of the space dependent $\phi_{r,j}$, instead of space and time dependent Φ_r. This is basically a transfer function from velocity to potential.

$$\Phi_r(x,y,z,t) = \sum_{j=1}^{6}\Re\left[\frac{\widehat{\Phi}_{r,j}}{\hat{u}_j}\hat{u}_j e^{-i\omega t}\right] = \sum_{j=1}^{6}\phi_{r,j}(x,y,z)v_j(t)$$

Where: $v_j = \Re\left[-i\omega\hat{u}_j e^{-i\omega t}\right]$ and $\phi_{r,j} = \Re\left[\frac{\widehat{\Phi}_{r,j}}{-i\omega\hat{u}_j}\right]$

In this way the velocity perpendicular to the surface can be written as:

$$\frac{\partial\Phi_r}{\partial n_i} = \sum_{j=1}^{6}\frac{\partial\phi_j}{\partial n_i}v_j$$

Where n is the outward normal vector on the surface considered. The pressure from the potential with the linearized Bernoulli equation is:

$$p = -\rho\frac{\partial\Phi_{r,j}}{\partial t}$$

In this way the force and moment from the radiation can be described:

$$F_{r,i,j} = -\iint_S p_{r,j}n_i dS = \rho\iint_S \frac{\partial\Phi_{r,j}}{\partial t}n_i dS = \rho\iint_S \frac{\partial v_j}{\partial t}\phi_{r,j}n_i dS$$

$$M_{r,i,j} = -\iint_S p_{r,i,j}(r\times n)_i dS$$

It is proceeded with the force only for this case. This force could also be represented in terms of a transfer function and split into a part relative to the velocity and a part relative to the acceleration:

$$F_{r,i,j} = \Re\left[F_{r,i,j,a}e^{-i\epsilon_{u_j,\eta}}e^{-i\omega t}\right] = \Re\left[\frac{\widehat{F}_{r,i,j}}{\hat{u}_j}\hat{u}_j e^{-i\omega t}\right] = -a_{ij}\Re\left[(-i\omega)^2\hat{u}_j e^{-i\omega t}\right] - b_{ij}\Re\left[(-i\omega)\hat{u}_j e^{-i\omega t}\right]$$

So that the following holds:

$$\rho\iint_S -v_j i\omega\phi_{r,j}n_i dS = -a_{ij}\Re\left[(-i\omega)^2\hat{u}_j e^{-i\omega t}\right] - b_{ij}\Re\left[(-i\omega)\hat{u}_j e^{-i\omega t}\right]$$

Eliminating $\hat{u}_j e^{-i\omega t}$ from this equation and taking away the real part notation the following is found:

$$\iint_S -\rho\phi_{r,j}\omega^2 n_i dS = a_{ij}\omega^2 + b_{ij}i\omega$$

This results in the following statements of the added mass and hydrodynamic damping:

$$a_{ij} = \Re\left[\iint_S -\rho\phi_{rj}n_i dS\right]$$

$$b_{ij} = \Im\left[\iint_S -\rho\phi_{rj}\omega n_i dS\right]$$

A.2 Wave excitation force potential

The first order wave excitation forces consists of the undisturbed wave force and the DIFFRACtion force:

$$F_e = F_w + F_d$$

The undisturbed wave potential can be described as:

$$\Phi_w(x,y,z,t) = \frac{\zeta_a g}{\omega}e^{kz}\sin(kx\cos(\mu) + ky\sin(\mu) - \omega t) = -\Re\left[\frac{\zeta_a g}{\omega}e^{kz}e^{i(kx\cos(\mu)+ky\sin(\mu))}e^{-i\omega t}\right]$$

With the corresponding dispersion relation for water depth d: $\omega^2 = kg\tanh(kd)$

Similar to the radiation potential it is desired to write the potential as space dependent, rather than space and time dependent. This can be done by writing the function as a transferfunction, with respect to the surface elevation velocity at the origin $(\dot{\zeta}_o)$.

$$\Phi_w(x,y,z,t) = -\Re\left[i\frac{g}{-i\omega^2}e^{kz}e^{i(kx\cos(\mu)+ky\sin(\mu))} - i\omega\zeta_{o,a}e^{-i\omega t}\right]$$
$$= \Re\left[\frac{g}{\omega^2}e^{kz}e^{i(kx\cos(\mu)+ky\sin(\mu))}\dot{\zeta}_o\right] = \Re\left[\phi_0(x,y,z)\dot{\zeta}_o(t)\right]$$

The same procedure can be followed for the DIFFRACtion potential:

$$\Phi_d(x,y,z,t) = \Re\left[\phi_7(x,y,z)\dot{\zeta}_o(t)\right]$$

The wave excitation force becomes then:

$$F_{wkj} + F_{dkj} = \iint_S \rho\left(\frac{\partial\Phi_{wj}}{\partial t} + \frac{\partial\Phi_{dj}}{\partial t}\right)n_k dS = -\rho\omega^2\zeta_o e^{-i\omega t}\iint_S(\phi_0 + \phi_7)n_i dS$$

A.3 BEM solvers

BEM solvers using a panel method have an approach of solving the potentials. The potentials $\phi_{r,j}, \phi_0, \phi_7$ are obtained with source strengths on the wetted surface and are transferred to the potentials with Green's functions that satisfy the boundary conditions. More information about these routines can be found in **(verwijzing) Journee en massie** from section 7.4.2 onwards.

B: Euler-Lagrange equation

The Euler-Lagrange equation to compose the equation of motion for multiple degrees of freedom system is given as:

$$\frac{d}{dt}\frac{\partial \mathcal{L}}{\partial \dot{u}_i} - \frac{\partial \mathcal{L}}{\partial u_i} = F_i$$

With the Lagrangian Function: $\mathcal{L} = \mathcal{T} - \mathcal{V}$.

Where:

$\mathcal{T}$ Kinetic energy

$\mathcal{V}$ Potential energy

u Motion in degree of freedom i

F External forcing in degree of freedom i

For clarification purposes the equation of motion is derived for a single mass spring system, with no external forcing.
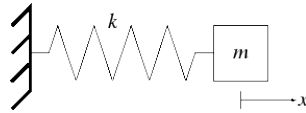
The kinetic and potential energy and the corresponding Lagrangian are as follows.

$$\mathcal{T} = \frac{1}{2}m\dot{x}^2, \mathcal{V} = \frac{1}{2}kx^2 \rightarrow \mathcal{L} = \frac{1}{2}m\dot{x}^2 - \frac{1}{2}kx^2 \qquad \text{(Eq. 0.1)}$$

Following the Euler-Lagrange procedure:

$$\frac{d}{dt}\frac{\partial \mathcal{L}}{\partial \dot{x}} = \frac{d}{dt}\frac{\partial}{\partial \dot{x}}\left(\frac{1}{2}m\dot{x}^2\right) = m\ddot{x}$$

$$\frac{\partial \mathcal{L}}{\partial x} = \frac{\partial}{\partial x}\left(-\frac{1}{2}kx^2\right) = -kx$$

$$m\ddot{x} + kx = 0$$

$$m\ddot{x} = -kx \leftrightarrow m\ddot{x} = \frac{-\partial \mathcal{V}}{\partial x}$$

This shows that the potential energy determines the spring term forcing on the mass. By only taking the potential energy into account the forcing of the springs of two interconnected floaters becomes in a more general form:

$$F_{joint,i} = \frac{-\partial \mathcal{V}}{\partial u_i}$$

C: Linearization

For calculations in the frequency domain only linearized terms are allowed. The following section will elaborate on linearizing the obtained non-linear joint forcing F_{joint}.

Linearization can be accomplished by assuming the small angle approximation derived from first order Taylor expansion:

$$\cos(\phi) \approx 1, \sin(\phi) \approx \phi \qquad \text{(Eq. 0.1)}$$

This is an assumption that is not valid with the expected rotations of the platform. Nevertheless, the influence is investigated in order to determine if a linear approximation for these kinds of applications is useful.

Applying the small angle approximation does not give linear terms immediately and therefore the procedure is analyzed more carefully for pitch (rotation around the y-axis). The forcing in this degree of freedom shows non-linear terms that will not vanish by applying the small angle approximation.

This is caused by the square term in the potential energy calculation, see Appendix B. Since the motions at a point P on the side of the floater consists of a combination of rotations and translations relative to the floaters CoG, still square terms arise in the joint forcing after applying the small angle approximation. These terms are set to zero and just skipped to fulfill the linearization.

C.1 Symbolic programming solution

To come to a convenient way to solve this matter with symbolic programming, it is desirable to know which factors can cause this effect.

Therefor it is suggested to map out the possible combinations in the potential energy equation for the 12 DoF model of two interconnected floaters. In the Euler-Lagrange equation the derivative is taken of this potential energy and it can be seen if the small angle approximation, gives complete linearization, see Table 0.1.

Table 0.1: Overview of differentiation and linearization with small angle approximation, with a and b being different degrees of freedom.

Possible term in potential energy: $f(a, b)$	Derivative of term: $\frac{\partial f(a,b)}{\partial a}$	Small angle approximation of derivative
$\cos(a)\cos(a)$	$-\sin(a)\cos(a)$	$-a$
$\cos(a)\cos(b)$	$-\sin(a)\cos(b)$	$-a$
$\sin(a)\sin(a)$	$\cos(a)\sin(a)$	a
$\sin(a)\sin(b)$	$\cos(a)\sin(b)$	b
$a\cos(b)$	$\cos(b)$	1

$\cos(a)\, b$	$-\sin(a)\, b$	$-ab$
$a\sin(b)$	$\sin(b)$	b
$\sin(a)\, b$	$\cos(a)\, b$	b

Other cross terms in the potential energy will vanish automatically due to symmetry in the system, with two joints placed on the corners of the floater, being the following possibilities:

$\sin(a)\cos(b)$	$\cos(a)\cos(b)$	1
$\cos(a)\sin(b)$	$-\sin(a)\sin(b)$	$-ab$

Therefor for these does not need to be corrected. Note that the variables within the sinusoidal functions are always rotational degrees of freedom, and when a multiplication of a sinusoidal with another variable takes place, the variable multiplicated with the sinusoidal is a translational variable.

Knowing this, the procedure can easily be implemented in a script after taking the derivative of the potential energy. The complete non-linear forcing vector by the joints for all the degrees of freedom is then obtained. A code that searches for the derivative with the shape $(\sin(a)\, b)$ (with a and b being any degree of freedom in the system) and replaces it with zero.

Afterwards the small angle approximation is applied to the forcing vector, which carries out the following replacement procedure $\cos(a) = 1, \sin(a) = a$, with a=any rotational degree of freedom.

This results in a linear joint forcing vector that represents the interaction between the two floaters in the joints: $F_{joint,linear}$.

D: Joint stiffness forcing

D.1 Linearized Joint stiffness matrix

The non-linear joint forces with respect to the floaters' centers of gravity obtained with the potential energy part of the Euler-Lagrange equation looks the following:

$$F_{joint} = \left[F_{joint,x1}, \cdots, F_{joint,\psi1}, F_{joint,x2}, \cdots, F_{joint,\psi2}\right]^T$$

Applying the differentiation procedure leads to the following forcing on the first floater in its degrees of freedom. The forces on the second floater look similar.

$$\begin{aligned}
F_{joint,x1} = -\frac{k_a}{2}&(-2a\,sin(\psi_1) + 2a\,sin(\psi_2) + 2b\,cos(\psi_1) + 2b\,cos(\psi_2) + 2b\,cos(\theta_1) + 2b\,cos(\theta_2) - 8b \\
&+ 2x_1 - 2x_2) - \frac{k_a}{2}(2a\,sin(\psi_1) - 2a\,sin(\psi_2) + 2b\,cos(\psi_1) + 2b\,cos(\psi_2) + 2b\,cos(\theta_1) \\
&+ 2b\,cos(\theta_2) - 8b + 2x_1 - 2x_2)
\end{aligned}$$

$$\begin{aligned}
F_{joint,y1} = -\frac{k_s}{2}&(-2a\,cos(\phi_1) + 2a\,cos(\phi_2) - 2a\,cos(\psi_1) + 2a\,cos(\psi_2) + 2b\,sin(\psi_1) + 2b\,sin(\psi_2) + 2y_1 \\
&- 2y_2) - \frac{k_s}{2}(2a\,cos(\phi_1) - 2a\,cos(\phi_2) + 2a\,cos(\psi_1) - 2a\,cos(\psi_2) + 2bsin(\psi_1) \\
&+ 2bsin(\psi_2) + 2y_1 - 2y_2)
\end{aligned}$$

$$\begin{aligned}
F_{joint,z1} = -\frac{k_s}{2}&(-2a\,sin(\phi_1) + 2a\,sin(\phi_2) - 2bsin(\theta_1) - 2bsin(\theta_2) + 2z_1 - 2z_2) - \frac{k_s}{2}(2a\,sin(\phi_1) \\
&- 2a\,sin(\phi_2) - 2bsin(\theta_1) - 2bsin(\theta_2) + 2z_1 - 2z_2)
\end{aligned}$$

$$\begin{aligned}
F_{joint,\phi1} = ak_s&(-a\,sin(\phi_1) + a\,sin(\phi_2) - bsin(\theta_1) - bsin(\theta_2) + z_1 - z_2)cos(\phi_1) - ak_s(a\,sin(\phi_1) \\
&- a\,sin(\phi_2) - bsin(\theta_1) - bsin(\theta_2) + z_1 - z_2)cos(\phi_1) - ak_s(-a\,cos(\phi_1) + a\,cos(\phi_2) \\
&- a\,cos(\psi_1) + a\,cos(\psi_2) + bsin(\psi_1) + bsin(\psi_2) + y_1 - y_2)sin(\phi_1) + ak_s(a\,cos(\phi_1) \\
&- a\,cos(\phi_2) + a\,cos(\psi_1) - a\,cos(\psi_2) + bsin(\psi_1) + bsin(\psi_2) + y_1 - y_2)sin(\phi_1) - k_t(2\phi_1 \\
&- 2\phi_2)
\end{aligned}$$

$$\begin{aligned}
F_{joint,\theta1} = bk_a&(-a\,sin(\psi_1) + a\,sin(\psi_2) + b\,cos(\psi_1) + b\,cos(\psi_2) + b\,cos(\theta_1) + b\,cos(\theta_2) - 4b + x_1 \\
&- x_2)sin(\theta_1) + bk_a(a\,sin(\psi_1) - a\,sin(\psi_2) + b\,cos(\psi_1) + b\,cos(\psi_2) + b\,cos(\theta_1) + b\,cos(\theta_2) \\
&- 4b + x_1 - x_2)sin(\theta_1) + bk_s(-a\,sin(\phi_1) + a\,sin(\phi_2) - bsin(\theta_1) - bsin(\theta_2) + z_1 \\
&- z_2)cos(\theta_1) + bk_s(a\,sin(\phi_1) - a\,sin(\phi_2) - bsin(\theta_1) - bsin(\theta_2) + z_1 - z_2)cos(\theta_1) \\
&- k_r(2\theta_1 - 2\theta_2)
\end{aligned}$$

$$\begin{aligned}
F_{joint,\psi1} = -\frac{k_a}{2}&(-2a\,cos(\psi_1) - 2bsin(\psi_1))(-a\,sin(\psi_1) + a\,sin(\psi_2) + b\,cos(\psi_1) + b\,cos(\psi_2) + b\,cos(\theta_1) \\
&+ b\,cos(\theta_2) - 4b + x_1 - x_2) - \frac{k_a}{2}(2a\,cos(\psi_1) - 2bsin(\psi_1))(a\,sin(\psi_1) - a\,sin(\psi_2) \\
&+ b\,cos(\psi_1) + b\,cos(\psi_2) + b\,cos(\theta_1) + b\,cos(\theta_2) - 4b + x_1 - x_2) - k_r(2\psi_1 - 2\psi_2) \\
&- \frac{k_s}{2}(-2a\,sin(\psi_1) + 2b\,cos(\psi_1))(a\,cos(\phi_1) - a\,cos(\phi_2) + a\,cos(\psi_1) - a\,cos(\psi_2) \\
&+ bsin(\psi_1) + bsin(\psi_2) + y_1 - y_2) - \frac{k_s}{2}(2a\,sin(\psi_1) + 2b\,cos(\psi_1))(-a\,cos(\phi_1) + a\,cos(\phi_2) \\
&- a\,cos(\psi_1) + a\,cos(\psi_2) + bsin(\psi_1) + bsin(\psi_2) + y_1 - y_2)
\end{aligned}$$

D.2 Linearized Joint stiffness matrix

Linearizing all terms in the non-linear joint forcing vector and put them in matrix notation, with the following procedure:

$$\underline{F}_{joint,linear}\left(\underline{u}(t)\right) = -C_{joint}\underline{u}(t) \qquad \text{(Eq. 0.1)}$$

Note: the minus is due to the difference in side (left or right of the equal sign) of the equation where the joint forcing is implemented.

Since the forcing vector is linear, the entries of the stiffness matrix can be composed by taking the derivative with respect to each degree of freedom for every vector input:

$$C_{joint} = \begin{bmatrix} c_{1,1} & \cdots & c_{1,12} \\ \vdots & \ddots & \vdots \\ c_{12,1} & \cdots & c_{12,12} \end{bmatrix} = -1 \cdot \begin{bmatrix} \dfrac{\partial F_1}{\partial u_1} & \cdots & \dfrac{\partial F_1}{\partial u_{12}} \\ \vdots & \ddots & \vdots \\ \dfrac{\partial F_{12}}{\partial u_1} & \cdots & \dfrac{\partial F_{12}}{\partial u_{12}} \end{bmatrix} \qquad \text{(Eq. 0.2)}$$

This leads to the following full diagonal joint stiffness (12x12) matrix with respect to the centers of gravity of floater 1 and 2 for the interconnected floaters.

$$C_{joint} =$$

$$2 \cdot \begin{bmatrix}
k_a & 0 & 0 & 0 & 0 & 0 & -k_a & 0 & 0 & 0 & 0 & 0 \\
0 & k_s & 0 & 0 & 0 & bk_s & 0 & -k_s & 0 & 0 & 0 & bk_s \\
0 & 0 & k_s & 0 & -bk_s & 0 & 0 & 0 & -k_s & 0 & -bk_s & 0 \\
0 & 0 & 0 & a^2 k_s + k_t & 0 & 0 & 0 & 0 & 0 & -a^2 k_s - k_t & 0 & 0 \\
0 & 0 & -bk_s & 0 & b^2 k_s + k_r & 0 & 0 & 0 & bk_s & 0 & b^2 k_s - k_r & 0 \\
0 & bk_s & 0 & 0 & 0 & a^2 k_a + b^2 k_s + k_r & 0 & -bk_s & 0 & 0 & 0 & -a^2 k_a + b^2 k_s - k_r \\
-k_a & 0 & 0 & 0 & 0 & 0 & k_a & 0 & 0 & 0 & 0 & 0 \\
0 & -k_s & 0 & 0 & 0 & -bk_s & 0 & k_s & 0 & 0 & 0 & -bk_s \\
0 & 0 & -k_s & 0 & bk_s & 0 & 0 & 0 & k_s & 0 & bk_s & 0 \\
0 & 0 & 0 & -a^2 k_s - k_t & 0 & 0 & 0 & 0 & 0 & a^2 k_s + k_t & 0 & 0 \\
0 & 0 & -bk_s & 0 & b^2 k_s - k_r & 0 & 0 & 0 & bk_s & 0 & b^2 k_s + k_r & 0 \\
0 & bk_s & 0 & 0 & 0 & -a^2 k_a + b^2 k_s - k_r & 0 & -bk_s & 0 & 0 & 0 & a^2 k_a + b^2 k_s + k_r
\end{bmatrix}$$

E: User Guide NEMOH

NEMOH consists of a collection of Matlab codes, that can be divided into three programs as shown in Figure 0.1.
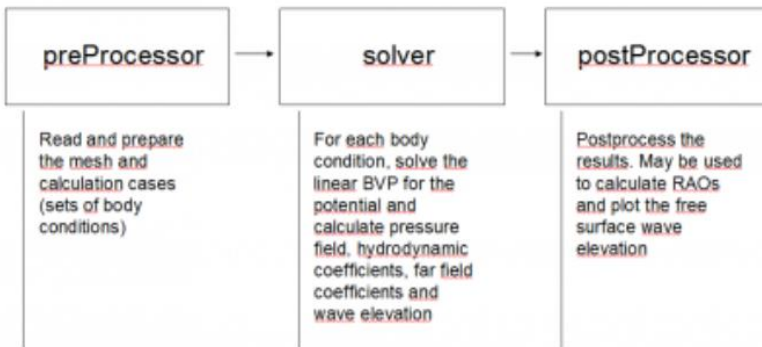

Figure 0.1: Three programmes of which NEMOH is composed.

First the pre-processor is used to create a Mesh. By pre-defining the surfaces of the structure, the mesh code will divide it into a surface consisting of multiple panels. The coordinates of the pre-defined surface should be stated left rotating, when looking from the fluid domain into the body (Babarit & Delhommeau, 2015).
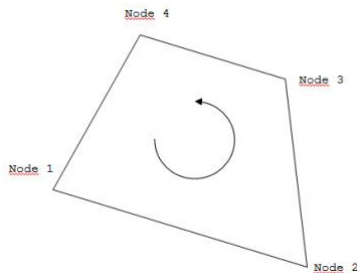
Figure 0.2: orientation convention of a described panel

In the mesh file a symmetry in the xOz-plane is assumed and therefor only half of the body needs to be defined. Automatically the part above the seawater (z=0) is erased and only the under water part is modelled. A mesh of a rectangular box with a certain width (Bf), length (Lf) and draft (T) can be described in the following way:

```
L=Lf/2;      %Only half of the box is modelled
B=Bf/2;

nBodies=1;                                   %number of bodies
n(1)=5;                                      %number of pre-defined panels
%description of panels, with four corner coordinates:
%height above water line taken as one, but does not matter.
X(1,1,:,:)=[-L -B 1.;-L -B -T ;L -B -T ;L -B 1.];
X(1,2,:,:)=[-L 0. 1.;-L -B 1.;L -B 1.;L 0. 1.];
```

```
X(1,3,:,:)=[-L 0. -T;L 0. -T;L -B -T;-L -B -T];
X(1,4,:,:)=[L 0. 1.;L -B 1.;L -B -T;L 0. -T];
X(1,5,:,:)=[-L 0. 1.;-L 0. -T;-L -B -T;-L -B 1.];
%Translation of body in space
tX(1)=0.;
%Center of Gravity for global axis system on water level height
CG(1,:)=[0. 0. KG-T];
%desired number of objects (panels)
nfobj(1)=1000;

[Mass,Inertia,KH,XB,YB,ZB]=Mesh(nBodies,n,X,tX,CG,nfobj)
```

The second step is to let NEMOH calculate the added mass (A), hydrodynamic damping (B) and frequency dependent wave forces (Fe). This is done for a given frequency vector (w) and a wave direction (mu):

```
[A,B,Fe]=NEMOH(w, mu, depth);
```

The mesh generating code automatically generates an ID file with the name of the folder where the mesh is stored. Running NEMOH afterwards this is automatically adapted, and specification of the mesh source is not necessary.

The result of the complex force relates to the incident wave in the following manner (Babarit A. , General Notations and Conventions, 2014):

$$F_{ex}(t) = \Re\big(A\tilde{F}_{ex}(\omega)e^{-i\omega t}\big) = \Re\big(A\big|\tilde{F}_{ex}(\omega)\big|e^{-i(\omega t - \angle\tilde{F}_{ex}(\omega))}\big)$$

E.1 Additional changes in NEMOH code

Multiple wave directions
Changes in NEMOH.m

line 61:

```
textline(n)={sprintf('%g %f %f      ! Number of wave directions, Min and Max
(degrees)',length(dir),dir(1),dir(end))};
```

line 108:116:

```
for i=1:length(dir)
    ligne=fgetl(fid);
    for k=1:nw
        ligne=fscanf(fid,'%f',1+12*nBodies);
        for j=1:6*nBodies
            Famp(i,j,k)=ligne(2*j);
            Fphi(i,j,k)=ligne(2*j+1);
        end;
        ligne=fgetl(fid);
    end;
end;
```

Multiple translations
Change in calling mesh file: `[Mass,Inertia,KH,XB,YB,ZB]=Mesh(nBodies,n,X,tX,tY,CG,nfobj`
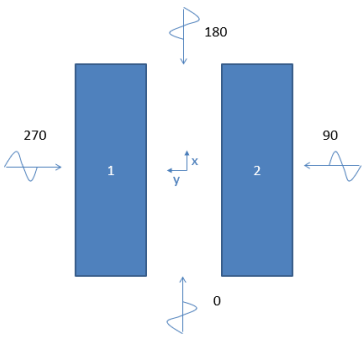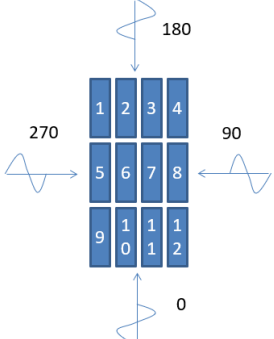
Change line 96 in Mesh.m: `fprintf(fid,'1 \n %f %f \n ',tX(c),tY(c));`

F: Phase shifts in NEMOH & DIFFRAC

Two DIFFRAC files are evaluated, to see how the phase shift is taken into account. In Table 0.1 the two considered systems are shown with the CoG of the two first floaters with respect to the center of each system.

Table 0.1: the reference system of the two considered DIFFRAC files

HydFile 1: 2 bodies		HydFile 2: 12 bodies	
CoG floater 1 [m]	(0 ; 1.455)	CoG floater 1 [m]	(12.598 ; 4.529)
CoG floater 2 [m]	(0 ; -1.455)	CoG floater 2 [m]	(12.598 ; 1.510)
Depth [m]	1000		24

For the convenience the wave direction is kept at 270 degrees ($1.5\pi\ rad$). And from this direction a regular wave is generated, and the phase difference can be computed between the wave arriving at the CoG of body 1 and body 2:

$$\epsilon_{\zeta_{1,2}\zeta_{CoG}} = -kx_{1,2}\cos(1.5\pi) - ky_{1,2}\sin(1.5\pi)$$

$$\epsilon_{\zeta_2\zeta_1} = \epsilon_{\zeta_2\zeta_{CoG}} - \epsilon_{\zeta_1\zeta_{CoG}}$$

To verify this the same is done for the forcing phase shifts obtained for DIFFRAC in the heave motion in the same direction. It is expected that a similar phase difference will arise between these two floating bodies in low frequencies, since the floaters will then "exactly follow the waves".

$$\epsilon_{F_{z2}F_{z1}} = \epsilon_{F_{z2}\zeta} - \epsilon_{F_{z1}\zeta}$$

Table 0.2: comparison for HydFile1: 2 bodies

$\omega\ [rad/s]$	$\lambda\ [m]$	$\epsilon_{\zeta_2\zeta_1}\ [rad]$	$\epsilon_{F_{z2}F_{z1}}\ [rad]$
0.3	685	-0.027	-0.0011
0.5	247	-0.074	-0.0063
1	61.6	-0.30	-0.065
1.5	27.4	-0.67	-0.023

Table 0.3: comparison for HydFile2: 12 bodies: difference between body 1 and 2

$\omega\ [rad/s]$	$\lambda\ [m]$	$\epsilon_{\zeta_2\zeta_1}$	$\epsilon_{F_{z2}F_{z1}}$
0.3	310	-0.061	-0.004
0.5	173	-0.11	-0.010
1	60.8	-0.31	0.076
1.5	27.4	-0.69	0.41

By giving a wave height to the regular wave (H=2.4m in this case), the results can also be plotted. This is done for Steel 12F 1.24 Springs and a frequency of 1 rad/s in Figure 0.1.
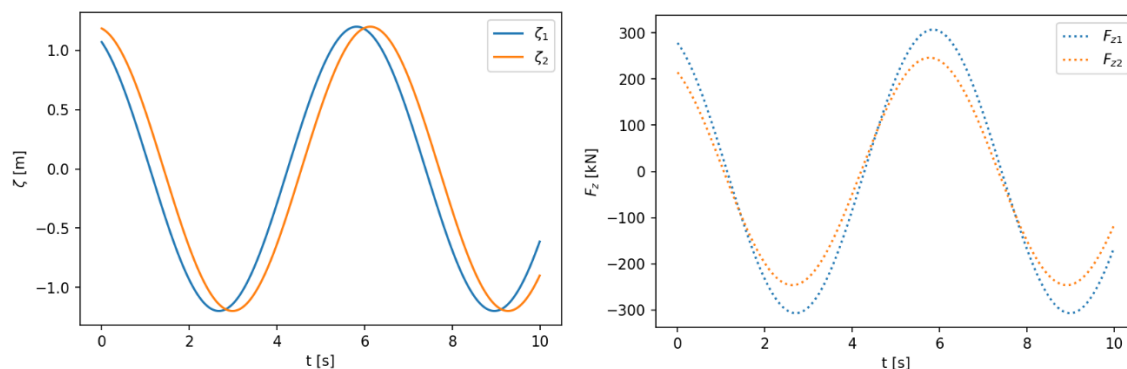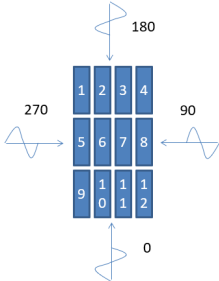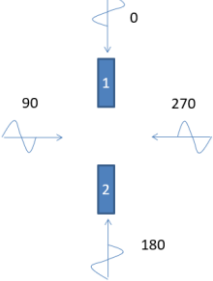

Figure 0.1: wave elevation and heave forcing in floater 1 and 2 for a regular wave in time

It is clearly visible that the phase shifts between the two lines are not similar in both figures. It can be said that DIFFRAC takes not into account the phase shift in the hyd-file and therefor this needs to be

added afterwards for the appropriate location of every body its CoG. It can be seen in Table 0.3 that for higher frequencies (phase shift positive) body 2 even starts to experience forcing earlier than body 1, which is rather a contradiction.

NEMOH seems to take these phase shifts into account properly, with respect to its global coordinate system.

To compare for a larger distance NEMOH and DIFFRAC are compared.

Name	Steel 12F 1.24 Springs		test_CoGdiff_tandem_25.2	
CoG 1	Floater 1	(12.598 ; 4.529)	Floater 1	(0; 0)
CoG 2	Floater 9	(-12.598 ; 4.529)	Floater 2	(25.2 ; 0)
Distance	25.196		25.2	
Depth	24		24	
μ	180		0	

Figure 0.2: Result for DIFFRAC

Figure 0.3: Result for NEMOH

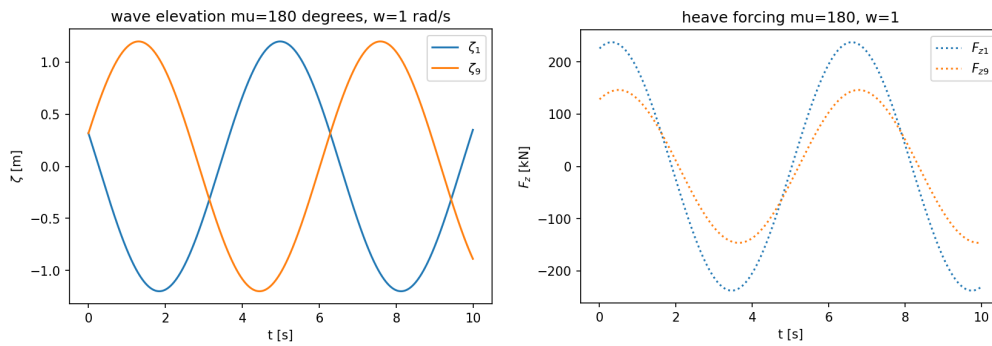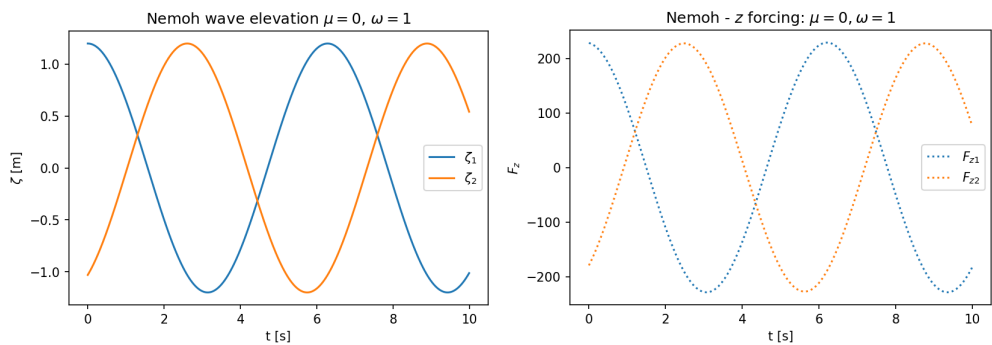The results in Figure 3.6 and Figure 3.7 show clearly that the wave phase difference between the two waves is $\epsilon_{\zeta_1 \zeta_2} = 2.605 \ rad$, when $\zeta = \zeta_a \cos(\omega t - \epsilon_\zeta)$

In NEMOH the Phase shift $F_{eps} = \arg(F_{complex})$ should be used in the following manner:

$$F = \Re\left(F_a e^{-i(\omega t - F_{eps}(\omega))}\right)$$

This will give the correct time shift in time domain. Applying the same to the DIFFRAC file a small phase shift is visible but not realistic for the applied wave $\left(\omega = 1\frac{rad}{s}, \lambda = 60.8 \ m\right)$ leading to the following results:

	DIFFRAC	NEMOH
$\epsilon_{F_{z1}\zeta}$	0.32	-0.07
$\epsilon_{F_{z2}\zeta}$	0.50	2.48
$\epsilon_{F_{z2}F_{z1}}$	0.18	2.56

The two following can be retrieved from a closer study:

- The phase shift in NEMOH has a different sign than the one in DIFFRAC.
- On top of that the DIFFRAC phase shift is with respect to the incident wave at the floaters center of gravity and the one of NEMOH is with respect to the incident wave at the origin of the global coordinate system.

Meaning that:

$$\epsilon_{DIFFRAC,global} = \epsilon_{DIFFRAC}(\omega) - kx_{CoG}\cos(\mu) - ky_{CoG}\sin(\mu)$$

$$\epsilon_{NEMOH} = -\epsilon_{DIFFRAC,global}$$

G: Numerical time integration schemes

G.1 Modified Euler (RK2)

Also known as 2nd order Runge-Kutta, Heun's Method or Predictor-Corrector.

$$\overline{w}_{n+1} = w_n + hf(t_n, w_n)$$
<div style="text-align: right">*(Eq. 0.1)*</div>

$$w_{n+1} = w_n + \frac{h}{2}[f(t_n, w_n) + f(t_{n+1}, \overline{w}_{n+1})]$$

Where:

n	step
w_n	Solution at time step t_n
$\overline{w}_{n+1}$	Predictor of the solution at time t_{n+1}
w_{n+1}	Numerical solution at time t_{n+1}
h	Step size Δt
$f(t, w)$	Approximation function for time derivative

Modified Euler has a local truncation error of $O(h^2)$.

G.2 4th order Runge-Kutta (RK4)

This method combines 4 predictors and has quite attractive stability characteristics. This method has a local truncation error of $O(h^4)$ and can therefor lead to higher accuracies of the time integration and increases the stability region. Nevertheless, the expected increase in time step size compared to Modified Euler is very small and is not of practical use (Vuik, van Beek, Vermolen, & van Kan, 2006).

$$w_{n+1} = w_n + \frac{1}{6}[k_1 + 2k_2 + 2k_3 + k_4]$$
<div style="text-align: right">*(Eq. 0.2)*</div>

$$k_1 = hf(t_n, w_n)$$

$$k_2 = hf\left(t_n + \frac{1}{2}h, w_n + \frac{1}{2}k_1\right)$$

$$k_3 = hf\left(t_n + \frac{1}{2}h, w_n + \frac{1}{2}k_2\right)$$

$$k_4 = hf(t_n + h, w_n + k_3)$$

G.3 ODE45-solver

Different programming languages have numerical time integration packages. A widely used numerical integration scheme in these packages is the ODE45-solver. A mix of an explicit RK4 and RK5 method with variable time stepping to increase the stability of the integration scheme. In Python the package is due to Dormand & Prince (The SciPy community, 2019) and a more detailed description can be found in (Hairer, Norsett, & Wanner, 1993).

G.4 Solving EoM

As an input for the time integration scheme the EoM needs to be solved at the particular time step indicated in the function $f(t_n, w_n)$ (see for example equation 8.2), where w_n contains all the displacements and velocities at this time step. A short intermezzo is given for solving this for a SDoF- and a MDoF-system.

SDoF – system

As an example the predictor function presented in equation 0.1 is solved. For convenience the EoM is described with a damping factor b (which is not the correct representation of the Cummins' equation, but will do as an example).

$$m\,\ddot{x}_n + b\dot{x}_n + cx_n = F_n \qquad (Eq.\ 0.3)$$

For a single degree of freedom: $w_n = \begin{bmatrix} x_n \\ \dot{x}_n \end{bmatrix}$.

Solving the equation of motion will return $f(t_n, w_n) = \begin{bmatrix} \dot{x}_n \\ \ddot{x}_n \end{bmatrix}$

The function $f(t_n, w_n)$ can therefore be written as:

$$f(t_n, w_n) = f\left(t_n, \begin{bmatrix} x_n \\ \dot{x}_n \end{bmatrix}\right) = \begin{bmatrix} \dot{x}_n \\ \ddot{x}_n \end{bmatrix} = \begin{bmatrix} \dot{x}_n \\ \dfrac{1}{m}(F_n - b\dot{x}_n - cx_n) \end{bmatrix} \qquad (Eq.\ 0.4)$$

It can now be seen that the function 8.2 can be rewritten in the following form:

$$\bar{w}_{n+1} = w_n + hf(t_n, w_n) = \begin{bmatrix} x_n \\ \dot{x}_n \end{bmatrix} + h\begin{bmatrix} \dot{x}_n \\ \dfrac{1}{m}(F_n - b\dot{x}_n - cx_n) \end{bmatrix} \qquad (Eq.\ 0.5)$$

MDoF – system

The same procedure can be performed for a MDoF:

$$M\ddot{u}_n + B\dot{u}_n + Cu_n = \bar{F}_n \qquad (Eq.\ 0.6)$$

The w will become a (2xnDoF) vector containing all the velocities and accelerations: $w_n = \begin{bmatrix} u_n \\ \dot{u}_n \end{bmatrix}$. Since the system is written in matrix notation, the solution to the predictor formula becomes:

$$\bar{w}_{n+1} = w_n + hf(t_n, w_n) = \begin{bmatrix} u_n \\ \dot{u}_n \end{bmatrix} + h\begin{bmatrix} \dot{u}_n \\ M^{-1}(\bar{F}_n - B\dot{u}_n - Cu_n) \end{bmatrix} \qquad (Eq.\ 0.7)$$

H: Retardation Function

The retardation function:

$$R_{ij}(\tau) = \frac{2}{\pi} \int_0^\infty b_{ij}(\omega) \cos(\omega\tau)\, d\omega$$

In numerical form approximated by:

$$R_{ij}(\tau) = \sum_{k=1}^N b_{ij}(\omega_k) \cos(\omega_k \tau)\, \Delta\omega$$

Next to the hydrodynamic damping in frequency domain, two important factors are of influence on the outcome of the retardation function:

- The frequency range
- The Retardation time

H.1 Frequency range

In order to capture all the 'damping' in the retardation, the hydrodynamic damping coefficient in frequency domain should decay towards zero at high frequencies. Otherwise this is a sign that not all the damping is captured in the impulse response (retardation function).

The difference in retardation function is shown for different frequency ranges.
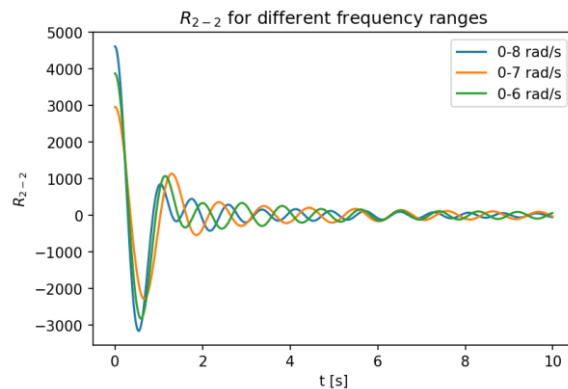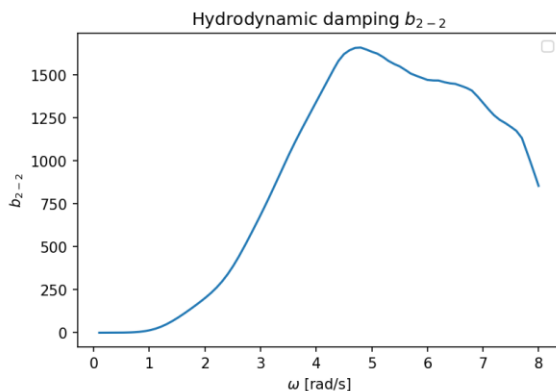
Figure 0.1: Hydrodynamic damping in frequency domain for sway and heave (left), the resulting Retardation function for different frequency ranges considered (right).

Figure 0.1 shows that the frequency range can be of major importance on the retardation function. Especially for damping coefficients that have not decayed to zero at the end of the considered frequency range (this is the case for surge at 6 and 7 rad/s). The heave retardat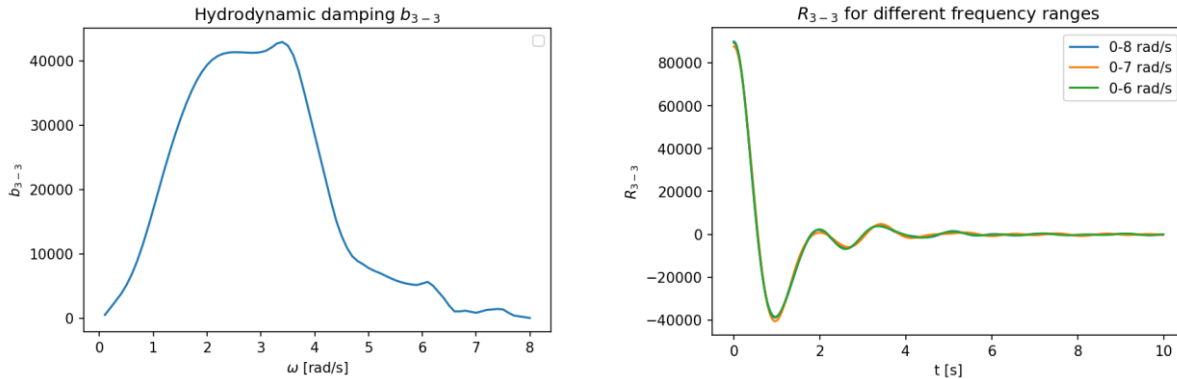ion function shows not these large differences, since the hydrodynamic damping approaches zero faster for higher frequencies.

H.2 Retardation time

Another factor of influence is for how many seconds the retardation function is evaluated in the model. Since the Retardation function is a decaying function, there is no need to evaluate it for the total desired time output. It can therefor be shortened for a certain number of seconds that is used in the convolution with the same amount of time steps of the velocity.

Studying every Retardation function (12x12 for two floaters) shows that all retardation functions have decayed to approximately zero after 10-20 seconds.

In order to do the convolution of the whole retardation function and the velocity, the model needs some 'startup time', which means that the convolution cannot be evaluated completely until the time is past the retardation time given up.

By plotting the result of the two interconnected floater model after sufficient time shows the following for different retardation time, see Figure 0.2. Only some difference can be observed for very small retardation time.
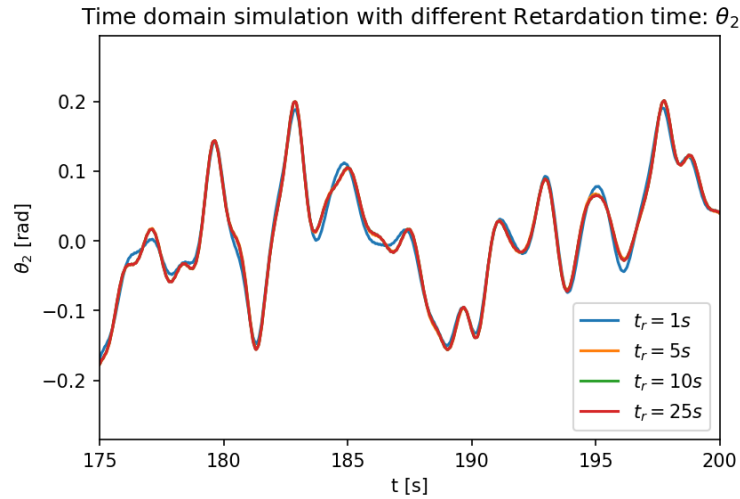
Figure 0.2: Result of two interconnected floaters for different retardation time

H.3 Conclusion

It can be concluded that for a proper implementation of the Retardation function the frequency range should be wide enough for the hydrodynamic damping to become zero at higher frequencies. This is at approximately 8 rad/s for the floaters considered in this study. The retardation time can be shortened due to the fast decay to zero of the retardation function. This is taken as 25 seconds in this research.

I: Added Mass at infinite frequency

In this appendix the determination of added mass at infinite frequency is evaluated. Two methods are compared:

- the determination of the added mass at infinite frequency with the frequency dependent added mass by averaging the formula presented in section 2.3.5, (Babarit & Delhommeau, Theoretical and numerical aspects of the open source BEM solver NEMOH, 2015).

  - $a_{ij,\infty} = \overline{a_{ij,\infty}(\omega) + \frac{1}{\omega}\int_0^\infty R_{ij}(\tau)\sin(\omega\tau)\,d\tau}$

  $$\rightarrow a_{ij,\infty} = \frac{1}{n_\omega}\sum_{n=1}^{N_\omega}\left(a_{ij}(\omega_n) + \frac{1}{\omega_n}\sum_{k=0}^{N_t}R_{ij,k}\sin(\omega_n t_k)\,\Delta t\right)$$

- Let NEMOH Calculate the added mass at higher frequencies and analyze its convergence.
- Developed formulas for added mass calculation

I.1 Averaging

The first method stated can be obtained with the frequency dependent added mass and hydrodynamic damping. The retardation function follows from the hydrodynamic damping, see section 2.3.5.

For two floaters in heave and pitch this results in the following added mass matrix (including gap resonance suppression, see Appendix K):

$$A_\infty = 10^3 \cdot \begin{bmatrix} 29.2 & -0.81 & 7.63 & 1.85 \\ -0.84 & 4.48 & -1.87 & -0.54 \\ 7.63 & -1.85 & 29.2 & 0.81 \\ 1.87 & -0.54 & 0.84 & 4.48 \end{bmatrix}$$

A similar method is presented in the aNySIM theory documentation (MARIN, 2018) as being:

$$a_{ij,\infty} = a_{ij}(\omega) + \frac{1}{\omega}\int_0^{\frac{\pi}{\Delta\omega}} R_{ij}(\tau)\sin(\omega\tau)\,d\tau$$

For a frequency step size of $\Delta\omega = 0.01\ rad/s$ (see section 3.3.2), the Retardation function should at least be evaluated until 315 seconds to full fill the calculation of the integral. The result for the calculation of the heave added mass is shown in Figure 0.1 at the different frequencies.
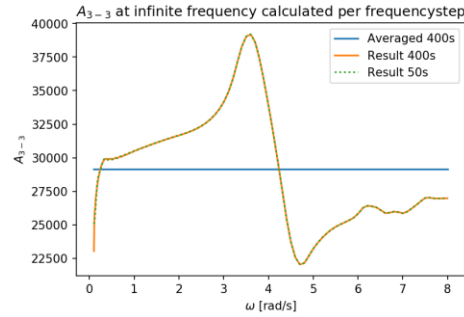
Figure 0.1: Result for calculation of infinite added mass at different frequencies and different Retardation time

The result shows that it is in this case not of influence if the retardation time is calculated for 50 seconds or more then the stated 315 seconds. This due to the fast decay of the retardation function, see Appendix H.

I.2 Higher frequencies

In order to estimate the added mass at higher frequencies properly, also the mesh needs to be adjusted to be able to capture high frequency waves/short wave lengths. There should be sufficient panels per wave length.

As a rule of thumb the minimum required number of panels (William Otto, Marin 2018) should be at least 5 per occurring wavelength. Knowing the wetted surface area an estimation can be made of the number of panels required per wave frequency that is calculated.

The wave length corresponds to the wave frequency via the dispersion relation and can be calculated iteratively:

$$\lambda = \frac{g}{2\pi} T^2 \tanh\left(2\pi \frac{h}{\lambda}\right)$$

The minimum number of panels on the floater that are at least required per wave length can then be calculated accordingly:

$$N_{panels} = \frac{A_{wetted}}{\left(\frac{\lambda}{5}\right)^2}$$

The result is summed up in the following table:

Table 0.1: Estimation of the amount of panels minimal required in mesh for higher frequencies

$\omega\ [rad/s]$	$\lambda\ [m]$	N_{panels}
8	0.96	903
10	0.62	2204
25	0.10	86108
50	0.024	1,377,739

This means that the calculation of higher frequencies would be very time intensive and is proceeded here.

I.3 Developed formulas

Different methods have been presented to approximate the added mass at infinite frequency and for heave motion they were summarized by (Koo & Kim, 2015).

For a rectangular barge the following table can be applied:

Table 0.2: Heave added mass for various B/T at high (infinite) frequency in deep water (h/T=30) *(Koo & Kim, 2015).*

Rectangle	
B/T	$a_{33} / \rho A$
2	1.120081
3	1.032703
4	0.969387
5	0.919991
6	0.880204
7	0.847645
8	0.820776
9	0.798465
10	0.779873

Applying the dimensions of the structure would implicate an added mass for heave of $a_{33} = 21.8\ kN/(m/s^2)$, which is slightly lower than the ones stated above.

I.4 Influence of Added Mass

Two different cases of the added mass are considered to verify its influence on the total. The averaged value and a decreased value of the averaged added mass of 75%: $A_{\infty,75} = 0.75 \cdot A_\infty$, to study the change in behavior due to this added mass. Again, this has large influence on the rotational motions of two interconnected floaters, see Figure 0.2.
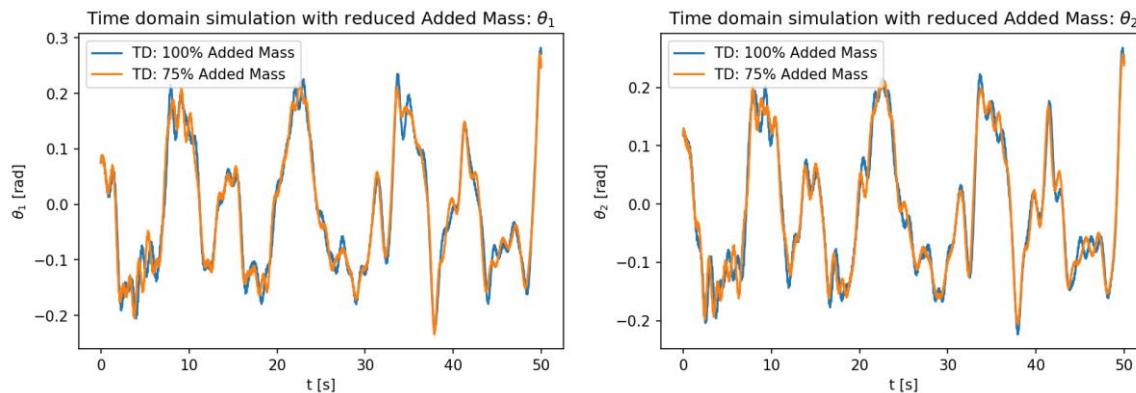
Figure 0.2: Influence of a reduction of Added Mass on the pitch behaviour of two interconnected floaters

It can clearly be seen that not only on the amplitudes, but also on the phase of the motions it has influence, and an inaccuracy in the infinite added mass has influence on the overall behavior.

I.5 Conclusion

The formula given by (Koo & Kim, 2015) gives a lower value than the added mass with the averaging function (29.2 $vs.$ 21.8 $kN/(m/s^2)$). Nevertheless, for multiple bodies, it is more convenient to stick to the method presented by (Babarit & Delhommeau, Theoretical and numerical aspects of the open source BEM solver NEMOH, 2015) to calculate the added mass.

It is shown that inaccuracies in the infinite added mass, can have significant influence on the response of the floater.

J: Exact Solution in TD

This appendix describes the exact solution for a single mass-spring dashpot system.

The exact solution to the following system, where F is an arbitrary force:

$$(m + a_\infty)\ddot{u} + b\dot{u} + cu = F \leftrightarrow \ddot{u} + 2\zeta\omega_0\dot{u} + \omega_0^2 u = F/(m + a_\infty)$$

<div align="right">(Eq. 0.1)</div>

And can be divided in a homogeneous and particular part:

$$u(t) = u_{hom}(t) + u_{part}(t)$$

<div align="right">(Eq. 0.2)</div>

The general solution to a sub-critically damped system is:

$$u_{hom}(t) = \exp(-\zeta\omega_0 t)\left(C_1 cos(\omega_1 t) + C_2 sin(\omega_1 t)\right)$$

<div align="right">(Eq. 0.3)</div>

The arbitrary force $F(t)$ can be expressed as a convolution integral (different than the one mentioned before): $F(t) = \int_0^\infty F_u(\tilde{t})\delta(t - \tilde{t})d\tilde{t}$. The particular solution to this is the Duhamel's integral for damped systems:

<div align="right">(Eq. 0.4)</div>

$$u_{part}(t) = \frac{1}{(m + a_\infty)\omega_1}\int_0^t F_u(\tilde{t})\exp\left(-\zeta\omega_0(t - \tilde{t})\right)\sin\left(\omega_1(t - \tilde{t})\right)d\tilde{t}$$

Solving for the initial conditions (u_0, v_0), gives the following expression for the 1DoF motion:

<div align="right">(Eq. 0.5)</div>

$$u(t) = \exp(-\zeta\omega_0 t)\left(u_0 cos(\omega_1 t) + \frac{1}{\omega_1}(v_0 + u_0\zeta\omega_0)sin(\omega_1 t)\right)$$

$$+ \frac{1}{(m + a_\infty)\omega_1}\int_0^t F_u(\tilde{t})\exp\left(-\zeta\omega_0(t - \tilde{t})\right)\sin\left(\omega_1(t - \tilde{t})\right)d\tilde{t}$$

K: Gap Resonance Interpolation

Two floaters are modelled up to 8 rad/s in NEMOH (2 floaters with gap of 0.3m) to obtain the hydrodynamic coefficients (Added mass, hydrodynamic damping and first order wave forces). A comparison is made with the diagonal hydrodynamic coefficients of a single floater in Figure 0.1. The result shows that the locations of the gap resonance are clearly visible.

In Figure 0.1 can be seen that the gap resonance causes significant influence. Even negative diagonal terms are found in the matrices, which is not desirable. This is observed for the added mass in every direction, except sway (A_{22}).
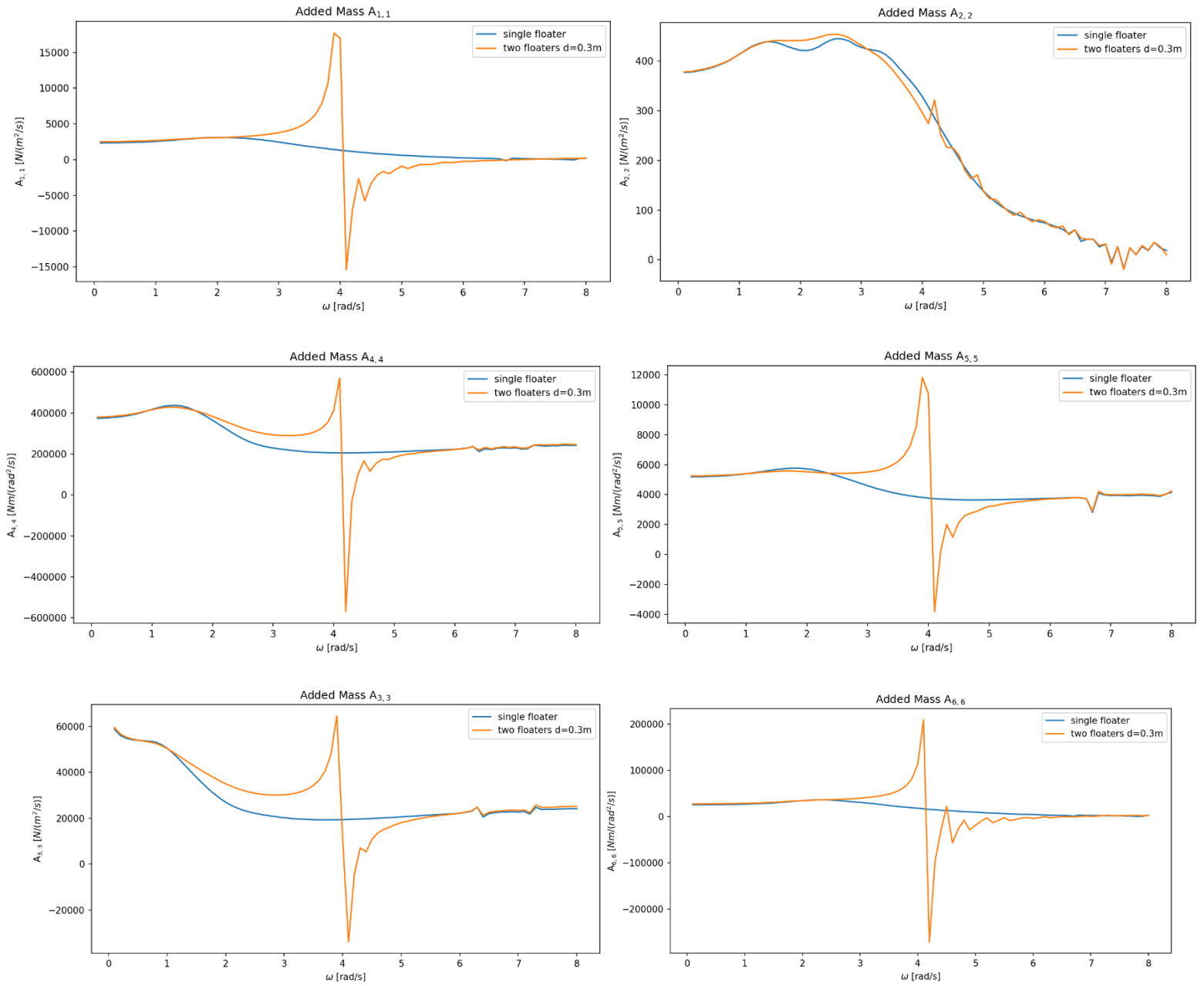
Figure 0.1: Diagonal Added Mass terms of single floater and first floater of a two-floater model
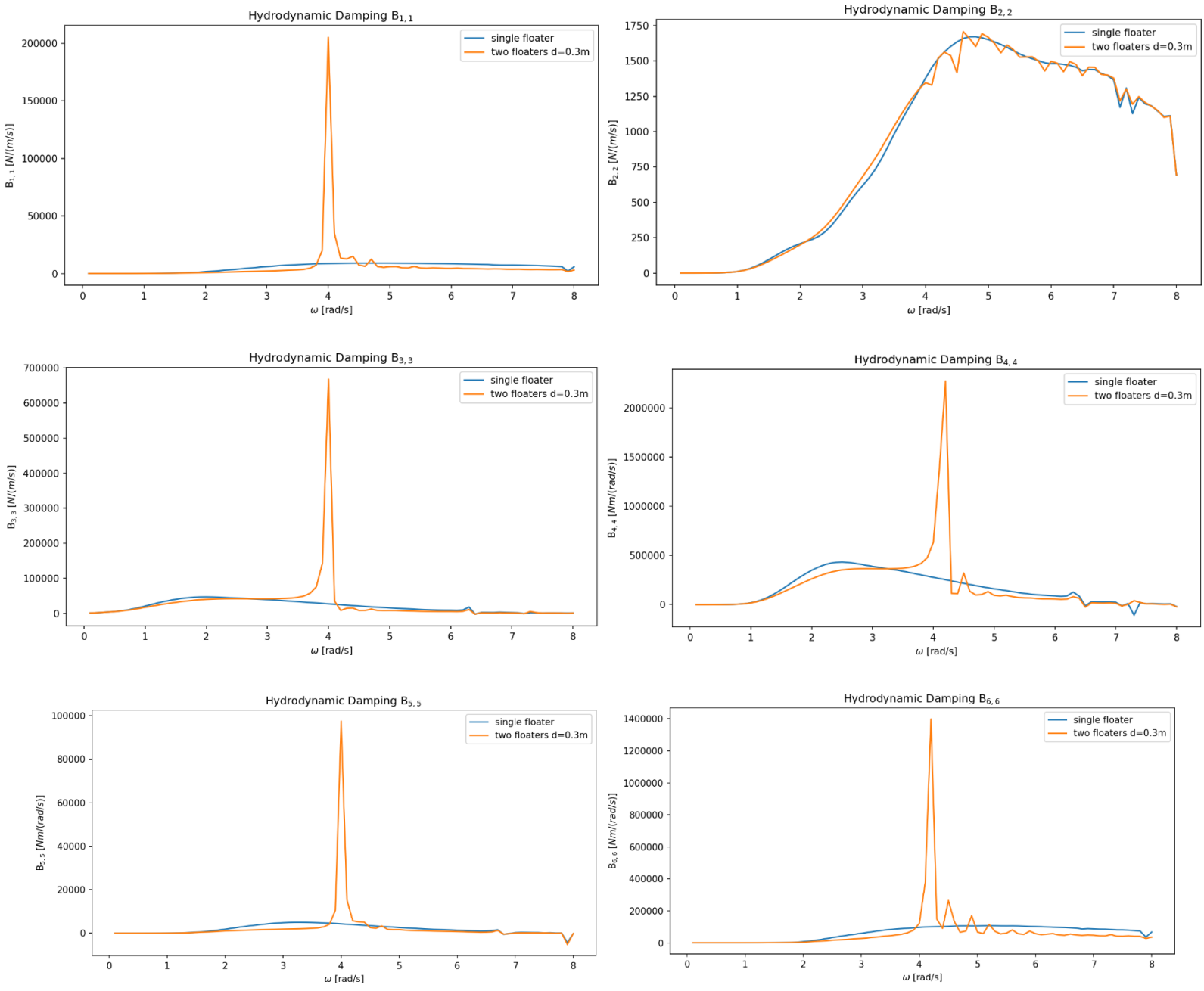
Figure 0.2: Diagonal Hydrodynamic Damping terms of single floater and first floater of a two-floater model
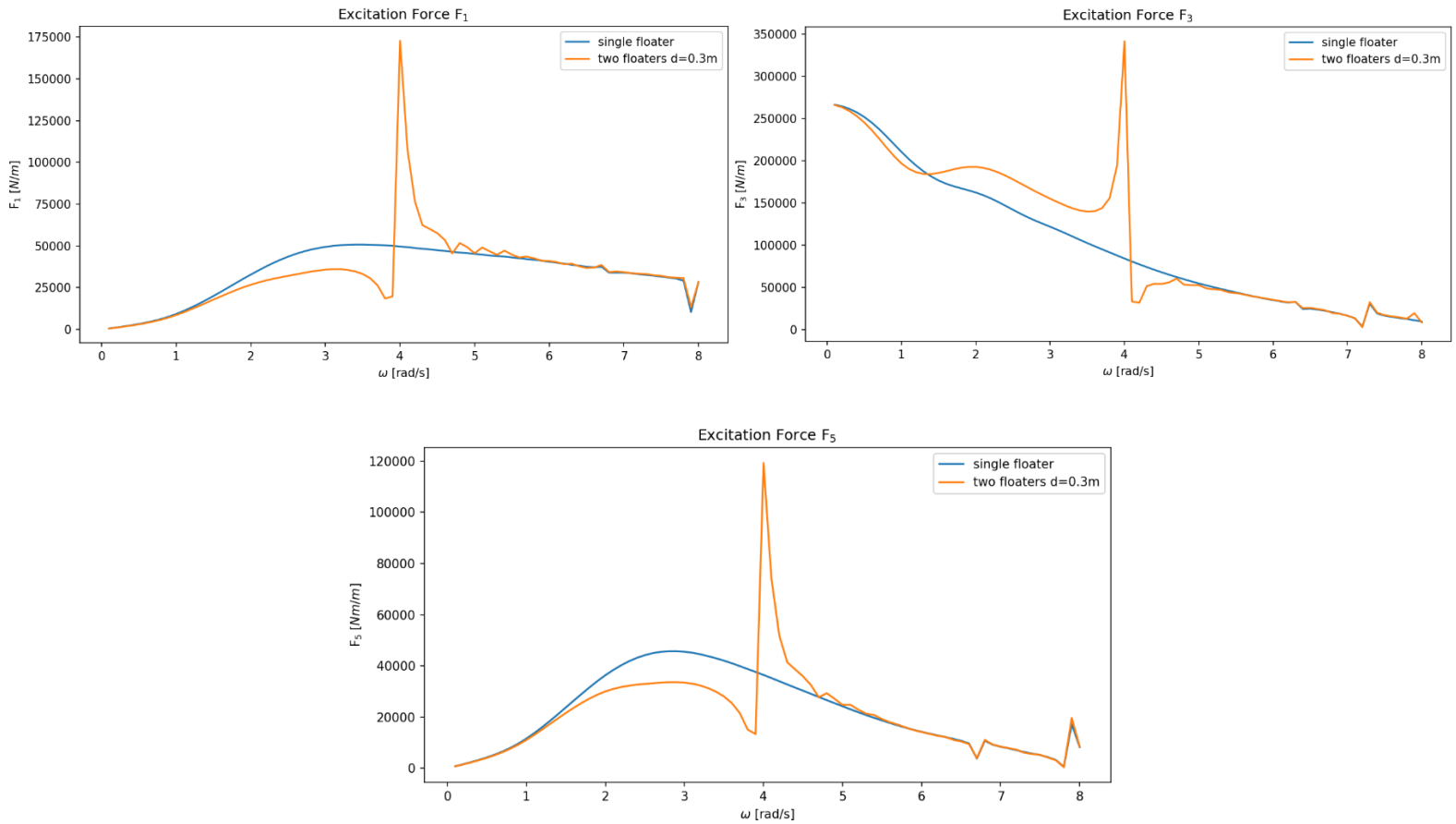
Figure 0.3: Force amplitude response under head waves ($\mu = 0°$) of a single floater and first floater of a two-floater model

Implementing a linear interpolation around the gap resonant frequency part, that is cut out, is applied. As stated in chapter 5, the first calculated gap resonant frequency based on Molin's formula is: $\omega_{gap} \approx 3.82\ rad/s$. Visually it can be seen that it is indeed around $4\ rad/s$. Since there are multiple coefficients that need to be adjusted for (namely for two floaters: 12x12 Added Mass, 12x12 Hydrodynamic damping, 12x(number of wave directions) wave forcing), the range that is cut out needs to be chosen correctly. Three different ranges have been applied to the coefficients; Cut out and interpolate between: 3.9-4.2 rad/s, 3.5-4.5 rad/s and 3.0-5.0 rad/s. On every coefficient the optimal range can differ as can be seen in figure Figure 0.4 for the proposed interpolations of $B_{2,2}$ and F_1 ($\mu = 0°$).
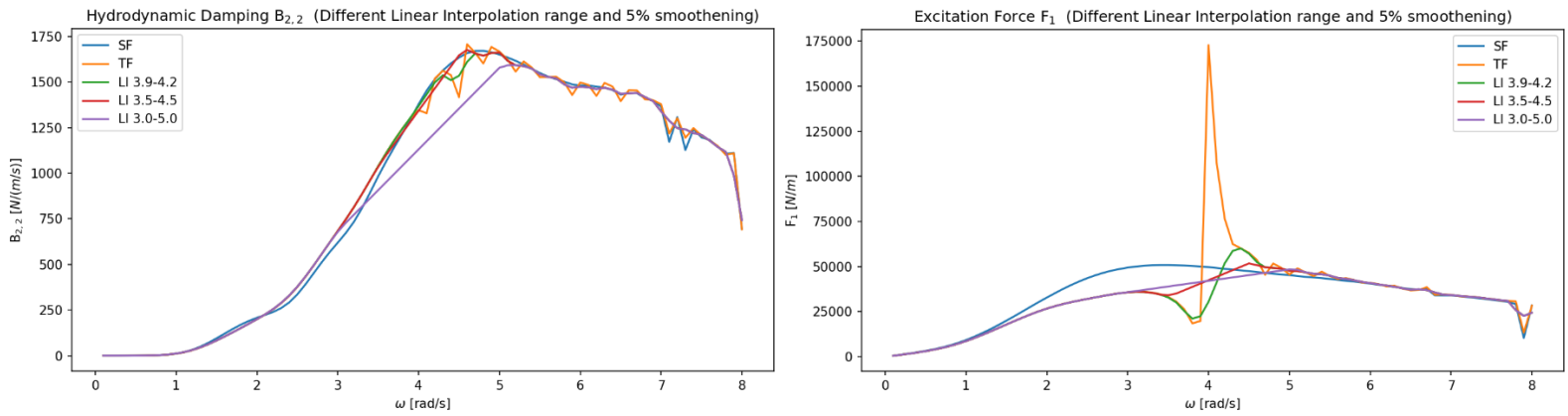
Figure 0.4: Linear interpolation for different ranges for Hydrodynamic Damping in sway-sway (left) and Wave force amplitude response in surge under head waves (right).

While the cut-out range of 3.0-5.0 rad/s would give the most smooth result for the forcing in this case (Figure 0.4right), it is obviously that this is not the case for the hydrodynamic damping in sway-sway motion. A good range to suppress the first gap-resonant peak is at 3.5-4.5 rad/s, for all coefficients in this case and applied accordingly.

K.1 Smoothening

In order to overcome sharp discontinuities at higher resonant frequencies and at the cut-out boundaries a smoothening can be applied. This averages the values of a certain fraction of the result. See Figure 0.5 for different smoothening fractions S.
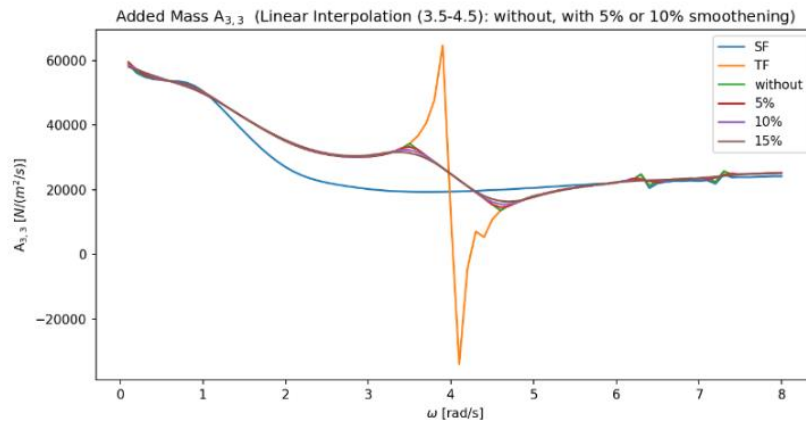
Figure 0.5: Linear interpolation of Added Mass in Heave-Heave of the first floater (in a two-floater-configuration) for different smoothening fractions.

In all cases 10% smoothening gives convenient results, to get out the peaks at resonant frequencies, without changing the overall shape of the hydrodynamic coefficients.

K.2 Force interpolation

Keeping in mind that the first order wave force is composed of a force amplitude response $\left(\frac{F_{a,i}}{\zeta_a}\right)$ and a phase shift $\epsilon_{F_i\zeta}$. Interpolating this properly is by interpolating the real and imaginary part of the combined complex wave force response function:

$$\Re\left(\frac{F_{a,i}}{\zeta_a}(\omega)e^{i\epsilon_{F_i\zeta}(\omega)}\right) \text{ and } \Im\left(\frac{F_{a,i}}{\zeta_a}(\omega)e^{i\epsilon_{F_i\zeta}(\omega)}\right)$$

The interpolation on the phase shift goes properly as can be seen in Figure 0.6.

Figure 0.6: Unprocessed (old) and Interpolated/smoothened (new) force amplitude response (left) and force phase shift (right) under head waves ($\mu = 0°$) of the first floater of a two-floater model.

126

K.3 Sensitivity

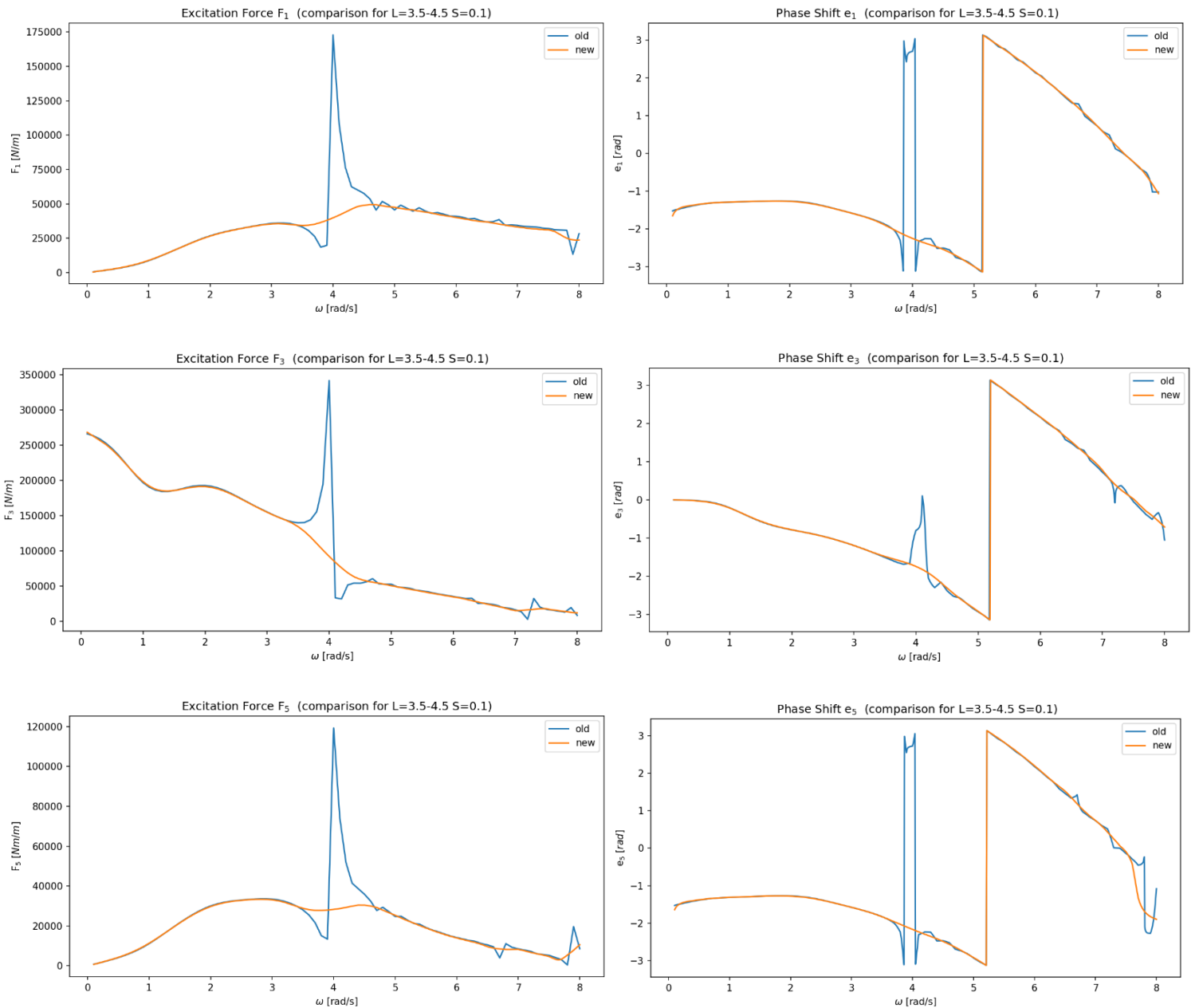It can be checked what the sensitivity is of the model to these changes in suppressing the gap resonance. This is performed for two floaters with heave and pitch motion under head waves. As a reference also the motion is plotted for cutting of all the frequencies above 3 rad/s (in this case there is no influence of gap resonance at all, but there will be information lost as well at higher frequencies).

Going back to the equation of motion stated in in section 2.2.2, a change in these hydrodynamic coefficients has the biggest influence on the wave forcing and the retardation function in the time domain model.

The amplitude of the retardation function increases significantly when the hydrodynamic damping is not suppressed at its resonant frequencies (Figure 0.7), and even can change sign (Figure 0.8), due to a large negative peak at the gap resonance. An additional gain of the suppression is that the retardation time can be shorter in the time domain model, due to its faster convergence to zero, see Figure 0.7.
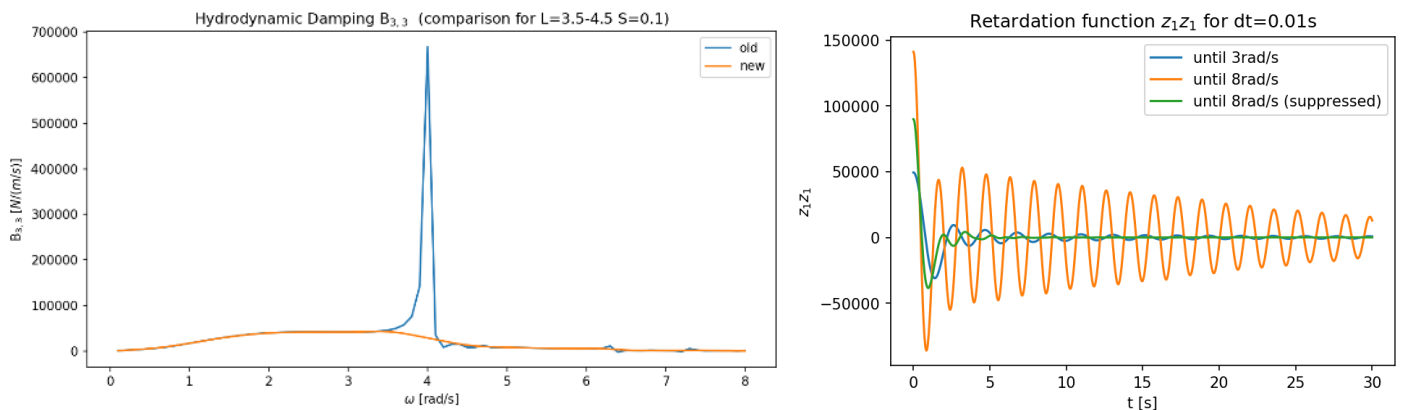
Figure 0.7: Unprocessed (old) and Interpolated/smoothened (new) Hydrod. damping of the first floater of a two-floater model in heave-heave (left). The result of the calculation of the retardation function in heave-heave (right).
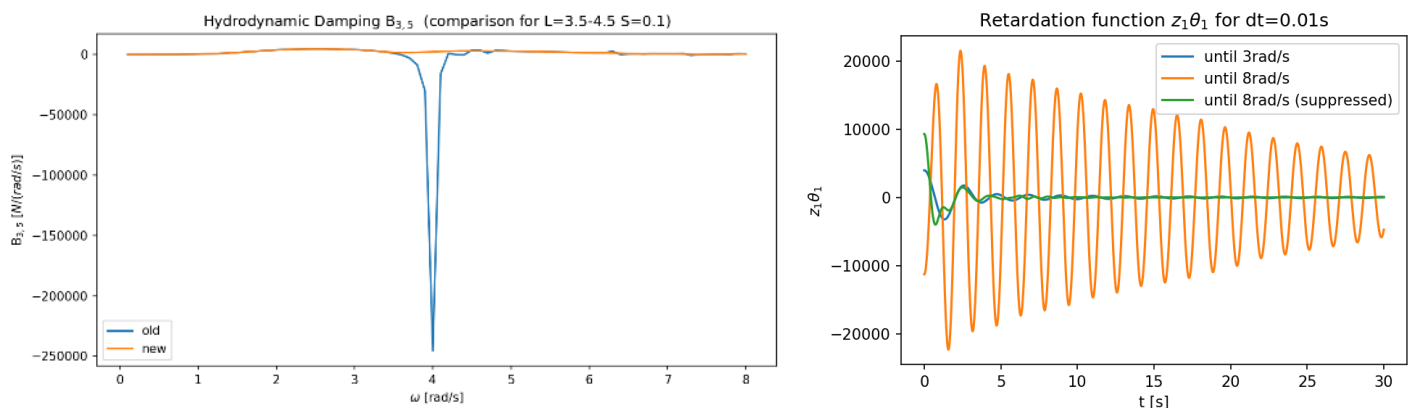
Figure 0.8: Unprocessed (old) and Interpolated/smoothened (new) Hydrod. damping of the first floater of a two-floater model in heave-pitch (left). The result of the calculation of the retardation function in heave-pitch (right).

The calculated wave forcing in the system for the three cases, is evaluated by means of superposition and shown in Figure 0.9. As described before, it can clearly be seen that the force in pitch, is most

sensitive to the changes at these higher frequencies, where the unsuppressed gives the highest fluctuations for high frequencies, due to the resonant peak.
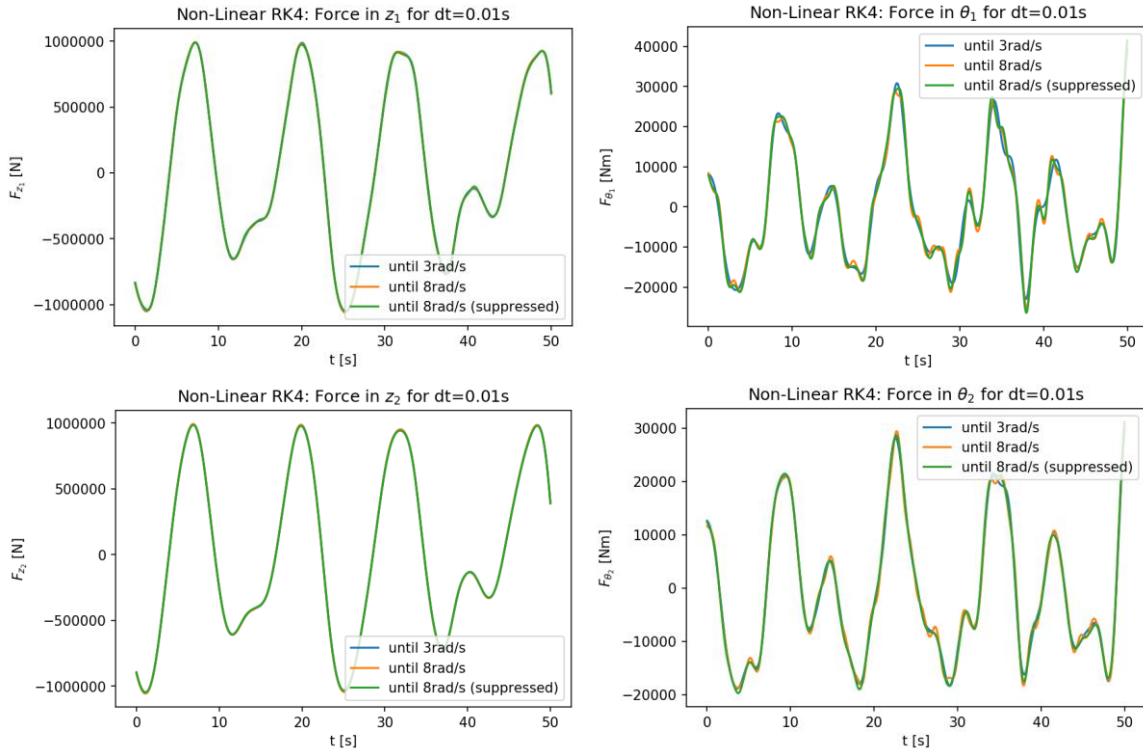
Figure 0.9: Forcing in the four degrees of freedom for two floaters under head waves for heave and pitch. Wave-state: ULS.

The results of the time domain model are shown in Figure 0.10. It can be observed that especially the pitch is very sensitive to these changes. This is mainly because is overall more sensitive for higher wave frequencies. Short waves on the platform are more likely to cause pitching motions on the relatively small floaters. Longer waves on the other hand are more of influence on the heaving motion.
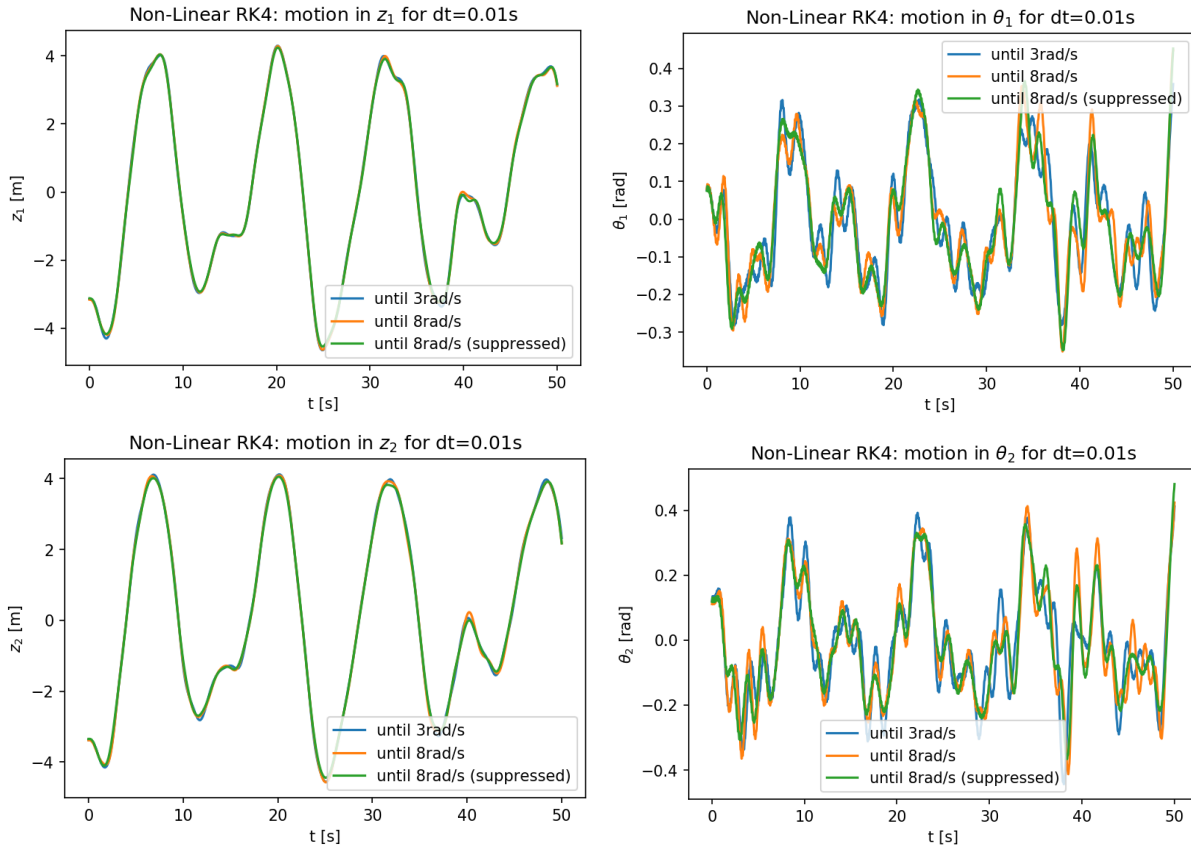
Figure 0.10: Motion in the four degrees of freedom for two floaters under head waves for heave and pitch. Wave-state: ULS.

Keeping the retardation time low in a system that is not suppressed, so the retardation function has not decayed yet completely. The system tends to become unstable when the resonant frequencies are not suppressed. See Figure 0.11.
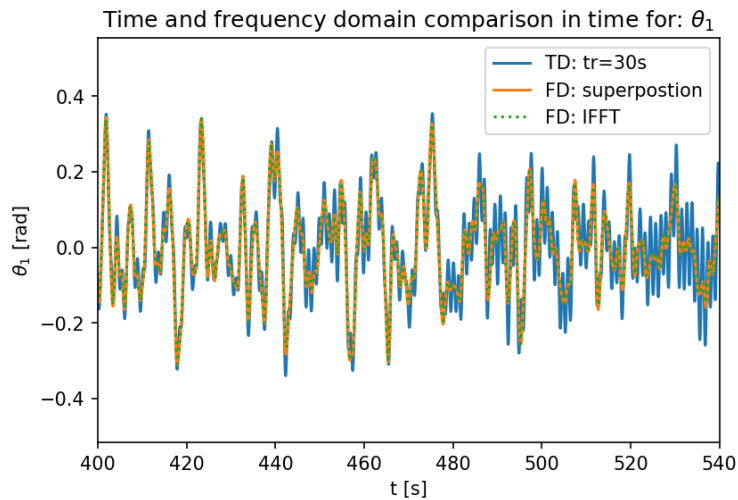
Figure 0.11: Time domain becoming unstable, when retardation time is not sufficient, unsuppressed situation shown.

K.4 Conclusion

A straightforward way of suppressing the gap resonance is cutting out the part around the gap resonance (3.5-4.5 rad/s) and linearly interpolate this. The range that is cut-out needs to be chosen carefully, so that this method is valid for all hydrodynamic coefficients. A 10% smoothening of the results flattens the discontinuities at higher resonant frequencies and at the cut-out boundaries.

The procedure has beneficial effects on the retardation time that needs to be considered in the time domain model, since the retardation function of the suppressed hydrodynamic damping decays faster to zero.

L: Joint stiffness determination

The joint is described as springs (see: 2.4.1 Joints as springs) and for optimal result of the model it is more desired to give realistic values to the spring. As a reference a 'fictive' but realistic rubber ring-shaped fender is used. Not considering if this could bear the forces and the yield stressed.

Spring stiffnesses

In order to get an approximation of the stiffness of the joints, it is assumed that it will have a round shape, like a fender. In the middle space is required for cabling between the various platforms. The second moment of area therefor will become:
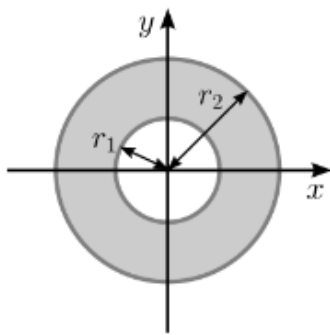
$$I_x = I_y = \frac{\pi}{4}(r_2^4 - r_1^4)$$
$$I_p = I_x + I_y = \frac{\pi}{2}(r_2^4 - r_1^4)$$
$$A = \pi(r_2^2 - r_1^2)$$

Where:
A = crossectional area
$I_{x,y}$ = second moment of area
I_p = the polar moment of inertia

Figure 0.1: Crossection of a circular joint and its characteristics

The spring stiffnesses can be determined accordingly:

- Axial stiffness: $\quad k_a = \frac{EA}{l}$ $\hfill$ *(Eq. 0.1)*

- Shear stiffness: $\quad k_s = \frac{12EI}{l^3}$ $\hfill$ *(Eq. 0.2)*

- Bending stiffness: $\quad k_r = \frac{EI}{l}$ $\hfill$ *(Eq. 0.3)*

- Torsional stiffness: $\quad k_t = \frac{GI_p}{l}, \; G = \frac{E}{2(1+v)}$ $\hfill$ *(Eq. 0.4)*

Where:

$\quad E \quad$ Young's modulus [N/m²]

$\quad G \quad$ Shear modulus [N/m²]

$\quad v \quad$ Poisson ratio

l Length of joint [m]

Summarizing the above calculations gives the initial implemented joint for the calculations:

Table 0.1: Initial characteristics for and resultant joint stiffness

material	Rubber
r_2	-
r_1	-
$I_{x,y}$	-
I_p	-
A	-
E	-
ν	-
G	-
l	-
k_a	$2221\ kN/m$
k_s	$1629\ kN/m$
k_r	$12\ kNm/rad$
k_t	$8\quad kNm/rad$

M: Reaction force and Stress

M.1 Reaction forcing in joint

When the model calculates the motions of the interconnected floaters, also the reaction forces at the connection points can be calculated afterwards with the relative displacements of the connection points. The relative displacement of each connection point can be calculated with the floater's motions and the rotation matrices as presented in section 0 and 0.

$$\underline{F}_{local} = \Delta\underline{u}_{joint}\underline{k}^T + \Delta\underline{\dot{u}}_{joint}\underline{d}^T \qquad \text{(Eq. 0.1)}$$

Where: $\Delta\underline{u}_{joint} = \left[\Delta x_{joint}, \Delta y_{joint}, \Delta z_{joint}, \Delta\phi_{joint}, \Delta\theta_{joint}, \Delta\psi_{joint}\right]^T, \underline{k} = [k_a, k_s, k_s, k_t, k_r, k_r]^T, \underline{d} = [d_a, d_s, d_s, d_t, d_r, d_r]^T$

$\underline{F}_{local} = $ local force/moment in joint in all directions. All as a function of time.

$$\Delta\underline{u}_{joint} = \underline{u}_{P1} - \underline{u}_{P2}$$

$$\underline{u}_{P_i} = \begin{bmatrix} x_i + x_{P,\theta_i} + x_{P,\psi_i} \\ y_i + y_{P,\phi_i} + y_{P,\psi_i} \\ z_i + z_{P,\phi_i} + z_{P,\theta_i} \\ \phi_i \\ \theta_i \\ \psi_i \end{bmatrix}$$

This will result in non-linear equations for the acting reaction forces. For frequency domain or linear time domain calculations these need to be linearized, to derive the appropriate reaction forces that were acting in the used model.

M.2 Stress calculation

The reacting shear stress in the joint at the connection point can be calculated by combining the local transversal forces (in local y and z direction) and torsional moment (in local ϕ). The reacting compressive and tensional stress can be calculated by the local axial force (in local x) and bending moments (in local θ and ψ).

The combined forces in the connection:

$$F_{axial} = F_{local,x} \qquad \text{(Eq. 0.2)}$$

$$F_{transversal} = \sqrt{F_{local,y}^2 + F_{local,z}^2} \qquad \text{(Eq. 0.3)}$$

$$M_{bending} = \sqrt{F_{local,\theta}^2 + F_{local,\psi}^2}$$

$$M_{torsion} = F_{local,\phi}$$

The maximum material stresses will be on the outer surface of the cross-section and can be composed out of the following:

Axial and bending stress: $\sigma_{axial} = \frac{F_{axial}}{A}$, $\sigma_{bending} = \frac{M_{bending}r_2}{I_{x,y}}$

Transversal and torsional stress: $\tau_{transversal} = \frac{F_{transversal}}{A}$, $\tau_{torsion} = \frac{M_{torsion}r_2}{I_p}$

This leads to the following maximum tensional, compressive and shear stresses in the cross-section at the connection point.

$$\sigma_{tension} = \begin{cases} \sigma_{axial} - \sigma_{bending} & for\ \sigma_{axial} - \sigma_{bending} < 0 \\ 0 & else \end{cases}$$

$$\sigma_{compression} = \begin{cases} \sigma_{axial} + \sigma_{bending} & for\ \sigma_{axial} - \sigma_{bending} > 0 \\ 0 & else \end{cases}$$

$$\tau_{shear} = \tau_{transversal} + \tau_{torsional}$$

Note: these are the maximum reaction stresses at the connection point. In reality the stress and force in the joints can become higher due to inertia in the joints. This is not considered here, and they are only modelled as springs/dampers.

N: Maximum Results

Table 0.1: Maximum occurring motions of floater 1 for the different models subjected to various wave directions.

μ		$x\ [m]$	$y\ [m]$	$z\ [m]$	$\phi\ [rad]$	$\theta\ [rad]$	$\psi\ [rad]$
0°	FD	8.13	0	6.06	0	0.45	0
	TDL	7.93	0	6.01	0	0.43	0
	TDNL	8.04	0	6.02	0	0.45	0
15°	FD	7.83	2.09	6.04	0.1	0.41	0.09
	TDL	7.64	2.07	5.99	0.1	0.4	0.07
	TDNL	7.75	2.05	5.99	0.1	0.42	0.16
30°	FD	6.99	4.02	5.99	0.19	0.37	0.15
	TDL	6.81	3.99	5.93	0.19	0.37	0.12
	TDNL	6.94	3.95	5.93	0.19	0.38	0.19
45°	FD	5.67	5.64	5.92	0.27	0.32	0.17
	TDL	5.52	5.59	5.86	0.27	0.31	0.14
	TDNL	5.62	5.58	5.86	0.27	0.31	0.15
60°	FD	3.98	6.85	5.86	0.34	0.23	0.15
	TDL	3.88	6.79	5.81	0.33	0.22	0.12
	TDNL	3.92	6.79	5.81	0.33	0.22	0.08
75°	FD	2.05	7.6	5.82	0.38	0.12	0.08
	TDL	2	7.53	5.77	0.37	0.12	0.07
	TDNL	1.98	7.55	5.77	0.37	0.12	0.05
90°	FD	0	7.86	5.81	0.39	0.01	0
	TDL	0	7.79	5.76	0.39	0.03	0
	TDNL	0	7.79	5.76	0.39	0.03	0

Table 0.2: Maximum occurring joint reaction forces at connection point P1 for the different models subjected to various wave directions.

μ		F_x [kN]	F_y [kN]	F_z [kN]	F_ϕ [kNm]	F_θ [kNm]	F_ψ [kNm]
0°	FD	7.47	0	2.27	0	3.67	0
	TDL	3.34	0	2.25	0	2.5	0
	TDNL	4.3	0	2.22	0	2.62	0
15°	FD	6.02	1.3	4.6	0	2.39	0
	TDL	2.29	1.3	4.63	0	1.18	0
	TDNL	3.02	1.31	4.88	0	1.25	0
30°	FD	3.69	1.59	6.29	0.01	1.21	0
	TDL	1.7	1.59	6.33	0.01	0.62	0
	TDNL	2.72	1.3	6.44	0.01	0.59	0
45°	FD	2.02	1.58	6.47	0.01	0.69	0
	TDL	2.38	1.57	6.47	0.01	0.53	0
	TDNL	3.17	1.33	6.64	0.01	0.52	0
60°	FD	1.07	1.11	5.16	0	0.36	0
	TDL	2.98	1.11	5.16	0	0.7	0
	TDNL	3.17	1.3	5.29	0	0.69	0
75°	FD	0.66	0.67	2.84	0	0.2	0
	TDL	3.19	0.67	2.86	0	0.77	0
	TDNL	3.13	1.12	2.94	0	0.75	0
90°	FD	0.47	0	0	0	0.2	0
	TDL	3.13	0	0	0	0.8	0
	TDNL	3.14	0	0	0	0.77	0

Table 0.3: Maximum occurring reaction stress at joint P1 for the different models subjected to various wave directions. Axial, bending, total compressive, total tensile, transversal, torsional and total shear stress.

μ		σ_a [MPa]	σ_b [MPa]	σ_c [MPa]	σ_t [MPa]	τ_{trans} [MPa]	τ_{tor} [MPa]	τ_s [MPa]
0°	FD	0.11	1.47	1.48	1.57	0.03	0	0.03
	TDL	0.05	1	1.03	1.02	0.03	0	0.03
	TDNL	0.06	1.05	1.09	1.02	0.03	0	0.03
15°	FD	0.09	0.96	0.96	1.04	0.07	0	0.07
	TDL	0.03	0.47	0.48	0.49	0.07	0	0.07
	TDNL	0.05	0.5	0.51	0.5	0.07	0	0.08
30°	FD	0.06	0.48	0.51	0.53	0.1	0	0.1
	TDL	0.03	0.25	0.25	0.27	0.1	0	0.1
	TDNL	0.04	0.24	0.23	0.25	0.1	0	0.1
45°	FD	0.03	0.27	0.26	0.3	0.1	0	0.1
	TDL	0.04	0.21	0.21	0.25	0.1	0	0.1
	TDNL	0.05	0.21	0.23	0.25	0.1	0	0.1
60°	FD	0.02	0.14	0.15	0.13	0.08	0	0.08
	TDL	0.04	0.28	0.26	0.32	0.08	0	0.08
	TDNL	0.05	0.28	0.28	0.32	0.08	0	0.08
75°	FD	0.01	0.08	0.08	0.09	0.04	0	0.04
	TDL	0.05	0.31	0.29	0.36	0.04	0	0.04
	TDNL	0.05	0.3	0.3	0.35	0.05	0	0.05
90°	FD	0.01	0.08	0.08	0.08	0	0	0
	TDL	0.05	0.32	0.33	0.36	0	0	0
	TDNL	0.05	0.31	0.34	0.35	0	0	0